



*energies*

# Advanced Technologies in Hydropower Flow Systems

---

Edited by

Adam Adamkowski and Anton Bergant

Printed Edition of the Special Issue Published in *Energies*

# **Advanced Technologies in Hydropower Flow Systems**

# Advanced Technologies in Hydropower Flow Systems

Editors

**Adam Adamkowski**

**Anton Bergant**

MDPI • Basel • Beijing • Wuhan • Barcelona • Belgrade • Manchester • Tokyo • Cluj • Tianjin



*Editors*

Adam Adamkowski  
Polish Academy of Sciences  
Poland

Anton Bergant  
Litostroj Power d.o.o. &  
University of Ljubljana  
Slovenia

*Editorial Office*

MDPI  
St. Alban-Anlage 66  
4052 Basel, Switzerland

This is a reprint of articles from the Special Issue published online in the open access journal *Energies* (ISSN 1996-1073) (available at: [https://www.mdpi.com/journal/energies/special\\_issues/advanced\\_technologies\\_hydropower\\_flow\\_systems](https://www.mdpi.com/journal/energies/special_issues/advanced_technologies_hydropower_flow_systems)).

For citation purposes, cite each article independently as indicated on the article page online and as indicated below:

LastName, A.A.; LastName, B.B.; LastName, C.C. Article Title. *Journal Name* **Year**, *Volume Number*, Page Range.

**ISBN 978-3-0365-4693-3 (Hbk)**

**ISBN 978-3-0365-4694-0 (PDF)**

© 2022 by the authors. Articles in this book are Open Access and distributed under the Creative Commons Attribution (CC BY) license, which allows users to download, copy and build upon published articles, as long as the author and publisher are properly credited, which ensures maximum dissemination and a wider impact of our publications.

The book as a whole is distributed by MDPI under the terms and conditions of the Creative Commons license CC BY-NC-ND.

# Contents

<b>Kai Zhang, Xinkuo Jiang, Shiyang Li, Bin Huang, Shuai Yang, Peng Wu and Dazhuan Wu</b> Transient CFD Simulation on Dynamic Characteristics of Annular Seal under Large Eccentricities and Disturbances Reprinted from: <i>Energies</i> <b>2020</b> , <i>13</i> , 4056, doi:10.3390/en13164056 . . . . .	<b>1</b>
<b>Adam Adamkowski, Waldemar Janicki and Mariusz Lewandowski</b> Measurements of Discharge through a Pump-Turbine in Both Flow Directions Using Volumetric Gauging and Pressure-Time Methods Reprinted from: <i>Energies</i> <b>2020</b> , <i>13</i> , 4706, doi:10.3390/en13184706 . . . . .	<b>23</b>
<b>Zhiyan Yang, Zirui Liu, Yongguang Cheng, Xiaoxi Zhang, Ke Liu and Linsheng Xia</b> Differences of Flow Patterns and Pressure Pulsations in Four Prototype Pump-Turbines during Runaway Transient Processes Reprinted from: <i>Energies</i> <b>2020</b> , <i>13</i> , 5269, doi:10.3390/en13205269 . . . . .	<b>51</b>
<b>Hamid Arionfard and Sina Mohammadi</b> Numerical Investigation of the Geometrical Effect on Flow-Induced Vibration Performance of Pivoted Bodies Reprinted from: <i>Energies</i> <b>2021</b> , <i>14</i> , 1128, doi:10.3390/en14041128 . . . . .	<b>71</b>
<b>Martin Polák</b> Innovation of Pump as Turbine According to Calculation Model for Francis Turbine Design Reprinted from: <i>Energies</i> <b>2021</b> , <i>14</i> , 2698, doi:10.3390/en14092698 . . . . .	<b>87</b>
<b>Erick O. Castañeda Magadán, Gustavo Urquiza Beltrán, Laura L. Castro Gómez and Juan C. García Castrejón</b> Application of CFD to the Design of Manifolds Employed in the Thermodynamic Method to Obtain Efficiency in a Hydraulic Turbine Reprinted from: <i>Energies</i> <b>2021</b> , <i>14</i> , 8359, doi:10.3390/en14248359 . . . . .	<b>101</b>
<b>Madhusudhan Pandey, Dietmar Winkler, Kaspar Vereide, Roshan Sharma and Bernt Lie</b> Mechanistic Model of an Air Cushion Surge Tank for Hydro Power Plants Reprinted from: <i>Energies</i> <b>2022</b> , <i>15</i> , 2824, doi:10.3390/en15082824 . . . . .	<b>121</b>

Article

# Transient CFD Simulation on Dynamic Characteristics of Annular Seal under Large Eccentricities and Disturbances

Kai Zhang <sup>1</sup>, Xinkuo Jiang <sup>2</sup>, Shiyang Li <sup>1</sup>, Bin Huang <sup>3</sup>, Shuai Yang <sup>1</sup>, Peng Wu <sup>1,\*</sup> and Dazhuan Wu <sup>1,4</sup>

<sup>1</sup> College of Energy Engineering, Zhejiang University, Hangzhou 310027, China; zhangkai612@zju.edu.cn (K.Z.); lishiyang@zju.edu.cn (S.L.); shuaiyangzju@zju.edu.cn (S.Y.); wudazhuan@zju.edu.cn (D.W.)

<sup>2</sup> China Tianchen Engineering Corporation, Tianjin 300400, China; jiangxinkuo@zju.edu.cn

<sup>3</sup> Ocean College, Zhejiang University, Hangzhou 310027, China; binhuang@zju.edu.cn

<sup>4</sup> State Key Laboratory of Fluid Power Transmission and Control, Hangzhou 310027, China

\* Correspondence: roc@zju.edu.cn; Tel.: +86-1373-543-5349

Received: 17 June 2020; Accepted: 3 August 2020; Published: 5 August 2020

**Abstract:** Annular seals of turbomachinery usually suffer from various degrees of eccentricities and disturbances due to the rotor–stator misalignment and radial loads, while the discussion of annular seal under both large static eccentricities and dynamic disturbances is relatively limited. In this paper, the applicability of linear assumption and reliability of nonlinear dynamic model for eccentric annular seals under large eccentricities and disturbances is discussed based on the investigation of seals with various rotor motions through computational fluid dynamics (CFD). After the validation of transient CFD methods by comparison with experimental and bulk theory results, the dynamic behaviors of annular seal are analyzed by adopting both direct transient simulations and the nonlinear Muszynska model. The results show that the nonlinear dynamic model based on rotor circular whirls around seal center can predict the fluid excitations of different types of rotor motions well under small static eccentricities, while it is limited severely with large static eccentricities, which indicates that the dynamic characteristics of annular seal under large eccentricities are related with the rotor’s motion ways. The paper provides a reference for studies of rotor–seal system with complex rotor motions considering radial loads or running across the resonance region.

**Keywords:** annular seal; CFD; dynamic coefficients; fluid forces; nonlinear dynamic model; static eccentricity

## 1. Introduction

Hydraulic machinery such as pumps and turbines is widely applied in various energy fields, playing a significant role in energy development, utilization and transformation. The vibration caused by the fluid forces generated in gap seals of hydraulic machinery tend to have important effects on the efficiency and vibration of rotor system [1]. Due to the rise of safety and efficiency concerns, dynamic characteristics of various annular seals have been studied by researchers [2–5]. Almost all of these studies are based on the assumption of small perturbation, hence linear dynamic characteristics of annular seals can be investigated. Generally, the annular seal is not the supporting element in design. Under the condition of static equilibrium, the rotor is normally concentric with the annular seal. Due to the axial-symmetry of seal geometry, as shown in Figure 1, the force coefficients of concentric seals show symmetric or skew symmetric features, as shown in Equation (1), where  $F_x$ ,  $F_y$  are the X and Y components of fluid forces respectively;  $K$  and  $k$  denote direct and cross stiffness coefficients,

respectively; similarly, direct and cross damping coefficients are expressed as  $C$  and  $c$ , respectively; and  $M$  is direct mass coefficient. These five coefficients can be numerically computed by using the bulk flow model [6], CFD simulations by introducing moving reference frame [7,8] or transient method [9] and measured by perturbing the rotor or the stator [10].

$$-\begin{Bmatrix} F_x \\ F_y \end{Bmatrix} = \begin{bmatrix} K & k \\ -k & K \end{bmatrix} \begin{Bmatrix} x \\ y \end{Bmatrix} + \begin{bmatrix} C & c \\ -c & C \end{bmatrix} \begin{Bmatrix} \dot{x} \\ \dot{y} \end{Bmatrix} + \begin{bmatrix} M & 0 \\ 0 & M \end{bmatrix} \begin{Bmatrix} \ddot{x} \\ \ddot{y} \end{Bmatrix} \quad (1)$$

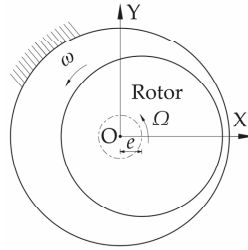


Figure 1. The circular whirl around seal center.

However, under actual condition, the static eccentricity of the rotor may exist in annular seal due to the misalignment during assembly process or the effects of various side loads (e.g., impeller weight). The dynamic characteristics of eccentric annular seals, as shown in Figure 2, were also investigated based on the bulk flow model by Nelson and Nguyen [11]. The fluid force increments ( $\Delta F_x$  and  $\Delta F_y$ ) induced by the small perturbation around static eccentricity position are similarly expressed in linearized rotordynamic form, as shown in Equation (2) [12].

$$-\begin{Bmatrix} \Delta F_x \\ \Delta F_y \end{Bmatrix} = \begin{bmatrix} k_{xx} & k_{xy} \\ k_{yx} & k_{yy} \end{bmatrix} \begin{Bmatrix} \Delta x \\ \Delta y \end{Bmatrix} + \begin{bmatrix} c_{xx} & c_{xy} \\ c_{yx} & c_{yy} \end{bmatrix} \begin{Bmatrix} \Delta \dot{x} \\ \Delta \dot{y} \end{Bmatrix} + \begin{bmatrix} m_{xx} & 0 \\ 0 & m_{yy} \end{bmatrix} \begin{Bmatrix} \Delta \ddot{x} \\ \Delta \ddot{y} \end{Bmatrix}, \quad (2)$$

where  $\Delta x$  and  $\Delta y$  define the rotor motion relative to the equilibrium position. Unlike concentric seals, the force coefficients of eccentric seals are no longer symmetric or skew symmetric due to rotor misalignment. This brings difficulties to the numerical solutions of force coefficients. Arghir and Frene [13] compared the bulk flow model of concentric seals and eccentric seals, the results showing that the terms of circumferential partial derivatives emerge in all bulk flow equations due to the static eccentricity of flow field. This can result in the coupling effect between circumferential momentum equation and continuity equation and make the solutions of both bulk flow equations and their perturbation equations very complex. As to the CFD method, the seal flow field disturbed by rotor circular whirl is not axisymmetric, as shown in Figure 2, and the steady-state simplified treatment by introducing moving reference frame is no longer applicable [8]. This means that transient simulations are necessary for evaluating force coefficients of eccentric seals.

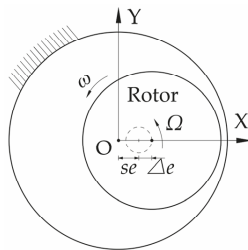


Figure 2. The circular whirl around equilibrium position.

To overcome numerical difficulties in eccentric seal research, Venkataraman and Palazzolo [14] determined the circumferential derivatives through a cubic spline interpolation method and simplified the bulk flow equations of eccentric seals. Athavale and Hendricks [15] presented a small perturbation CFD method for calculation of rotordynamic coefficients of concentric and eccentric seals, and the SCISEAL code along with a modified SIMPLEX algorithm was adopted. Wu et al. [16] developed a new transient CFD method, which is based on rotor's variable-speed whirl; the results show that this new method can keep good accuracy of traditional transient method and save much computational time and cost in the meantime.

The research for fluid force presented above has mainly focused on linear fluid force analysis, and it was performed under the strict restriction and assumption that the whirl amplitude is relatively very small compared to the seal clearance (within  $0.1 C_r$ ;  $C_r$  denotes the seal clearance). While large amplitude vibration often occurs during the passage of the critical speed of actual turbomachinery, the linear bulk flow analysis may not be applicable for the accurate fluid force characteristics in such situations with large amplitude. To describe the fluid forces of annular seal induced by large disturbances, the nonlinear dynamic model should be established. San Andres and Jeung [17] presented an orbit analysis method based on extended Reynolds equation to investigate force coefficients valid over a wide frequency range of a squeeze film damper bearing with large amplitude and static eccentricity. Ikemoto et al. [6] investigated the nonlinear fluid forces for the concentric seal with large whirl amplitude up to about a half of the clearance by using extended perturbation analysis of the bulk flow theory. Currently, the Muszynska's model proposed by Bently and Muszynska [18] is commonly used by researchers as a nonlinear dynamic model. Li and Chen [19] adopted the Muszynska's seal force model with the empirical parameters to investigate the 1:2 subharmonic resonance of labyrinth seal-rotor system. These empirical parameters obtained by employing the CFD analysis are used in the subsequent nonlinear analysis, regardless of whether the whirl amplitude is around the concentric position or not. He and Jing [20] indicated that Muszynska's model will not describe the dynamic characteristics of the rotor-seal system well when the rotor-seal system has larger eccentricity ratio. However, the present paper is devoted to develop nonlinear dynamic models of concentric seal with large whirl amplitude or eccentric seal with large static eccentricity and rather small whirl amplitude. The applicability of linear assumption and reliability of nonlinear model for seals under large static eccentricities and disturbance amplitude is rarely discussed in the literature. Thus, an investigation on the applicability of nonlinear Muszynska's model under large eccentricities and disturbances is wished for, particularly in nonlinear rotor-seal system research considering radial loads.

In experimental studies of eccentric seals, Marquette, Childs and Andres [21] measured the force coefficients of a plain liquid annular seal under different static eccentricities, and the results show that the force coefficients were more sensitive to the changes of static eccentricity than theoretically predicted. Childs, Arthur and Mehta [22] measured the net reaction forces of gas annular seals as the eccentricity ratios increased; negative stiffness created by unanticipated eccentricities may lead to over prediction of critical speeds, which illustrates the importance of concentric assembly of annular seals.

In this paper, three-dimensional (3D) transient CFD simulations based on dynamic mesh method are performed to evaluate the static and dynamic characteristics of eccentric annular seals. The obtained force coefficients and leakage rates are compared with Marquette's experiment [21] for validating the reliability of the transient CFD method. The effects of rotor disturbance amplitude on the dynamic characteristics of eccentric annular seals are analyzed to investigate the linear ranges of seal dynamic characteristics. In addition, transient CFD simulations and a nonlinear dynamic model are adopted to study the fluid excitations of annular seals induced by different rotor large motions. The nonlinear dynamic model is based on the famous Muszynska's model [18,23,24] and is obtained by fitting the "nominal" force coefficients of concentric annular seal under different whirl amplitude, as shown in Figure 2. With nonlinear model and transient CFD simulations, fluid excitations under various large disturbances are computed. Based on these fluid excitations, seal dynamic characteristics under large

eccentricities and disturbances are investigated in detail, which provides a solid basis for the research of seal–rotor system analysis by using Muszynska’ model as nonlinear seal force.

## 2. Numerical Methods

### 2.1. Geometry Model and Grid

The plain annular seal adopted to perform the studies in this paper is applied in high speed hydrostatic journal bearings, which is tested in the apparatus and facility in Marquette’s experiment. The work medium is water at 20 °C. The geometric and operating parameters of the seal are listed in Table 1. As shown in Figure 3, the structured grids are generated in the concentric annular fluid domain by the CFD Preprocessor Gambit, which is geometry and mesh generation commercial software for computational fluid dynamics (CFD) analysis.

**Table 1.** Parameters of plain annular seal.

Main Parameters	Symbols	Values	Units
seal length	$L$	34.93	mm
seal diameter	$D$	76.29	mm
seal clearance	$C_r$	0.11	mm
rotating speed	$\omega$		rpm
pressure difference	$\Delta P$	5.52	MPa
length-diameter ratio	$L/D$	0.46	

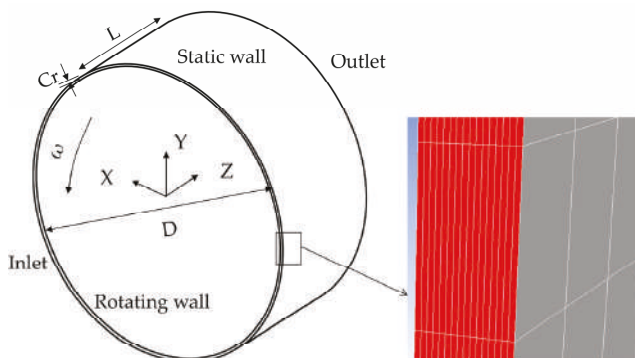


**Figure 3.** Numerical model of concentric annular seal.

The grid independence is checked by comparing the several grids with different radial grid densities. Under 80% eccentricity ratio, the radial and tangential components of fluid force are evaluated according to different grid models, as shown in Figure 4. The curves of “Fr refined” and “Ft refined” represent the radial and tangential fluid force of refined grid model, which has 36 radial layers with more than 10 layers near the both walls to keep  $y^+$  less than 5. The grid model of 16 radial layers is adopted considering the accuracy and computational time. With respect to the tangential and axial density, it can be seen in Table 2 that the results of fluid force show good convergence at Grid 3 ( $16 \times 318 \times 1448$ , i.e., there are 16 layers of grids generated along seal clearance in radial direction, 318 layers in axial direction and 1448 layers in circumferential direction) as the grid density changes to 1.25 or 1.5 times. This indicates that the present grid resolution ( $16 \times 318 \times 1448$ , 7,358,770 grid cells) is suitable for this research considering about the accuracy and efficiency of simulations.

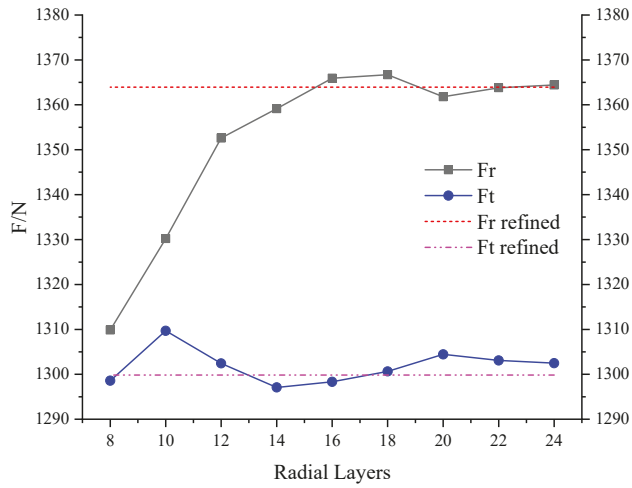


Figure 4. Radial grid density study.

Table 2. Tangential and axial grid density study.

Name	Grid Density	Fr/N	Relative Error <sup>1</sup>	Ft/N	Relative Error <sup>1</sup>
Grid 1	16 × 204 × 1448	1331.43	2.53%	1278.62	1.52%
Grid 2	16 × 254 × 1448	1358.79	0.52%	1289.26	0.70%
Grid 3	16 × 318 × 1448	1365.92	-	1298.33	-
Grid 4	16 × 397 × 1448	1367.51	−0.12%	1299.54	−0.09%
Grid 5	16 × 477 × 1448	1367.86	−0.14%	1300.15	−0.14%
Grid 6	16 × 318 × 926	1344.51	1.57%	1276.36	1.69%
Grid 7	16 × 318 × 1158	1360.28	0.41%	1290.79	0.58%
Grid 8	16 × 318 × 1810	1366.09	−0.01%	1298.65	−0.02%
Grid 9	16 × 318 × 2170	1365.82	0.01%	1298.93	−0.05%

<sup>1</sup> Note: by comparing with Grid 3 (16 × 318 × 1448, radial × axial × tangential layers).

2.2. 3D Transient Solutions

Under various rotor disturbances, the static and dynamic characteristics of plain annular seal are investigated by simulating the transient flow in seal clearance. In this paper, the commercial CFD solver, ANSYS Fluent, is chosen to solve the 3D Reynolds-averaged Navier–Stokes equations. To achieve transient simulations, dynamic mesh problem should be firstly settled. As shown in Figure 2, the motion of rotor (i.e., rotating wall) can change the shape of fluid domain, and grids will change accordingly. However, due to high aspect ratio of grid cells in the clearance, the three types of dynamic methods in Fluent—spring-based smoothing, local remeshing and dynamic layering methods—tend to cause bad orthogonality or negative volume of grids.

To ensure good grid quality, the dynamic mesh model based on interpolation method [9,25] is adopted in this paper, which can effectively control the movement of the grids. First, nodes on rotating wall (i.e., rotor surface) are controlled to move according to the motion equation of the rotor and nodes on static wall keep stationary. Then, the ratio of nodes in the clearance is deduced according to the geometric relations of position of nodes in the clearance and movement of rotor. After that, the motions of grid nodes in the domain are determined by using the interpolation method based on the distances of the nodes from rotor and stator walls. Finally, the positions and velocities of grid nodes in the domain are obtained after the movement of rotor.

Figure 5 shows the grid nodes moving in the clearance of annular seal. As illustrated in the figure,  $pf^0 (x^0_f, y^0_f)$  and  $pb^0 (x^0_b, y^0_b)$  represent the nodes of rotor surface and stator surface, respectively,

when the rotor is at the concentric position.  $pi^0(x_i^0, y_i^0)$  is an arbitrary node in the clearance domain of annular seal along the line between  $pf^0$  and  $pb^0$ .  $\theta$  denotes the initial angular coordinate of node  $pf^0$ . The superscript denotes the moving step of nodes and the subscript denotes the position of nodes.  $d^1(x_d^1, y_d^1)$  represents the motion vector of moving rotor in Cartesian coordinates.  $di^1$  denotes the vector from  $pi^0$  to  $pi^1(x_i^1, y_i^1)$ . Then, the new coordinates  $(x_f^1, y_f^1)$  of  $pf^0$  (current node  $pf^1$ ) are defined as Equation (3).

$$x_f^1 = x_f^0 + x_d^1, y_f^1 = y_f^0 + y_d^1, \tag{3}$$

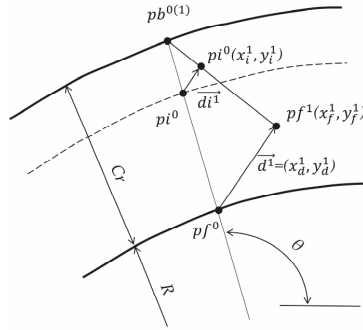


Figure 5. Schematic diagram of moving grid node.

The node of stator surface is assumed to stay still, the movement distance between rotor and stator is determined by the interpolation algorithm. Then, the new position coordinates  $(x_f^1, y_f^1)$  of  $pi^1$  could be expressed as Equation (4).

$$x_i^1 = x_i^0 + ra \times x_d^1, y_i^1 = y_i^0 + ra \times y_d^1, \tag{4}$$

where  $ra$  denotes the ratio of the distance between the nodes in the clearance domain and the static outer wall to the clearance. When the rotor is in concentric and eccentric position, the initial angular coordinate  $\theta$  of  $pf^0$  and the ratio of  $ra$  can be expressed by known parameters  $R$  and  $C_r$  and the coordinates of  $pf^0$ ,  $pi^0$  and  $pb^0$  according to collinear geometric relations of  $pf^1$ ,  $pi^1$  and  $pb^1$ . Then, the new position of  $pi^1$  in the clearance after the movement of rotor can be obtained by substituting  $ra$  to Equation (3).

The displacement of each node is restricted and calculated by mathematical procedures, which strictly ensures the movement coordination of adjacent grid nodes. The whole dynamic mesh process is implemented by adopting a subroutine linked with the CFD solver. This algorithm has been tested and the results show that, when the rotor whirled from the concentric position (with exaggerated seal clearance  $C_r$ ), as shown in Figure 6a, to the eccentric position, as shown in Figure 6b, the grid distortion rate will increase but there is no negative volumes and highly distorted elements. The maximum grid aspect ratio will not exceed 200 even with eccentricity ratios ( $e/C_r$ ,  $e$  denotes the rotor eccentricity) of 80%, which indicates that this dynamic mesh algorithm is suitable for the transient simulation with large eccentricity.

Due to rotor eccentricity, one side of the grids is compressed and the maximum aspect ratio of the grids increases on basis of the initial grid model in Figure 6a. Considering the extreme thin grid layers, numerical computations are performed under double precision to ensure the stability and reliability of the result. The boundary conditions of 5.52 MPa total pressure and 0 Pa static pressure are, respectively, adopted at inlet and outlet. Both walls are set as no-slip walls and the rotating wall possesses a rotation speed which equals to  $r/\text{min}$ . The wall  $y+$  of flow field under various disturbances is generally located in the range of 20–40 and the Realizable  $k-\epsilon$  model with enhanced wall function is suitable to handle the

situation [9,16]. The first-order implicit scheme is used for the discretization of time term. The chosen time step is equal to the wall rotation for 1 degree so that the Courant number in most regions can be confined within 5 for stability. More than 360 steps are performed to ensure the stability of transient simulation according to different rotor motions. The second-order up-wind scheme with numerical under-relaxation is adopted to the convection term in the equations. The central-differencing scheme is employed to discretize the diffusion. The velocity–pressure coupling is solved by using the well-known SIMPLE strategy. Each simulation case for one revolution costs about 50 h on the platform of CPU is Intel® Xeon® Gold 6240 @ 2.60GHz with an average 16-parallel-processes solver.

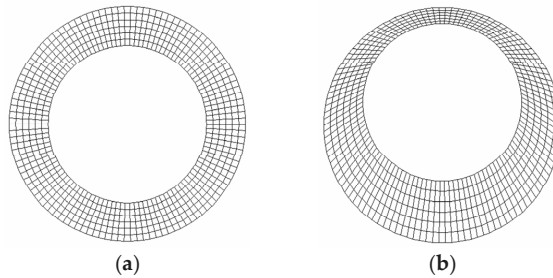


Figure 6. Diagram of cross section of the meshed rotor: (a) initial grids; and (b) moved grids.

### 2.3. Computing Static and Dynamic Characteristics of Eccentric Annular Seals

Transient CFD simulations are used to compute the static and dynamic characteristics of eccentric seals. The six cases with different static eccentricity ratios ( $se/C_r$ , where  $se$  denotes the static eccentricity of rotor) are investigated, respectively, 0%, 10%, 20%, 30%, 40% and 50%. The eccentric direction in +X direction is shown in Figure 2. The leakage rates of eccentric annular seals can be obtained by simulating the steady-state flow fields without rotor disturbances. The dynamic characteristics of eccentric seals can be analyzed by considering small rotor perturbations. The adopted perturbation is the circular whirl with a small whirl amplitude  $\Delta e$  (termed as dynamic eccentricity), as shown in Figure 2. The whirling speed  $\Omega$  is constant. Given the suitability of small perturbation assumption, dynamic eccentricity ratio ( $\Delta e/C_r$ ) should be very small (1% in the study). The small whirls are described by Equation (5). The fluid force increments ( $\Delta F_x$  and  $\Delta F_y$ ) induced by perturbations are expressed by Equation (6).

$$\begin{cases} \Delta x = x - se = \Delta e \cos(\Omega t) \\ \Delta y = y - 0 = \Delta e \sin(\Omega t) \end{cases} \quad (5)$$

$$\begin{cases} \Delta F_x = F_x - F_{x0} \\ \Delta F_y = F_y - F_{y0} \end{cases} \quad (6)$$

where  $F_{x0}$  and  $F_{y0}$  represent fluid forces at equilibrium position. Substituting Equations (5) and (6) into Equation (2),  $F_x$  and  $F_y$  can be expressed as the harmonic functions of time, as shown in Equation (7):

$$\begin{cases} F_x = F_{x0} + A_1 \Delta e \cos(\Omega t) + B_1 \Delta e \sin(\Omega t) \\ F_y = F_{y0} + B_2 \Delta e \cos(\Omega t) + A_2 \Delta e \sin(\Omega t) \end{cases} \quad (7)$$

where

$$\begin{cases} A_1 = -k_{xx} - c_{xy}\Omega + m_{xx}\Omega^2 \\ B_1 = -k_{xy} + c_{xx}\Omega + m_{xy}\Omega^2 \\ A_2 = -k_{yy} + c_{yx}\Omega + m_{yy}\Omega^2 \\ B_2 = -k_{yx} - c_{yy}\Omega + m_{yx}\Omega^2 \end{cases} \quad (8)$$

By simulating the transient flow field with rotor perturbation, the time histories of  $F_x$  and  $F_y$  can be recorded by integrating the fluid pressure at each time step. Then, they are used to evaluate  $F_{x0}$ ,

$F_{y0}$  and the four constant coefficients ( $A_1, B_1, A_2$  and  $B_2$ ) in Equation (7) by curve fittings.  $A_1, B_1, A_2$  and  $B_2$  are composed of a known whirling speed  $\Omega$  and three unknown force coefficients, as shown in Equation (8). To obtain all the unknown force coefficients,  $A_1, B_1, A_2$  and  $B_2$  under at least three (generally five is desired considering the fitting error) whirling speeds should be determined. Hence, at least three transient CFD simulations should be performed.

#### 2.4. Fitting Nonlinear Dynamic Model

Force coefficients of annular seals can only be used to describe fluid forces induced by rotor small perturbations. The Muszynska’s model is adopted to describe the fluid forces of annular seal induced by large disturbances. It is derived based on a serial of experiments and adopts nonlinear dynamic parameters similar with force coefficients to associate fluid forces with rotor motion, as shown in Equation (9):

$$\begin{Bmatrix} F_x \\ F_y \end{Bmatrix} = - \begin{bmatrix} S - m_f \tau_1^2 \omega^2 & \tau_1 \omega D \\ -\tau_1 \omega D & S - m_f \tau_1^2 \omega^2 \end{bmatrix} \begin{Bmatrix} x \\ y \end{Bmatrix} - \begin{bmatrix} D & 2\tau_1 \omega m_f \\ -2\tau_1 \omega m_f & D \end{bmatrix} \begin{Bmatrix} \dot{x} \\ \dot{y} \end{Bmatrix} - \begin{bmatrix} m_f & 0 \\ 0 & m_f \end{bmatrix} \begin{Bmatrix} \ddot{x} \\ \ddot{y} \end{Bmatrix}, \quad (9)$$

where  $S = S_0(1 - \varepsilon^2)^{-n}$ ,  $\tau_1 = \tau_0(1 - \varepsilon)^b$ ,  $D = D_0(1 - \varepsilon^2)^{-n}$ , for  $\varepsilon = \sqrt{x^2 + y^2}/C_r$

$n, \tau_0$  and  $b$  are empirical factors for certain seal structure;  $S_0, D_0$  and  $m_f$  can be computed using Black–Childs formulas [26]. When the seal is under steady working condition (constant  $\omega$  and  $\Delta P$ ), the  $S_0, D_0, m_f$  and empirical factors in Muszynska’s model become constant values. Namely, nonlinear dynamic parameters in matrices are only related with eccentricity ratio  $\varepsilon$ . Thus, Equation (9) can be expressed in a simplified form, as shown in Equation (10):

$$\begin{Bmatrix} F_x \\ F_y \end{Bmatrix} = - \begin{bmatrix} K(\varepsilon) & k(\varepsilon) \\ -k(\varepsilon) & K(\varepsilon) \end{bmatrix} \begin{Bmatrix} x \\ y \end{Bmatrix} - \begin{bmatrix} C(\varepsilon) & c(\varepsilon) \\ -c(\varepsilon) & C(\varepsilon) \end{bmatrix} \begin{Bmatrix} \dot{x} \\ \dot{y} \end{Bmatrix} - \begin{bmatrix} M(\varepsilon) & 0 \\ 0 & M(\varepsilon) \end{bmatrix} \begin{Bmatrix} \ddot{x} \\ \ddot{y} \end{Bmatrix}, \quad (10)$$

The Muszynska’s model under constant working condition is very similar to the linear dynamic model of concentric annular seal in Equation (1). The only difference is that dynamic parameters in Equation (10) are nonlinear functions of  $\varepsilon$  and can be used to describe fluid forces induced by rotor large disturbances. The expressions of nonlinear dynamic parameters can be determined based on the formulas in Equation (9), but proper empirical factors need to be chosen. In addition, the nonlinear expressions can be fitted based on the “nominal” force coefficients of concentric seal under different eccentricities (as shown in Figure 2). These “nominal” force coefficients can be computed by using CFD methods [8,27]. Rotor perturbation is the circular whirl around seal center. Usually, whirl amplitude (i.e., rotor eccentricity) is controlled within  $0.1C_r$  for satisfying the linear assumption. To obtain “nominal” force coefficients under different eccentricities, the limitation is broken here, and the adopted whirl amplitudes are located in the range of  $0.01C_r$ – $0.8C_r$  (i.e.,  $\varepsilon$  in 1%–80%).

Transient CFD simulations are conducted to solve the flow field disturbed by constant-speed circular whirals, and fluid-induced forces can be obtained. Based on these fluid forces, the “nominal” force coefficients of concentric annular seal can be evaluated [8] and used to generate the nonlinear dynamic model. With respect to the Muszynska’s model, the new nonlinear model does not need any empirical factors. Theoretically, it can describe fluid forces (seal forces) induced by various rotor motions within eccentricity ratio 80%. Its reliability and suitability are discussed in Section 3.

### 3. Results and Discussions

#### 3.1. Dynamic Characteristics of Different Static Eccentric Seals and Comparisons

The leakage rates and force coefficients of annular seal under different static eccentricity positions and same whirl amplitude ratio ( $\Delta e/C_r = 1\%$ ) are computed using the numerical scheme based on transient CFD simulations (see Section 2.3). They are, respectively, shown in Figures 7–12 along with the results from San Andres’ bulk flow method and Marquette’s experiments.

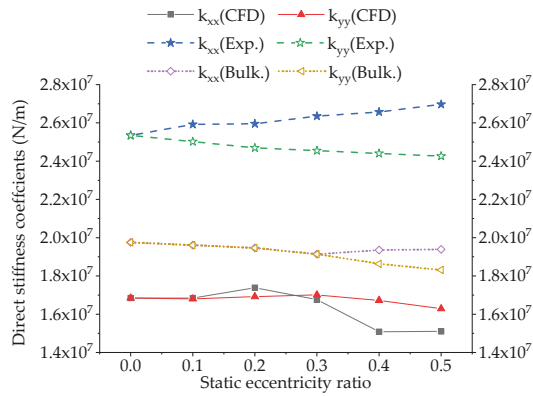


Figure 7. Direct Stiffness coefficients of eccentric annular seals.

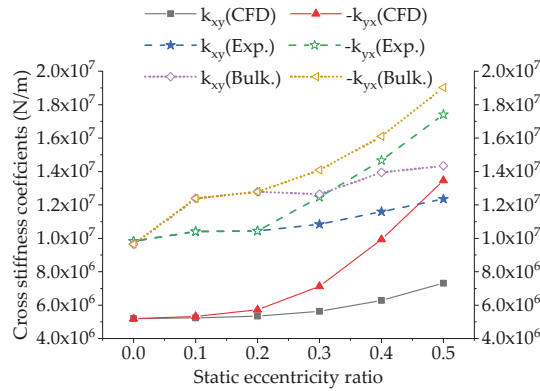


Figure 8. Cross Stiffness coefficients of eccentric annular seals.

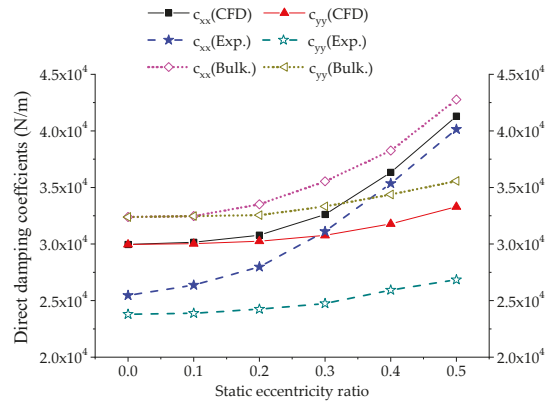


Figure 9. Direct damping coefficients of eccentric annular seals.

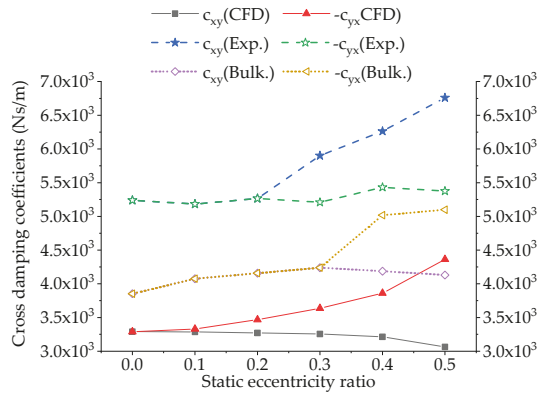


Figure 10. Cross damping coefficients of eccentric annular seals.

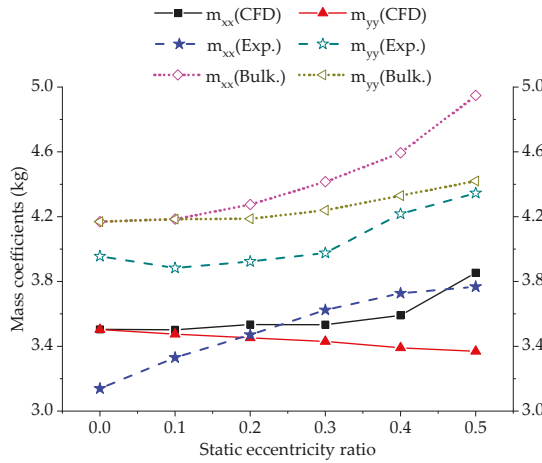


Figure 11. Mass coefficients of eccentric annular seals.

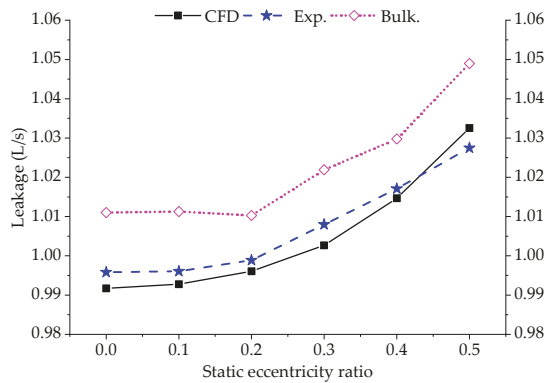


Figure 12. Leakage rates of eccentric annular seals.

In Figures 7 and 8, the measured values of direct and cross stiffness coefficients are larger than numerical values from transient CFD simulations. The test apparatus of Marquette’s experiment does not include any device to control or measure the inlet swirl, and the non-uniformity of incoming flow is not considered during the testing procedure, which may lead to variations of stiffness coefficients with eccentric directions according to Wu’s research [28]. The boundary condition of seal model illustrated in Marquette’s research is only pressure condition for inlet and outlet. There is no geometry information or measurement of inlet, which is also mentioned by the authors as a drawback. The reason of the lower accuracy is that it is much difficult to ensure the boundary condition of CFD analysis, especially for the inlet, consistent with the Marquette’s experiment. Tae Woong Ha’s study [27] shows the similar difference between the stiffness results of CFD analysis and the experimental results. Despite the differences of values in Figure 7, it shows a high level of consistency between results of transient simulations and measured values as static eccentricity ratio increases.

In Figures 9 and 10, direct damping coefficients from transient simulations and bulk flow method are both a little higher than measured values, and CFD results are closer to experimental values. Cross damping coefficients from the three approaches are all close in size. As shown in Figure 11, although numerical results of mass coefficients do not coincide with measured values in variation trend, they are close in size.

Figure 12 shows the variations of seal leakage rate with the eccentricity. As rotor eccentricity increases, seal leakage rate just slightly rises. In Figure 12, leakage rates computed by transient simulations are very close to measured values, which further indicate the reliability of CFD method. This also shows that leakage rates of annular seals mainly depend on sealed differential pressures and are not sensitive to flow status at seal inlet, unlike force coefficients [28].

On the whole, rotor eccentricities change the static and dynamic characteristics of annular seals to some extent; the behaviors of annular seals should be specially considered when the rotor is far away from seal center. By comparing with experimental data, transient CFD simulations are effective in computing the static and dynamic behaviors of eccentric seals.

### 3.2. Effects of Disturbance Amplitude on Force Coefficients of Eccentric Annular Seal

The force coefficients of eccentric seals in Figures 7–12 are computed using a very small dynamic eccentricity (eccentricity ratio 1%). To study the effects of disturbance amplitude, two more dynamic eccentricity ratios, 5% and 10%, are separately adopted to evaluate force coefficients of eccentric seals. The results are presented in Figures 13–17 for comparisons.

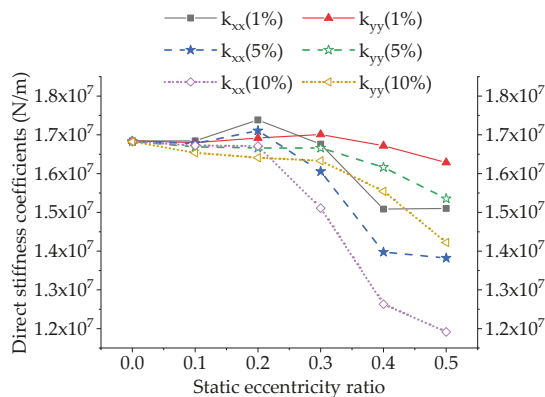


Figure 13. Direct stiffness coefficients under different dynamic eccentricities.

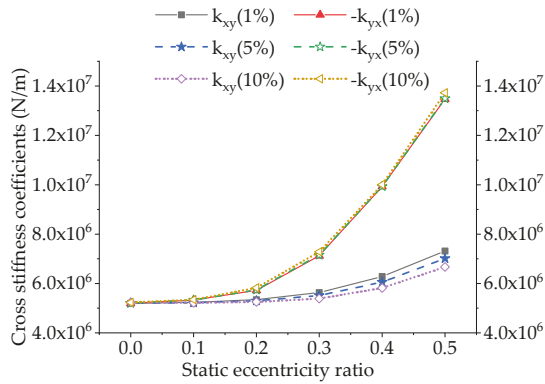


Figure 14. Cross stiffness coefficients under different dynamic eccentricities.

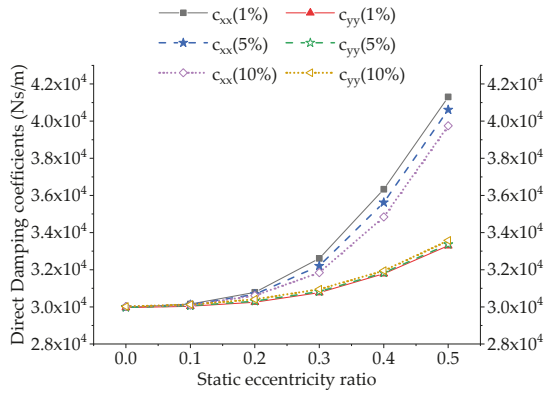


Figure 15. Direct damping coefficients under different dynamic eccentricities.

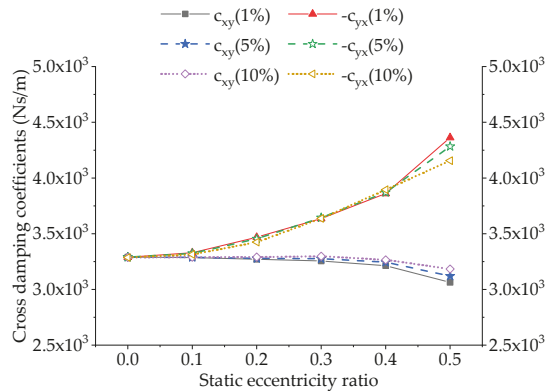


Figure 16. Cross damping coefficients under different dynamic eccentricities.

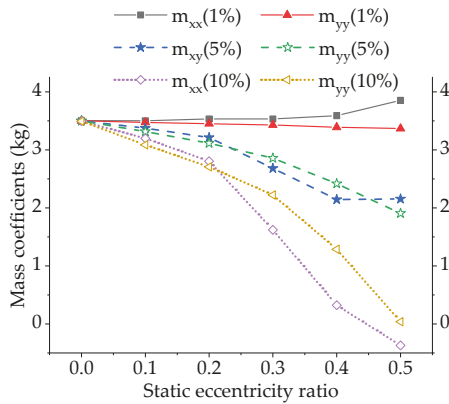


Figure 17. Mass coefficients under different dynamic eccentricities.

As shown in Figures 13–17, force coefficients based on three dynamic eccentricities are not the same. Their differences grow gradually as rotor static eccentricity increases, especially the coefficients  $k_{xx}$ ,  $k_{yy}$ ,  $k_{xy}$ ,  $c_{xx}$ ,  $m_{xx}$  and  $m_{yy}$ . For the concentric seal with static eccentricity zero, its force coefficients are generally unchanged with varying dynamic eccentricities. Namely, the dynamic characteristics of concentric annular seal are still linear when dynamic eccentricity ratio reaches 10%, which has been widely recognized by researchers [7,8,29]. However, as to the eccentric annular seal, its force coefficients tend to be sensitive to dynamic eccentricities (i.e., disturbance amplitude). As rotor static eccentricity increases, the sensitivity to rotor disturbances strengthens gradually and the linear range of seal dynamic characteristics narrows. With respect to the concentric seal, the annular seal under large eccentricity is more likely to show nonlinear characteristics.

### 3.3. Nonlinear Dynamic Model

As discussed above, force coefficients of eccentric seals can only be used to describe fluid forces induced by very small perturbations due to their strong sensitivity to disturbance amplitude. To express seal forces under large eccentricities or large disturbances, the nonlinear dynamic model is determined based on the thought in Section 2.3. The “nominal” force coefficients of concentric seal are computed based on different whirl amplitudes. They are presented in Figure 18 along with polynomial fitting curves. Piecewise fittings are used for direct stiffness  $K$  and cross damping  $c$ . As shown in Figure 18, the fitting effects of five force coefficients are satisfactory. The nonlinear expressions of these coefficients are listed as follows:

$$K(\varepsilon)(\times 10^6) = \begin{cases} 2.71\varepsilon^2 - 0.703\varepsilon + 16.9, & \varepsilon \leq 0.1, R^2 = 1 \\ 1.70\varepsilon^3 - 8.67\varepsilon^2 + 4.21\varepsilon + 16.5, & 0.1 < \varepsilon \leq 0.8, R^2 = 0.9911 \end{cases} \quad (11)$$

$$c(\varepsilon)(\times 10^3) = \begin{cases} -16.2\varepsilon^4 + 10.8\varepsilon^3 - 2.20\varepsilon^2 + 0.0767\varepsilon + 3.29, & \varepsilon \leq 0.4, R^2 = 0.9995 \\ -2.28 + 6.15\varepsilon^2 - 5.43\varepsilon + 4.58, & 0.4 < \varepsilon \leq 0.8, R^2 = 0.9997 \end{cases} \quad (12)$$

$$M(\varepsilon) = -5.28\varepsilon^4 + 6.63\varepsilon^3 - 3.58\varepsilon^2 + 0.36\varepsilon + 3.50, \quad \varepsilon \leq 0.8, R^2 = 0.9905 \quad (13)$$

$$k(\varepsilon)(\times 10^7) = 14.5\varepsilon^5 - 24.2\varepsilon^4 + 15.5\varepsilon^3 - 3.22\varepsilon^2 + 0.250\varepsilon + 0.517, \quad \varepsilon \leq 0.8 \\ R^2 = 0.9999 \quad (14)$$

$$C(\varepsilon)(\times 10^4) = 10.7\varepsilon^4 - 11.6\varepsilon^3 + 5.57\varepsilon^2 - 0.682\varepsilon + 3.01, \quad \varepsilon \leq 0.8, R^2 = 0.9994 \quad (15)$$

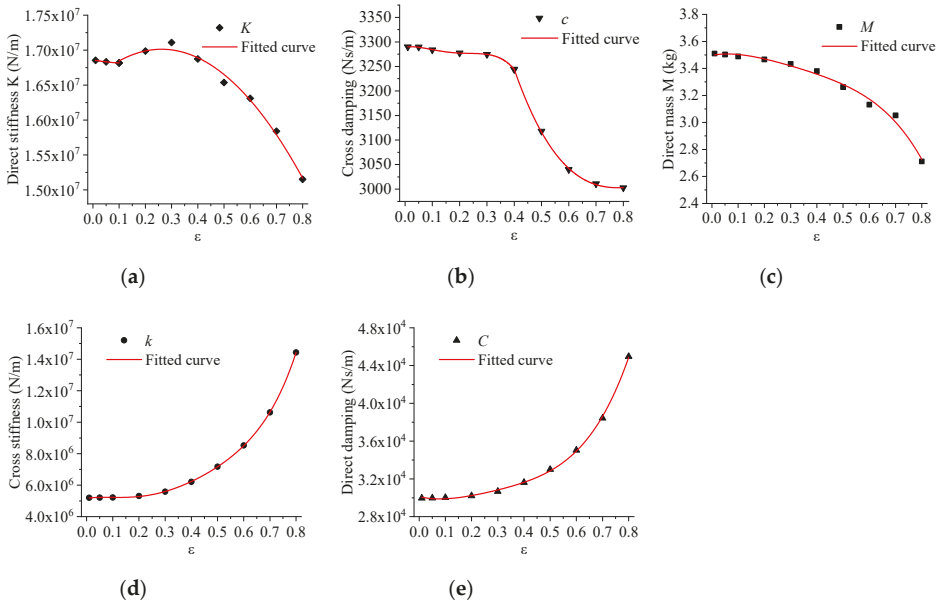


**Figure 18.** “Nominal” force coefficients of concentric annular seal: (a) direct stiffness; (b) cross damping; (c) direct mass; (d) cross stiffness; and (e) direct damping.

Substituting these nonlinear expressions into Equation (10), the nonlinear dynamic model is obtained. It will be used to evaluate fluid forces induced by rotor large disturbances along with transient CFD simulations.

**4. Fluid Excitations under Large Disturbances**

The fluid forces of annular seal under rotor large motions are computed by nonlinear dynamic model as well as transient CFD simulations. The suitability of nonlinear dynamic model for various rotor disturbances is investigated through comparisons with direct transient simulations. Several typical rotor motions are chosen for the investigation.

*4.1. Constant-Speed Circular Whirl Around Seal Center*

The rotor performs circular whirl around seal center with speed 10,200 r/min (Figure 1) and the whirl magnitude is 55%  $C_r$ . The motion equation is shown as below. Substituting Equations (11)–(16) into Equation (10), the induced fluid forces ( $F_x$  and  $F_y$ ) are obtained by the nonlinear dynamic model. They are shown in Figure 19 along with the results from transient CFD simulations.

$$\begin{cases} x = e\cos(\Omega t) \\ y = e\sin(\Omega t) \end{cases} \quad (16)$$

Because the prescribed initial solution is not absolutely accurate, the transient CFD computation needs passing a period of time to eliminate its effects. Fluid forces computed at initial some time steps are not true and can be ignored. In Figure 19, fluid force curves from nonlinear dynamic model and transient CFD simulations are in good agreement. Maximum differences are only 16.5 N for both  $F_x$  and  $F_y$ , and they are mainly caused by fitting and computing errors. This indicates that the present nonlinear dynamic model is adequate to describe seal fluid excitations induced by circular whirls around seal center.

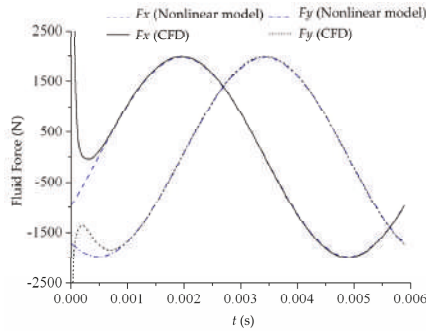


Figure 19. Fluid forces induced by the circular whirl around seal center.

4.2. Constant-Speed Circular Whirl Around Static Position

The rotor is assumed to perform circular whirl around static eccentricity position, as shown in Figure 2. The dynamic eccentricity ratio is 10%. Two whirl centers correspond to static eccentricity ratio 20% and 50%, respectively. The whirling speed is same with the rotating speed, 10,200 r/min. Rotor movements ( $x, y$ ) can be expressed by Equation (3). Substituting Equations (3) and (11)–(15) into Equation (10), fluid-induced forces ( $F_x$  and  $F_y$ ) are obtained by nonlinear dynamic model. They are compared with the forces from transient CFD simulations, as shown in Figures 20 and 21

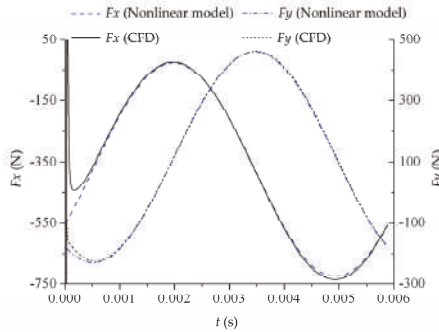


Figure 20. Fluid forces induced by the circular whirl around seal center ( $se/C_r$  20%).

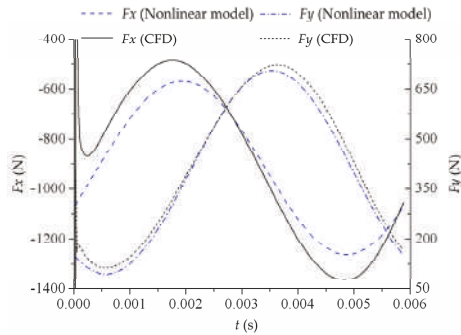


Figure 21. Fluid forces induced by the circular whirl around seal center ( $se/C_r$  50%).

As shown in Figure 20, for the circular whirl around the static position with eccentricity ratio 20%, fluid forces from nonlinear dynamic model and transient CFD simulations agree well.

Maximum differences are 9.42 N for  $F_x$  and 4.65 N for  $F_y$ . However, when the static eccentricity ratio increases to 50%, fluid force curves obtained by these two approaches are no longer consistent, as shown in Figure 21. The maximum differences are 111 N for  $F_x$  and 36.7 N for  $F_y$ . This indicates that the nonlinear dynamic model has low reliability for rotor disturbances under large eccentricity. However, the circular whirl around concentric position is an exception (see Figure 19). The nonlinear dynamic model can deal with it well. The two rotor motions corresponding to Figures 19 and 21 are both under large eccentricities. The only difference is their motion ways. The rotor motion corresponding to Figure 19 is the whirl around seal center, and “nominal” force coefficients used for generating the nonlinear dynamic model are based on this motion way. Therefore, it is understandable that the nonlinear model applies well. From this point of view, the reason that nonlinear dynamic model does not suitable for circular whirls around large eccentricity position (as shown in Figure 21) can be assumed to be that the force coefficients (or dynamic characteristics) of annular seal under large eccentricity are related to rotor motion ways.

### 4.3. 1D Harmonic Shaking Motions

To validate the assumption proposed above, the circular whirl around the static position with eccentricity ratio 50% is divided into two separate 1D shaking motions, as shown in Figure 22. One is the shaking motion in X direction; the other is in Y direction. The Y direction is also the tangential direction of the concentric whirl. Namely, the Y-directional shaking is somewhat similar to the circular whirl around seal center. The expressions of two shaking motions are, respectively, presented in Equations (17) and (18). The amplitude  $A$  is 10%  $C_r$  and the harmonic frequency  $\Omega$  corresponds to the speed 10,200 r/min.

$$\begin{cases} x = se + A\cos(\Omega t) \\ y = 0 \end{cases} \tag{17}$$

$$\begin{cases} x = se \\ y = A\sin(\Omega t) \end{cases} \tag{18}$$

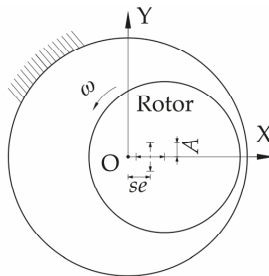


Figure 22. Two harmonic shaking motions.

According to motion equations of two harmonic shakings, fluid-induced forces can be obtained by nonlinear dynamic model and transient CFD simulations. They are shown in Figures 23 and 24. The comparison with transient CFD simulations shows that the reliability of nonlinear dynamic model is low in predicting fluid forces induced by X-directional shaking. Maximum differences of two approaches are 119 N for  $F_x$  and 30.8 N for  $F_y$ . However, as to the Y-directional shaking, the reliability of the nonlinear model is obviously improved, as shown in Figure 24. This can be attributed to the slight likeness of Y-directional shaking with the circular whirl around seal center. In Figure 20, maximum differences of two approaches are 18.5 N for  $F_x$  and 17.7 N for  $F_y$ , and they are much smaller than those in Figure 23. Namely, the nonlinear dynamic model is more applicable to rotor disturbances similar to the circular whirl around concentric position. The assumption proposed in Section 4.2 is confirmed and can explain the low reliability of nonlinear dynamic model. Under large eccentricity, the dynamic

characteristics of seals are varied with the motion ways of the rotor, and the nonlinear dynamic model based on a specific motion way is incompetent in dealing with all kinds of rotor disturbances.

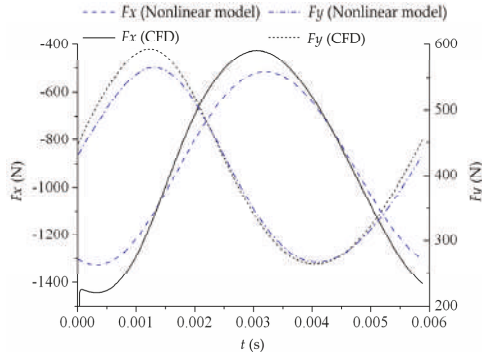


Figure 23. Fluid forces induced by X-directional shaking.

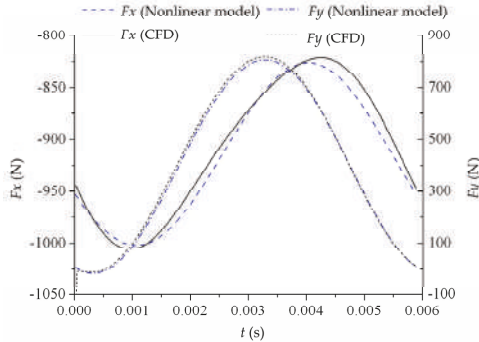


Figure 24. Fluid forces induced by Y-directional shaking.

#### 4.4. Quasi-Circular (Spiral) Whirl

In this section, the rotor is assumed to perform the circular whirl around seal center with growing whirl radius, i.e., the spiral whirl, in order to validate the suitability of nonlinear dynamic model for quasi-circular whirls no matter eccentricity magnitudes. The whirling speed is  $r/\text{min}$  and the rotor eccentricity ratio rises linearly to 60% within six whirl periods. The whirl equation is presented in Equation (17) and the whirl orbit is shown in Figure 25.

$$\begin{cases} x = f \cdot t \cos(\Omega t) \\ y = f \cdot t \sin(\Omega t) \end{cases} \quad (19)$$

where  $T$  is the whirl period and  $f = 60\% C_r / (6 T)$ , indicating the eccentricity speed of the rotor.

In actual applications, the spiral whirl in Figure 25 represents the destabilizing process of the rotor. Fluid forces induced by the destabilizing whirl are obtained, respectively, by nonlinear dynamic model and transient CFD simulations. They are shown in Figure 26. The rise of rotor eccentricity with time leads to the increasing fluid force (i.e., the resultant force of  $F_x$  and  $F_y$ ). The  $F_x$  and  $F_y$  from nonlinear model are in good agreement with those from transient CFD simulations. Maximum differences of two approaches are 42.7 N (i.e., relative error 2.3%) for  $F_x$  and 35.7 N (relative error 2.3%) for  $F_y$ . Namely, nonlinear dynamic model is reliable in evaluating fluid forces induced by the quasi-circular whirl around seal center without special limitations on eccentricity magnitudes.

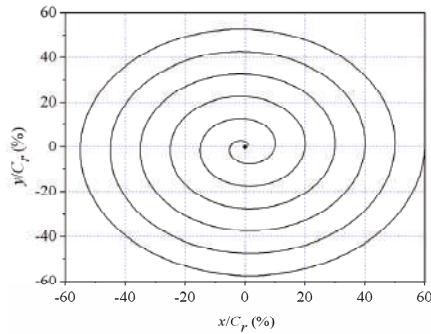


Figure 25. Spiral whirl orbit of the rotor.

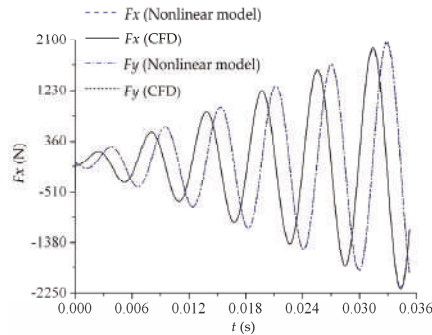


Figure 26. Fluid forces induced by the spiral whirl around seal center.

### 5. Conclusions

In the paper, dynamic characteristics of the annular plain liquid seal under various large rotor disturbance motions are studied using the transient CFD method based on dynamic mesh technique and nonlinear Muszynska’ model.

Force coefficients and leakage rates of annular seal under different static eccentricities are evaluated. The reliability of transient CFD simulation is validated by comparing the force coefficients and leakage rates with those from the Marquette’s experiment and bulk flow method. With increasing static eccentricity, these force coefficients show clearly asymmetric behavior and obvious changes. The force coefficients from transient CFD simulations show a high consistency with experimental values despite the different values of stiffness. The error sources are mainly form the influence of upstream and inlet boundary condition due to the drawback of the experimental apparatus for absent inlet control. Leakage rates computed by the CFD method fit better to measured values than those from the bulk flow method, which indicates that leakage rates are insensitive to static eccentricity.

As to the concentric annular seal, its dynamic characteristics are usually supposed to be linear (namely, constant force coefficients) when the rotor disturbance is within 10%  $C_r$ . However, this conclusion is not suitable for the eccentric annular seal, especially the seal under large static eccentricity. As rotor static eccentricity increases, the force characteristics of annular seal become more sensitive to whirl amplitude, in other words, the linear range of dynamic characteristics narrows gradually. With respect to the concentric seal, the annular seal with large eccentricity is easier to show nonlinear characteristics.

According to the Muszynska’s model, a nonlinear dynamic model is presented in the paper for describing nonlinear seal forces induced by rotor large disturbances. The suitability of the nonlinear model for all kinds of rotor disturbances is studied through four forms of rotor motions.

The nonlinear dynamic model is suitable for various rotor disturbances when the rotor is under small static eccentricity (e.g., eccentricity ratio under 20%). However, when rotor static eccentricity is large (e.g., eccentricity ratio 50%), the nonlinear dynamic model based on circular whirls around eccentric center becomes incompetent and unsatisfactory. It shows high reliability only for circular or quasi-circular whirls around concentric center. This means that dynamic characteristics of annular seal under large disturbance are related to rotor motion ways. For the annular seals under large dynamic eccentricity (whirl amplitude) and rather small static eccentricity (e.g., static eccentricity ratio under 20% in this case), the nonlinear Muszynska's model performs well when dealing with large rotor disturbances. The range of capability of this nonlinear model depends on the typical parameters of annular seals. It can also explain why Muszynska's model is out of action when rotor–seal system has a large eccentricity ratio in He's research.

On the whole, dynamic characteristics of annular seals under large disturbance are very complex. They are very sensitive to various rotor motion ways including whirl amplitude and static eccentricity. For the seal with large disturbances motion of a small static eccentricity, the nonlinear Muszynska's model performs reliably, which provides a solid basis for the seal–rotor system analysis using nonlinear seal force model. The capability and limitation of nonlinear dynamic model under large disturbances needs further investigation.

**Author Contributions:** Conceptualization, K.Z. and D.W.; methodology, K.Z., X.J. and P.W.; validation, D.W. and P.W.; formal analysis, K.Z. and X.J.; investigation, K.Z., S.L. and P.W.; resources, D.W.; data curation, K.Z., X.J. and S.Y.; writing—original draft preparation, K.Z. and X.J.; writing—review and editing, S.L. and S.Y.; visualization, K.Z.; supervision, P.W. and D.W.; project administration, B.H. and D.W.; and funding acquisition, B.H. All authors have read and agreed to the published version of the manuscript.

**Funding:** This research was funded by National Natural Science Foundation of China, grant numbers 51706198 and 51839010.

**Conflicts of Interest:** The authors declare no conflict of interest.

## Nomenclature

$C$	Direct and cross damping coefficients of concentric annular seal (N·s/m)
$c_{xx}, c_{yy}, c_{xy}, c_{yx}$	Damping coefficients of eccentric annular seal (N·s/m)
$C_r$	Seal clearance (mm)
$e$	Rotor eccentricity or whirl radius (mm)
$f$	Eccentricity speed of the rotor
$F_x, F_y$	Fluid forces in X and Y directions (N)
$F_{x0}, F_{y0}$	Fluid forces at equilibrium position (N)
$\Delta F_x, \Delta F_y$	The increments of fluid forces relative to $F_{x0}$ and $F_{y0}$ (N)
$K, k$	Direct and cross stiffness coefficients of concentric seal (N/m)
$k_{xx}, k_{yy}, k_{xy}, k_{yx}$	Stiffness coefficients of eccentric annular seal (N/m)
$M$	Direct mass coefficient of concentric annular seal (kg)
$m_{xx}, m_{yy}$	Direct mass coefficients of eccentric annular seal (kg)
$ra$	Ratio of the distance between the nodes in the clearance domain and the outer static wall to the clearance
$se$	Rotor static eccentricity (mm)
$se/C_r$	Static eccentricity ratio
$t$	Time (s)
$x, y$	The displacements of rotor center (mm)
$\Delta x, \Delta y$	Rotor displacements relative to equilibrium position (mm)
$\Delta e$	Rotor dynamic eccentricity (mm)
$\varepsilon$	Eccentricity ratio ( $e/C_r$ )
$\omega$	Rotating speed of the rotor (rpm)
$\Omega$	Whirling speed of the rotor (rpm)

## References

1. Du, Q.; Zhang, D. Numerical investigation on flow characteristics and aerodynamic performance of a 1.5-stage SCO<sub>2</sub> axial-inflow turbine with labyrinth seals. *Appl. Sci.* **2020**, *10*, 373. [\[CrossRef\]](#)
2. Wang, X.; Liu, M.; Kao-Walter, S.; Hu, X. Numerical Evaluation of Rotordynamic Coefficients for Compliant Foil Gas Seal. *Appl. Sci.* **2020**, *10*, 3828. [\[CrossRef\]](#)
3. Xia, P.; Chen, H.; Liu, Z.; Ma, W.; Yang, B. Analysis of Whirling Motion for the dynamic System of Floating Ring Seal and Rotor. *Proc. Inst. Mech. Eng. Part J J. Eng. Tribol.* **2019**, *233*, 1–15. [\[CrossRef\]](#)
4. Awad, H.; Parrondo, J.; González, V. Vibrations in Leaking Spherical Valves with Annular Seal. *Proceedings* **2018**, *2*, 1444. [\[CrossRef\]](#)
5. Zhai, L.; Wu, G.; Wei, X.; Qin, D.; Wang, L. Theoretical and Experimental Analysis for Leakage Rate and Dynamic Characteristics of Herringbone-Grooved Liquid Seals. *Proc. Inst. Mech. Eng. Part J J. Eng. Tribol.* **2015**, *229*, 849–860. [\[CrossRef\]](#)
6. Ikemoto, A.; Inoue, T.; Sakamoto, K.; Uchiumi, M. Nonlinear Analysis of Rotordynamic Fluid Forces in the Annular Plain Seal by Using Extended Perturbation Analysis of the Bulk-Flow Theory (Influence of Whirling Amplitude in the Case with Concentric Circular Whirl). *J. Tribol.* **2018**, *140*, 1–15. [\[CrossRef\]](#)
7. Gao, R.; Kirk, G. CFD Study on Stepped and Drum Balance Labyrinth Seal. *Tribol. Trans.* **2013**, *56*, 663–671. [\[CrossRef\]](#)
8. Untaroiu, A.; Hayrapetian, V.; Untaroiu, C.D.; Wood, H.G.; Schiavello, B.; McGuire, J. On the Dynamic Properties of Pump Liquid Seals. *J. Fluids Eng.* **2013**, *135*, 051104. [\[CrossRef\]](#)
9. Li, F.; Cui, B.; Zhai, L. Research on Rotordynamic Characteristics of Pump Annular Seals Based on a New Transient CFD Method. *Processes* **2020**, *8*, 227. [\[CrossRef\]](#)
10. Childs, D.W.; Arthur, S.P. Static Destabilizing Behavior for Gas Annular Seals at High Eccentricity Ratios. In Proceedings of the ASME Turbo Expo 2013: Turbine Technical Conference and Exposition, San Antonio, TX, USA, 3–7 June 2013; Volume 7A, pp. 1–7.
11. Nelson, C.C.; Nguyen, D.T. Analysis of Eccentric Annular Incompressible Seals: Part 1—A New Solution Using Fast Fourier Transforms for Determining Hydrodynamic Force. *J. Tribol.* **1988**, *110*, 354. [\[CrossRef\]](#)
12. Andres, L.A.S. Analysis of Variable Fluid Properties, Turbulent Annular Seals. *J. Tribol.* **1991**, *113*, 694–702. [\[CrossRef\]](#)
13. Arghir, M.; Frene, J. A Bulk-Flow Analysis of Static and Dynamic Characteristics of Eccentric Circumferentially-Grooved Liquid Annular Seals. *J. Tribol.* **2004**, *126*, 316–325. [\[CrossRef\]](#)
14. Venkataraman, B.; Palazzolo, A.B. Thermohydrodynamic Analysis of Eccentric Annular Seals Using Cubic Spline Interpolations. *Tribol. Trans.* **1997**, *40*, 183–194. [\[CrossRef\]](#)
15. Athavale, M.M.; Hendricks, R.C. A Small Perturbation CFD Method for Calculation of Seal Rotordynamic Coefficients. *Int. J. Rotating Mach.* **1996**, *2*, 167–177. [\[CrossRef\]](#)
16. Wu, D.; Jiang, X.; Li, S.; Wang, L. A New Transient CFD Method for Determining the Dynamic Coefficients of Liquid Annular Seals. *J. Mech. Sci. Technol.* **2016**, *30*, 3477–3486. [\[CrossRef\]](#)
17. Andres, L.S.; Jeung, S.H. Orbit-Model Force Coefficients for Fluid Film Bearings: A Step beyond Linearization. *J. Eng. Gas Turbines Power* **2016**, *138*, 1–11.
18. Muszynska, A.; Bently, D.E. Frequency-swept Rotating Input Perturbation Techniques and Identification of the Fluid Force Models in Rotor/Bearing/Seal Systems and Fluid Handling Machines. *J. Sound Vib.* **1990**, *143*, 103–124. [\[CrossRef\]](#)
19. Li, Z.G.; Chen, Y.S. Research on 1:2 Subharmonic Resonance and Bifurcation of Nonlinear Rotor-Seal System. *Appl. Math. Mech. (English Ed.)* **2012**, *33*, 499–510. [\[CrossRef\]](#)
20. He, H.J.; Jing, J.P. Research into the Dynamic Coefficient of the Rotor-Seal System for Teeth-on-Stator and Teeth-on-Rotor Based on an Improved Nonlinear Seal Force Model. *J. Vib. Control* **2014**, *20*, 2288–2299. [\[CrossRef\]](#)
21. Marquette, O.R.; Childs, D.W.; San Andres, L. Eccentricity Effects on the Rotordynamic Coefficients of Plain Annular Seals: Theory Versus Experiment. *J. Tribol.* **1997**, *119*, 443. [\[CrossRef\]](#)
22. Childs, D.W.; Arthur, S.; Mehta, N.J. The Impact of Hole Depth on the Rotordynamic and Leakage Characteristics of Hole-Pattern-Stator Gas Annular Seals. *J. Eng. Gas Turbines Power* **2013**, *136*, 042501. [\[CrossRef\]](#)

23. Muszynska, A. Whirl and Whip—Rotor/Bearing Stability Problems. *J. Sound Vib.* **1986**, *110*, 443–462. [[CrossRef](#)]
24. Muszynska, A. Improvements in Lightly Loaded Rotor/Bearing and Rotor/Seal Models. *J. Vib. Acoust. Stress. Reliab. Des.* **1988**, *110*, 129–136. [[CrossRef](#)]
25. Li, Q.; Liu, S.; Pan, X.; Zheng, S. A New Method for Studying the 3D Transient Flow of Misaligned Journal Bearings in Flexible Rotor-Bearing Systems. *J. Zhejiang Univ. Sci. A* **2012**, *13*, 293–310. [[CrossRef](#)]
26. Childs, D.W. Dynamic Analysis of Turbulent Annular Seals Based On Hirs' Lubrication Equation. *J. Lubr. Technol.* **1983**, *105*, 429–436. [[CrossRef](#)]
27. Ha, T.W.; Choe, B.S. Numerical Simulation of Rotordynamic Coefficients for Eccentric Annular-Type-Plain-Pump Seal Using CFD Analysis. *J. Mech. Sci. Technol.* **2012**, *26*, 1043–1048. [[CrossRef](#)]
28. Wu, D.; Jiang, X.K.; Chu, N.; Wu, P.; Wang, L.Q. Numerical Simulation on Rotordynamic Characteristics of Annular Seal under Uniform and Non-Uniform Flows. *J. Cent. South Univ.* **2017**, *24*, 1889–1897. [[CrossRef](#)]
29. Yan, X.; Li, J.; Feng, Z. Investigations on the Rotordynamic Characteristics of a Hole-Pattern Seal Using Transient CFD and Periodic Circular Orbit Model. *J. Vib. Acoust.* **2011**, *133*, 041007. [[CrossRef](#)]



© 2020 by the authors. Licensee MDPI, Basel, Switzerland. This article is an open access article distributed under the terms and conditions of the Creative Commons Attribution (CC BY) license (<http://creativecommons.org/licenses/by/4.0/>).

Article

# Measurements of Discharge through a Pump-Turbine in Both Flow Directions Using Volumetric Gauging and Pressure-Time Methods

Adam Adamkowski, Waldemar Janicki and Mariusz Lewandowski \*

The Szwedalski Institute of Fluid-Flow Machinery, Department of Hydropower, Polish Academy of Sciences, Fiszerza 14, 80-231 Gdansk, Poland; adam.adamkowski@imp.gda.pl (A.A.); waldemar.janicki@imp.gda.pl (W.J.)

\* Correspondence: mariusz.lewandowski@imp.gda.pl

Received: 13 July 2020; Accepted: 28 August 2020; Published: 9 September 2020

**Abstract:** This article presents the original procedures for measuring the flow rate using the pressure-time and the volumetric gauging method in the case of performance tests of a reversible hydraulic machine in either turbine or pump modes of operation. Achieving the lowest possible measurement uncertainty was one of the basic conditions during implemented machine tests. It was met using appropriate measuring procedures and high-class measuring equipment. Estimation of the uncertainty for both methods was made on the basis of an analysis consistent with current requirements in this respect. The pressure-time method was supplemented by the computational fluid dynamics (CFD) analysis that allowed reducing the impact of the pipeline complex irregular geometry on the uncertainty of flow measurement. Appropriate modifications of the calculation procedure enabled accurate measurements of flow during the pump mode of operation of the tested machine as well. The volumetric gauging method, thanks to a special procedure used for accurate measurement of the water level in the upper reservoir of the power plant, allowed measuring the discharge through the tested reversible machine with very low uncertainty. The obtained results allowed for a detailed comparison and mutual verification of the methods used to measure the discharge of the tested reversible machine in both modes of its operation. The most possible causes of obtained results are discussed and summarized in the paper. The need for further research was pointed out to explain the differences obtained and their influence on the accuracy of discharge measurement using the pressure-time method in pump operation mode.

**Keywords:** reversible hydraulic machines; penstocks; pressure pipelines; performance tests; flow rate measurements; volumetric gauging method; pressure-time method; water-hammer

---

## 1. Introduction

Fluid flow rate measurements are one of the most complex measurements that are carried out in engineering practice. These measurements, due to the need to maintain a very narrow uncertainty band, usually require the use of sophisticated, precise measuring equipment and the use of appropriate rigorous measurement procedures [1–3].

Liquid flow rate measurements in closed conduits or open channels of small size, for instance up to 1–2 m of diameter, are usually carried out using standard measuring devices such as measuring orifice plates, nozzles, Venturi tubes, measuring weirs, electromagnetic and ultrasound flow meters, calibrated bends, and others. Such devices are usually installed in properly prepared measuring sections of conduits or channels and provide a relatively easy and fairly accurate method of measuring the flow rate.

The situation is definitely more complicated when the liquid flow rate is to be measured in large-size conduits with a diameter of several meters or more. Measurements of the flow rate in this

type of structure, usually used in hydropower, are very difficult and expensive, especially when it is necessary to ensure the lowest possible uncertainty of measurement results.

According to international standards [4–6], a few primary methods for flow rate measurement can be used in hydropower plants:

- The velocity-area method—utilizing the distribution of local liquid velocities, measured using propeller current meters (especially in cases of large conduit diameters) or Pitot tubes (for smaller diameters and flow of liquids free of sediments). The volumetric flow rate is determined by integrating the velocity distribution over the entire area of the measuring cross-section.
- The pressure-time method (often called the Gibson method [7,8])—consisting of measuring the time course of changes in the pressure difference between two cross-sections of a closed conduit while stopping the liquid stream by means of a shut-off device. The volumetric flow rate of the liquid at the initial conditions, prior to the stoppage of the flow, is determined by appropriate integration of the change in pressure difference measured during the stoppage of the flow.
- The tracer method—consisting of measurements of the passing time, or concentration, of the radioactive or non-radioactive marker (e.g., salt) between two cross-sections of a conduit. The method requires long conduits and suitable conditions for good mixing of the marker.
- The volumetric gauging method—consisting of determining the variation of the water volume stored in the headwater or tailwater reservoir on the basis of the variation of the water level in this reservoir over time.
- The acoustic method—based on vector summation of the sound wave propagation speed and the average liquid flow velocity—it uses a difference in frequencies or passing times of the emitted and received acoustic signal.

It can be concluded that the first four methods on the above list belong to the group of traditional methods, while the acoustic method is relatively new and has been recently the object of numerous research activities oriented on its improvement and validation [9,10]. This method has not yet reached proper acceptance among the specialists. Standard [4] suggests conditional use of this method, i.e., in case of mutual agreement between interested parties. Its basic advantage is that it can be used for continuous flow rate measurement and monitoring. Such a feature is impossible or extremely hard to achieve using other primary methods of measuring absolute flow rate.

The volumetric gauging method and tracer method are those which are less frequently used in hydropower engineering. The first method is characterized by a very limited application, mainly to hydropower plants with artificial reservoirs, especially in pumped-storage plants. The second one requires very long measuring segments of flow conduits and special conditions facilitating the mixing process of the injected markers (e.g., the use of turbulizers).

The velocity-area method and the pressure-time method are primary methods that are the most commonly used for measuring the flow rate in the pipelines of hydraulic turbines [3,11–13]. It is also worth noting that the velocity-area method using propeller current meters, very popular in the past, nowadays is being replaced by the pressure-time method in hydropower plants equipped with pipelines longer than 10–20 m. One of the main reasons for this is the much lower cost of preparing and performing flow measurements using the pressure-time method and the use of computer techniques in recent years, which facilitate measurements and give the possibility for getting higher accuracy of results obtained with this method.

For low and very low head power plants, particularly with short intakes of hydraulic turbines, (with no penstocks) the situation is different. Up to now, generally only the velocity-area methods, especially current meter method, are basically available in such kind of plants. Flow rate measurements with this method are still quite expensive and alternatives are being sought. One such alternative is the acoustic scintillation technique, under development [14,15].

Relative (index) methods are also used to measure the flow rate in hydropower plants. For example, the Winter–Kennedy method and the methods utilizing non-standardized pressure difference devices,

non-standardized overflows (weirs), some simple variants of the acoustic method or local velocity measurement, which can be used for determining the relative value of the flow rate, or even the physical value, provided that calibration has been done on site by comparing with the results of measurements using the primary method [16–18].

As is the case concerning every measurement technique, obtaining the appropriate measurement precision is of the utmost importance. This is absolutely necessary wherever there are low uncertainty requirements, e.g., in the case of performance tests of hydraulic machines. The measurement conditions occurring in the flow systems of these machines require experience and knowledge about the flow phenomena prevailing in these systems, and also force the search for additional, unconventional techniques to ensure sufficiently low measuring uncertainty.

The bases of the analysis presented in the paper are measurement examples of flow rate through a high-head reversible hydraulic machine. Measurements were conducted using the volumetric gauging method and the pressure-time method, recommended (as mentioned earlier) by international standards [4–6] as the primary methods for discharge measurements used for performance tests (warranty, acceptance) of hydraulic turbines, pump turbines, and storage pumps. However, there are some restrictions on applicability as in the case of the pressure-time method, but work is continuously ongoing to expand and update these standards (A. Adamkowski, one of the authors of this work is a member of the PTC 18 Committee that is currently developing a revision to the ASME Performance Test Code PTC 18-2011 “Hydraulic Turbines and Pump Turbines”).

The simultaneous application of the pressure-time method and the volumetric gauging method to measure discharge through the tested hydrounit with reversible Francis turbine opened the possibility of their peer verification, which was the main goal of the work.

As part of this task, the suitability of the pressure-time method for measuring flow rate in the pump mode of operation was tested. The use of this method in such conditions is not recommended by standards [4–6], therefore the obtained results are of particular importance for the development of this method.

The tests were performed ensuring a low level of measurement uncertainty. It required a number of procedures, some of which are innovative solutions, such as:

- Applying a special procedure for measuring of water level changes in the upper reservoir using the volumetric method.
- Taking into account the complex geometry of measuring section of the pipeline and its impact on flow phenomena using techniques based on computational fluid dynamics (CFD) and applying these results in the pressure-time method.

Moreover, in order to reliably estimate the measurement uncertainty of the applied methods, a procedure that takes into account general requirements concerning uncertainty assessment gathered in [19] has been proposed. This task is an attempt to systematize the problem of estimating measurement errors with the use of the analyzed methods.

Comparison concerning results obtained using chosen flow measurement methods, which is an example quite rarely seen in the literature concerning this subject, provides a unique source of knowledge about the features of the methods and the possibilities of their practical use.

## 2. Materials and Methods

### 2.1. The Research Object

Both discussed methods for discharge measurement—pressure-time and volumetric gauging method—were used for performance tests of a reversible hydrounit in a Polish pumped-storage power plant (PSP). The considered plant is equipped with four similar reversible hydraulic machines (pump-turbines) working under the head of approximately 440 m and generating/consuming power over 120 MW.

The artificial head water reservoir is connected to pump-turbines using two underground penstocks, branching close to the inlets of the pump-turbines, prior to the shut-off ball-valves. The pump-turbines are connected via the tailrace tunnel with the surge tank to the tail water tank. A schematic diagram of the PSPP flow system with its main dimensions is shown in Figure 1.

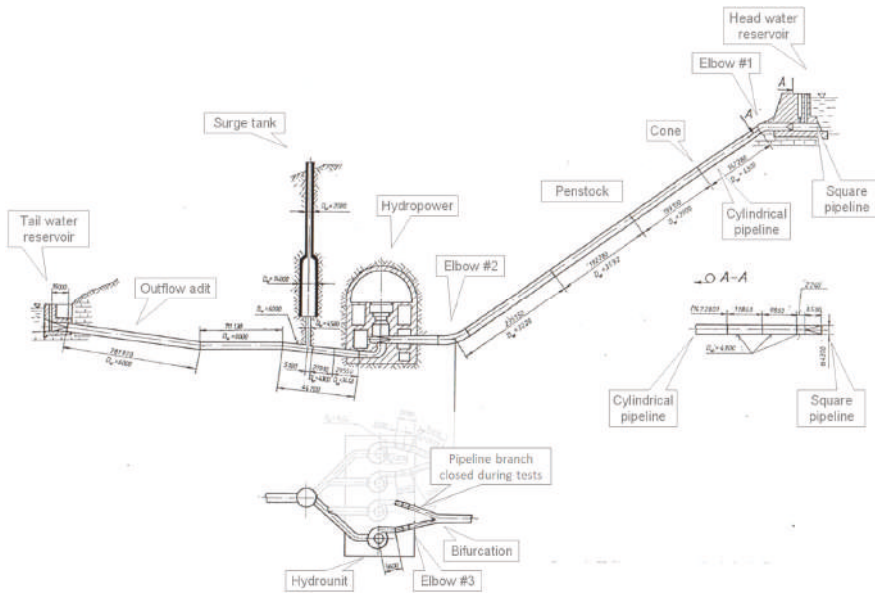


Figure 1. Flow system of the pump-turbine.

## 2.2. The Volumetric Gauging Method

Determining discharge using the volumetric gauging method consists in measuring the volume of water  $\Delta V$  flowing through the tested hydraulic machine during time  $\Delta t$ . The discharge is determined using of the following formula:

$$Q_V = \frac{\Delta V}{\Delta t} = \frac{V(z(t_f)) - V(z(t_0))}{t_f - t_0} \quad (1)$$

where  $\Delta V$  [m<sup>3</sup>] stands for measured increase or decrease in volume of water in the head water reservoir,  $\Delta t = t_f - t_0$  [s]—the time interval in which the increase/decrease in water volume occurred, and  $z$ —level of water in the head reservoir.

When using the volumetric gauging method, there are several issues that can significantly affect the accuracy of the measured flow rate [11,18]. The main task is to determine the relationship between the volume and the water level of the reservoir  $V(z)$ . This relationship should be determined on the basis of precise reservoir geometry measurements (particularly useful for artificial reservoirs) or accurate bathymetric scanning. The issue of determining the reservoir volume also involves measuring the water level in this reservoir.

In common situations, transmitters designed to control this level usually included in the power plant equipment are not suitable for use in the volumetric gauging method as they have a wide measuring range and low accuracy class. In order to achieve low uncertainty of measurements, the change in the water level in the reservoir should be determined using special methods. The schematic diagram of the proposed method is shown in Figure 2. Its most important element is measuring the increase in water level  $\Delta z$  in the power plant reservoir by means of a precise transducer measuring the

pressure difference in the reservoir and a constant pressure level set using small auxiliary tank, hung at the appropriate height. The configuration of such an installation should ensure the possibility of carrying out an approximately one-hour measurement at a fixed operating point of the tested hydrounit.

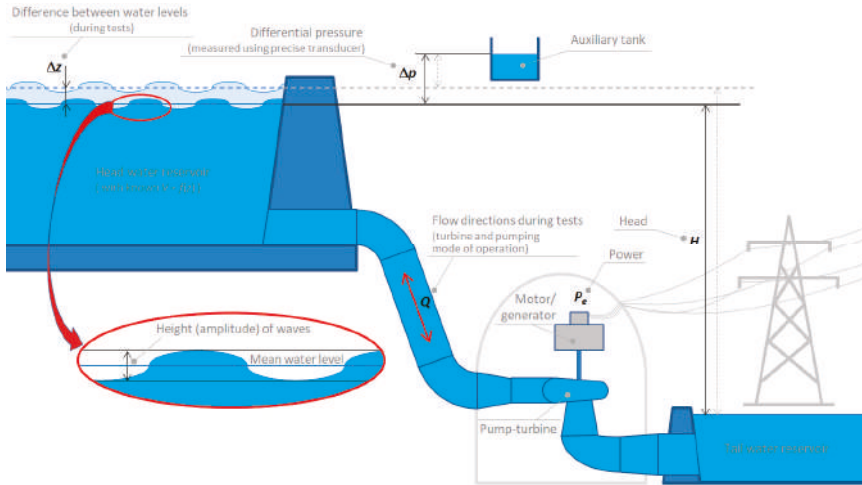


Figure 2. The water level change measurement technique used in the volumetric gauging method.

The proposed method allows for the significant reduction of the measurement uncertainty giving an additional possibility for taking into account the unfavorable phenomenon of water surface waving occurring during the tests. This phenomenon can affect the results of the measured flow rate in the most significant way. Traditional ways for measuring the water level used in the volumetric gauging method cannot ensure required accuracy of discharge measurements. Using a measuring system with appropriate characteristics and applying linear regression for the results of measuring the level of water in the reservoir leads to eliminate the effect of water waving on measurement results (Figure 3). It's worth pointing out that it is very important to base the regression line on the boundaries selected at the extreme points of the peaks or valleys of the differential pressure signal. This is a prerequisite for obtaining the correct final flow measurement results.

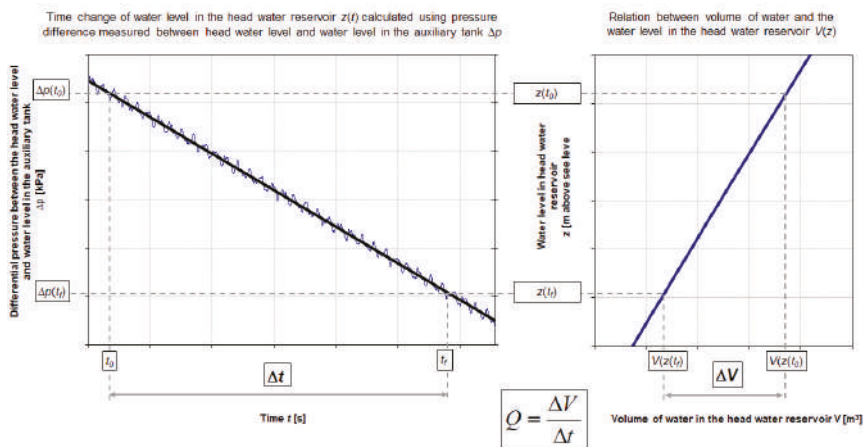


Figure 3. The volumetric gauging method—basic rules of flow rate determination.

Owing to the solutions applied, a very narrow uncertainty range was possible to achieve and the results of its estimation are presented in the next chapter of the paper. The uncertainties (standard and expended) were estimated according to the procedure described in Appendix B that was developed basing on the general recommendations presented in [19].

### 2.3. The Pressure-Time Method

#### 2.3.1. Basic Information

The pressure-time method is based on the relationship between flow rate at steady state conditions and pressure-time change occurring in the pipeline during cutting off the flow [7,8]. The value of  $Q_0$  indicating the discharge at initial liquid flow conditions is calculated using the definite integral over a time interval in which the flow varies from initial conditions to conditions after the flow is completely shut off [4,6,11]:

$$Q_0 = \frac{1}{\rho F} \int_{t_0}^{t_f} (\Delta p(t) + \Delta p_d(t) + \Delta P_r(t)) dt + Q_f \quad (2)$$

where:

$\rho$  is the density of a liquid,

$t_0$  and  $t_f$  are the initial and final time-limits of integration, respectively,

$Q_f$  is the discharge under final steady-state conditions (after complete closing of the shut-off device) due to the leakage through the closed shut-off device,

$\Delta p$  is the difference in pressures measured between the pipeline measuring cross-sections  $B-B$  and  $A-A$ , which geometrical centers are at level  $z_A$  and  $z_B$ , respectively (Figure 4):

$$\Delta p = p_B + \rho g z_B - p_A - \rho g z_A \quad (3)$$

$\Delta p_d$  is the difference in dynamic pressures between the pipeline measuring cross-sections with area of each section equal  $A_A$  and  $A_B$ :

$$\Delta p_d = \alpha_2 \frac{\rho Q^2}{2A_B^2} - \alpha_1 \frac{\rho Q^2}{2A_A^2} \quad (4)$$

where:

$\alpha_1, \alpha_2$  are the kinetic energy correction factors for  $A-A$  and  $B-B$  sections (the value of the kinetic energy correction factor for fully developed turbulent flow in the pipeline, dependent on  $Re$  number is within the limits from 1.03 to 1.11 [20,21]);

$\Delta P_r$  is the pressure loss caused by hydraulic resistance in pipeline between the measurement cross-sections—quantity calculated as proportional to the square of flow rate (accounting for its direction):

$$\Delta P_r = C_r \cdot Q|Q| \quad (5)$$

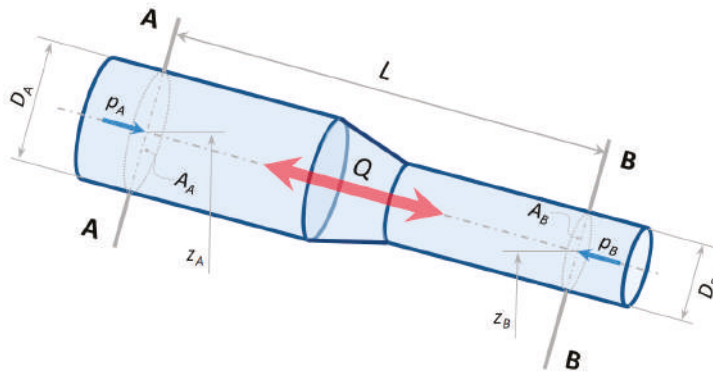


Figure 4. Scheme of the penstock measuring section with markings.

One of the most important parameters in Formula (2) is the  $F$  factor. Its value depends on the geometry of the pipeline flow system between the pressure measurement cross-sections. The following formula can be used to calculate the  $F$  factor in case of the pipeline segment with length  $L$  and  $j$  sub-segments with different sizes:

$$F = \int_0^L \frac{dx}{A(x)} = \sum_{j=1}^{j=J} \frac{\Delta x_j}{A_j}, \quad \text{with } \sum_{j=1}^{j=J} \Delta x_j = L \quad (6)$$

where  $\Delta x_j$  and  $A_j$  indicate the length and internal cross-sectional area of the  $j$ -th sub-segment, respectively. As shown in Equation (2), the pressure loss,  $\Delta P_r$ , representing hydraulic resistance and the dynamic pressure difference,  $\Delta p_d$ , should be separated from the pressure difference measured between the pipeline measurement cross-sections,  $\Delta p$ . In total, the integral expression of Equation (2) defines the pressure difference resulting from the inertia force of the mass of liquid retained in the pipeline measuring section (segment). The values of  $\Delta P_r$  and  $\Delta p_d$  can be calculated with good accuracy using their dependence on the square of the flow rate in the forms written in Equation (4) and (5).

Measurements made using the pressure-time method, as was the case concerning the volumetric gauging method, were carried out for both flow directions through a reversible machine equipped with Francis type runner. Measuring flow rate in the pump direction requires appropriate modifications of the pressure-time method to the calculation procedures described in the standards, which were postulated by the authors in earlier publications [11,22,23] and which resulted with formula in Equation (5) (introducing term  $Q|Q|$  instead of  $Q^2$ ).

A comprehensive discussion of some problems related to the computational procedures in the pressure-time method is provided in standards [4,6] as well as in monograph [11]. A description of some important problems related to the use of the pressure-time method for measuring flow rate in hydropower plants can also be found in publications [22–29]. Calculation of friction losses according to the quasi-stationary hypothesis is consistent with the conclusions presented in [30]. It was proved that the modelling of unsteady friction losses has little effect on the course of water hammer in its initial time-phase that is taken into account in the pressure-time method. Nevertheless, it should be emphasized that including the transient nature of friction losses into the calculation method, under certain circumstances, may improve predictions of the pressure-time method as described in [27–29].

Several variants of the pressure-time method are used in practice. They differ mainly in methods of measuring the pressure differences between pipeline measurement cross-sections. In the considered case, the pressure-time method was used in the variant based on measuring the pressure changes at the cross-section of the pump-turbine spiral case outlet/inlet and relating these changes to the pressure

exerted by the water column from the head water reservoir. This variant requires the determination of the geometric factor  $F$  accounting the entire penstock of the tested machine, starting from the inlet section and ending with the outlet/inlet cross-section of the spiral case.

The recommendations of the standards [4–6] allow the use of the  $F$  factor for straight-axis measuring pipelines of variable diameter (according to the Formula (6), taking into account their geometry). However, in the case of more complex changes in the geometry occurring in the measuring section of the pipeline (changes in the shape of the flow section, changes in the direction of the pipeline axis or branches), there is a need to take into account the influence of these changes on the flow conditions.

Irregular parts (components) of the penstock cause flow disturbances in the form of non-uniform water velocity distribution. This should be taken into account in order to ensure better accuracy of discharge measurement. In the considered case, except for the straight pipe sections with constant internal diameters, the penstock has three elbows (two vertical and one horizontal), a number of short conical sections connecting pipes of different diameters, and two short branches, where one branch remained closed during the tests. In addition, the square cross-section as well as transition section from square to the circular cross-section in the highest part of the penstock had to be taken into consideration. In the previously published work [24], authors presented the procedure, based on CFD, used for correction of  $F$ -factor calculated in case of penstocks with elbows. The assumption of equal kinetic energy resulting from the simulated and the uniform water flow velocity distributions in the same flow parts of the penstock was the main, except mass conservation law, theoretical basis for this procedure. In this work, using CFD, an extended procedure was developed and applied to correct the value of the  $F$ -factor for the above-mentioned irregular components of the penstock under consideration. The procedure is presented in detail in Appendix A. The selected results of CFD calculations and the  $F$ -factor correction for the studied case are presented later in this paper.

### 2.3.2. CFD Based Correction of Penstock Geometrical Factor

The *NUMECA/Hexpress* commercial software [31] was used for generating the computational grid representing the penstock geometry (Figure 5). The unstructured grids consisted of hexahedral elements.

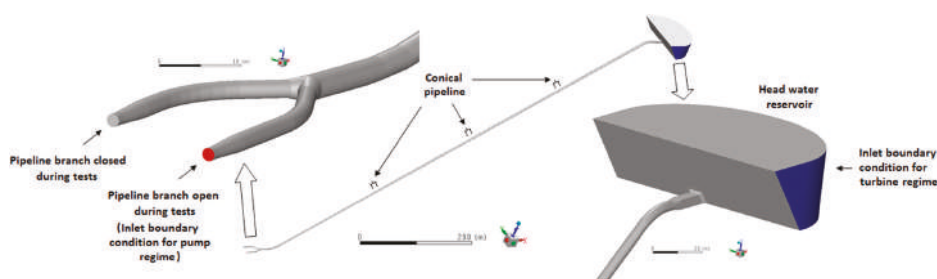


**Figure 5.** Geometry of hydraulic system (calculation domain): head water reservoir (hydraulic diameter of virtual half-cylindrical inlet 30 m) → square pipeline (4.3 × 4.3 m) → cylindrical pipe (4.3 m) → conical pipe (4.3/3.9 m) → cylindrical pipe (3.9 m) → conical pipe (3.9/3.6 m) → cylindrical pipe (3.6 m) → conical pipe (3.6/3.2 m) → cylindrical pipe (3.2 m) → pipe branch for two pump-turbines (2.276 m) → conical pipe (2.276/1.654 m) → outlet cylindrical pipe (1.654 m).

For flow calculations, *ANSYS/Fluent* commercial software was used [32]. The flow was simulated by solving the steady-state Reynolds Average Navier-Stokes (RANS) equations with the  $k-\omega$  SST turbulence model. Many studies demonstrate the great usefulness of this turbulence model in the calculation of industrial flow systems [33,34]. It's commonly known that the  $k-\omega$  SST model integrates advantages of both  $k$ -turbulence model and standard  $k-\omega$  turbulence model [35].

The second-order upwind discretization was used with the SIMPLE scheme of pressure-velocity coupling. Non-dimensional distance from wall  $Y^+$  was assumed to be in range 1 to 5 according to the used turbulence model. Initialization of calculation was done from all zones limiting the computational domain. The calculations were conducted until all of the residuals (continuity residual, velocity components, turbulent kinetic energy, and specific rate of dissipation) reached values less than 0.001. The parameters for a closure of turbulence model were hydraulic diameter and turbulence intensity. First of them was calculated using formula:  $D_h = 4A/P$  [m], in which  $A$  is the area and  $P$  is the perimeter (hydraulic diameter was 1.654 m at inlet/outlet of lower part the penstock and 30 m at inlet/outlet of upper part of the penstock). The second parameter was calculated using the formula [32]:  $I = 0.16 Re^{(-1/8)}$  in which  $Re$  is Reynolds number at inlet or outlet cross-section. At the outlet of the measuring section, constant static pressure was assumed for all calculation cases. The free surface of the reservoir was assumed as a no-slip boundary condition.

The CFD calculations were conducted for four discharge values (20, 25, 30, and 35 m<sup>3</sup>/s) in the turbine operation modes and for two discharge values (26 and 28 m<sup>3</sup>/s) in the pump operation modes. The sample of calculation results in the form of water velocity distributions in cross-sections for three chosen flow parts of the penstock were presented in Figures 6–8 for both flow directions, for analyzed discharge of 35 m<sup>3</sup>/s in turbine regime, and 28 m<sup>3</sup>/s in pump regime.

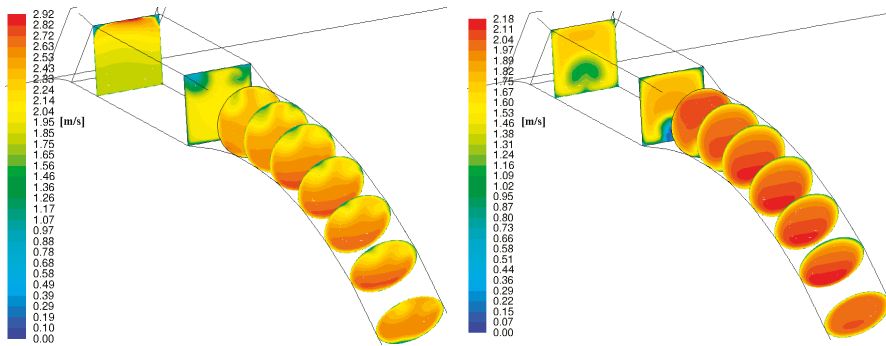


Figure 6. The water velocity contours in the penstock inlet part with first elbow for discharge of  $Q = 35 \text{ m}^3/\text{s}$  in turbine regime (left view) and for discharge of  $Q = 28 \text{ m}^3/\text{s}$  in pump regime (right view).

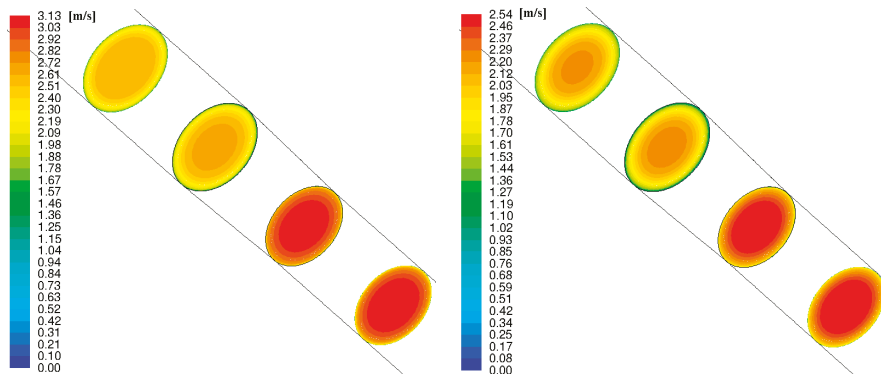
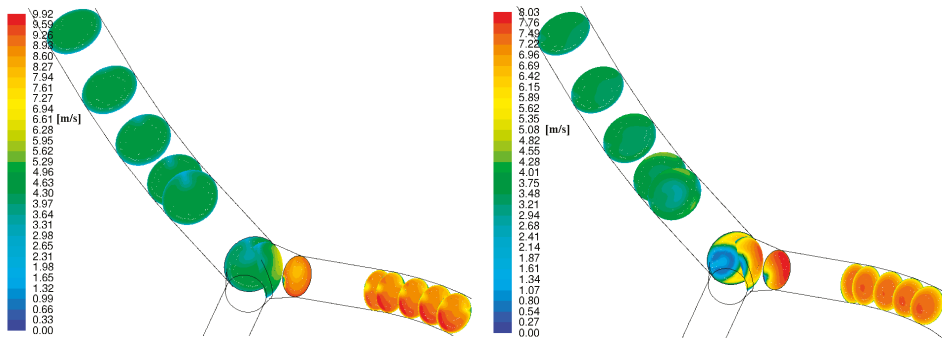


Figure 7. The water velocity contours in the penstock part containing the cone pipe for discharge of  $Q = 35 \text{ m}^3/\text{s}$  in turbine regime (left view) and for discharge of  $Q = 28 \text{ m}^3/\text{s}$  in pump regime (right view).



**Figure 8.** The water velocity contours in the penstock part containing the pipe branch for discharge of  $Q = 35 \text{ m}^3/\text{s}$  in turbine regime (left view) and for discharge of  $Q = 28 \text{ m}^3/\text{s}$  in pump regime (right view).

The CFD simulation results received for the analyzed penstock flow parts (Figures 6–8) can be characterized as follows:

- The water velocity distributions inside the area of the penstock inflow/outflow (in the cross-sections near the head water reservoir) are different for the turbine and pump operation modes.
- The largest irregular flow occurs in the penstock branch and despite the fact that it only affects the velocity distribution locally, the propagation of these irregularities in the direction of the water flow is clearly more visible than in the opposite direction. The intensity of the flow disturbance decreases rapidly with distance. On the other hand, the smallest flow irregularities in the penstock are induced by the existing short tapered pipe sections.
- The velocity distributions in the elbows also differ depending on the direction of flow, which is quite obvious—the elbows induce disturbances in the flow pattern, which propagate to the next penstock components with decreasing intensity. For example, for the turbine operation mode the flow achieving the elbow #2 is almost uniform because of the long straight section of pipe before this elbow (looking in turbine flow direction), while in pump operation mode, a similar effect takes place in elbow #1.

The CFD results taking account flow irregularities induced in the penstock were used to calculate the equivalent factor  $F_e$  according to the original procedure presented in Appendix A.

The deviation factor,  $\Delta f$ , representing a relative difference between the equivalent penstock factor,  $F_e$ , (obtained using CFD calculations) and the penstock geometrical factor,  $F$ , was included in discharge determination according to the pressure-time method. This factor is calculated as follows:

$$\Delta f = \frac{F_e - F}{F} \quad (7)$$

The values of quantity,  $\Delta f$ , determined for chosen discharge values for both flow directions are presented in Table 1. It can be stated that  $\Delta f$  is kept almost constant for both flow directions separately. However, it presents different level for both turbine and pump operational modes: the average value of  $\Delta f$  is about +0.13% and about +0.77% for turbine and pump modes of operation, respectively. These values were used as correction quantities of the geometrical factor  $F$  calculated based only on the geometry of the entire penstock.

**Table 1.** The relative differences of  $F$ -factor,  $\Delta f$ , determined for the entire penstock for the assumed discharge values in the both machine operation modes.

Machine Operation Mode	Discharge, $Q_0$	Relative Difference of $F$ -Factor, $\Delta f$
-	$m^3/s$	%
Turbine operation mode	20	0.15
	25	0.14
	30	0.13
	35	0.11
Pump operation mode	26	0.77
	28	0.77

### 2.3.3. Flow Rate Measurement, Uncertainty

The values of flow rate (discharge) were calculated based on the difference of pressures measured between the inlet/outlet cross-section of the tested pump-turbine (cross-section (B-B)) and the reservoir (cross-section (A-A)) and accounting for  $F_e$  factor obtained using CFD. Calculations were carried out using the computer program *GIB-ADAM* that has been tested and successfully verified on many occasions related to the implementation of laboratory tests as well as e.g., efficiency tests in hydropower plants [11]. Examples of the results measured or calculated for both modes of operation of the pump-turbine under investigation are shown in Figure 9. Measurements begin ca. 30–40 s before shut-off device start closing and end about 30–60 s after its complete closure or after extinction of the free pressure oscillation remaining in the flow system after the flow cut off. The time of closing the wicket gates of the tested machine was about 25 s and 20 s during turbine and pumping mode of operation, respectively. These time intervals were (8–10) times longer than the pipeline pressure wave period of about 2.5 s. Closing of the wicket gates was carried out in two stages in both modes—the faster stage followed by slower one. The reason for this common method of closing the wicket gates is to maintain the safety of the hydraulic system by preventing excessive pressure oscillations caused by too rapid shut-off of the flow, especially in the final phase of wicket gates closing.

The analysis of the influence of the above-mentioned and other parameters on the uncertainty of the results of the flow rate measurement with the applied method is presented in Appendix C.

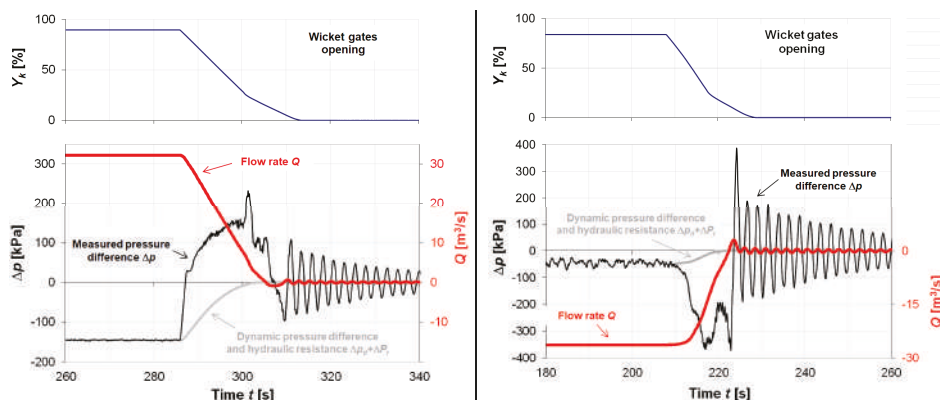


**Figure 9.** Examples of measured values of wicket gates opening and pressure difference and discharge through the machine calculated using the pressure time method. Left view: turbine operation mode, right view: pump operation mode.

### 3. Results and Discussion

The volumetric gauging method of flow measurement, due to the high requirements that must be met, is difficult to apply when testing real objects. For this reason, the examples of its practical application are quite rarely published. More valuable are the results presented in this paper, which were obtained for a pumped-storage power plant equipped with an artificial head water reservoir with known geometric characteristics. This made it possible to use the volumetric gauging method to measure the flow rate through the tested reversible hydrounit. The required narrow uncertainty band was obtained by supplementing the method with a special solution for accurate measurement of the water level change in the reservoir that also allowed including the impact of waves, as well as the amount of rainfall and leaks during measurements. It should be emphasized that measuring the upper water level in a standard way usually cannot ensure sufficient accuracy of the volumetric gauging method used for measuring flow in hydroelectric power plants.

The application of the pressure-time method to measure the flow rate in a real flow system with complex geometry additionally requires the use of an innovative calculation methodology to determine the  $F$ -factor—one of the critical parameters for maintaining a sufficiently narrow measurement uncertainty band. Owing to this factor, the geometrical characteristics of a pipeline measuring segment and impact of its flow elements on flow irregularities are taken into account. Disregarding changes in flow velocity profiles resulting from the variable shapes of pipeline elements leads to an increase in the inaccuracy of measurement using the pressure-time method, which cannot be corrected only by improving the modeling of friction losses in these elements, as discussed in [27–29] or by improving the computational model [22,28]. In addition, increasing the accuracy of estimation of the leakage rate through closed-flow shut-off devices is not enough [26]. In order to take into account changes in liquid velocity profiles in pipeline bends, the authors proposed a special calculation procedure (described in [24]) using CFD analysis for correction of the  $F$  factor. Verification of this procedure based on the analyzed examples confirmed that its application significantly increases the measurement accuracy of the pressure-time method. In this paper, the procedure based on CFD has been extended and used for piping systems with complex geometry (including curves, branches, conical elements, and inlets with changes in the shape of the flow section). In contrast to such a solution, the standard application of the pressure-time method does not provide the required uncertainty of flow rate measurement results. This innovative procedure provides the basis for using the pressure-time method in case of geometrically complex pipelines, and not only in turbine mode of operation, but also in the pump flow conditions of the tested reversible machine.

The uncertainties (standard and expanded) of the flow rate measurement results using both methods under consideration were as follows:

- Volumetric gauging method: standard and extended uncertainties were not greater than  $\pm 0.38\%$  and  $\pm 0.76\%$ , respectively, for all measured flow rates—Appendix B;
- Pressure-time method: standard and extended uncertainties were not greater than  $\pm 1.0\%$  and  $\pm 1.1\%$ , respectively, for all measured flow rates—Appendix C.

#### 3.1. Turbine Operation Mode

Because it was not possible to measure water discharge through the tested machine using both methods (volumetric gauging and pressure-time methods) simultaneously, the comparison of the results measured for the turbine operation mode was performed using the Winter–Kennedy method. According to this method, the measurement of discharge is based on the relationship between the discharge,  $Q$ , and the difference of pressures,  $\Delta p_{wk}$ , between the outer and the inner side of a spiral case of the machine under test:

$$Q = k\Delta p_{wk}^n \quad (8)$$

where  $k$  and  $n$  are constant coefficients experimentally determined during the calibration process. A value of the exponent,  $n$ , was assumed from the theory as equal to 0.5. Such assumption insignificantly

influenced the measuring results as was proven in [17] and it is negligible for purposes of comparison presented in this paper. For the tested machine, the values of  $k$  coefficient were determined independently on the basis of discharge measurement conducted using the volumetric gauging and the pressure-time methods—in Figure 10. The difference between  $k$  coefficient values obtained using these two different methods is very small, only about 0.2%. It should be emphasized that for the penstock geometrical factor,  $F$ , used in the pressure-time method without the  $\Delta f$  correction, the difference in the value of the  $k$  coefficient is slightly larger and amounts to approximately 0.33%. Although in the case under consideration the difference is not large, taking into account the various pipeline geometries that encounter in practice, it is recommended to support the pressure-time method by means of CFD analysis in the case of measuring sections of pipelines with irregular elements causing disturbances in the flow.

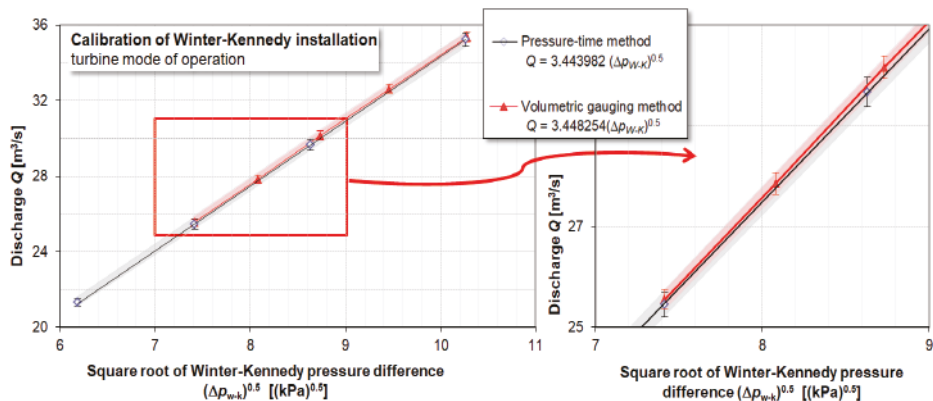


**Figure 10.** Turbine operation mode of the tested hydrounit: Comparison of the volumetric measurement method and the pressure-time method based on the results of calibration of the technical installation of the Winter–Kennedy method, with which the tested pump-turbine was equipped.

### 3.2. Pumping Operation Mode

The use of the Winter–Kennedy method for measuring flow rate in the pump mode of operation of hydraulic machines is not recommended by the standards [4–6]. This made it impossible to compare the pressure-time and volumetric gauging methods in a manner analogous to that used for turbine mode of operation, i.e., based on the results of simultaneous flow measurements. The comparison of results obtained using the analyzed methods was made by referring them to the head of the plant—Figure 11. The analysis also covered the impact of the penstock geometry irregularities on the results obtained using the pressure-time method. The differences between the discharge results obtained from the volumetric gauging method and pressure-time method were from  $-0.16\%$  to  $+0.58\%$  for lower (426 m) and higher head (439 m), respectively. Without correction of  $F$  geometrical factors, the differences were much greater—their values were  $+0.6\%$  and  $+1.35\%$ , correspondingly.

The comparison shows that the differences between the results obtained using the analyzed methods are much larger for pump mode of operation than for turbine mode of operation. At this stage of research, the causes of such observations cannot be clearly explained. Measurement of the hydraulic machine discharge using the pressure-time method is much more difficult to perform in pump operation than in turbine operation. This fact may suggest the reasons for this comparison results. This may also be the main reason why current standards do not recommend using this method in pump mode of operation of tested machines. However, it should be emphasized that the differences obtained in the analyzed case are still within the range of the measurement uncertainty characterizing the compared methods.

In addition, it should be emphasized that between the pump and turbine modes, in addition to obvious differences, there are those that can significantly affect the results obtained using the pressure-time method:

- Shutoff during pumping is characterized by much more irregular pressure changes than when cutting off flow during turbine mode of operation. This is related to the fact that during turbine operation, the flow was cut off while maintaining the generator connected to the network, while in pump operation, complete flow cut-off with the motor connected to the network was unacceptable.
- At the final stage of closing the machine's wicket gates, during pump operation, there is a short change in the direction of fluid flow—from the pump to the turbine direction;
- Due to the direction of flow, it should be noted that the pump operation mode, in contrast to the turbine operation mode, induces pressure pulsations with a much higher level, which propagate along the pipeline and have a direct impact on the measured pressure difference.
- The flow in the pump direction takes place along the expanding flow elements of the pipeline (diffusers), which is the reason for greater hydraulic losses (pressure losses occur due to local losses caused by greater turbulence in the boundary layers) and as a result requires greater correction of the  $F$  geometrical factor compared to turbine flow (and flow through the confusers).

Precise identification of how these differences may affect the final accuracy of flow measurement results obtained with the pressure-time method in the pump mode of operation of the hydraulic machines requires thorough professional testing and analysis. Currently, there is insufficient data on this topic, which hinders the extension of the applicability of this method and can also lead to excessive simplifications resulting in increased measurement uncertainty.

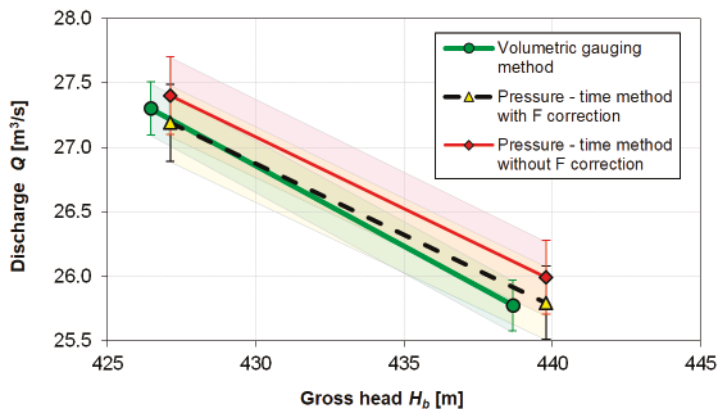


Figure 11. Pump operation mode of the tested hydrounit: Comparison of the discharges measured by the volumetric gauging method and the pressure-time method.

#### 4. Conclusions

The paper presents experiences concerning the use of the volumetric gauging method and the pressure-time method for measuring the water discharge through a reversible hydraulic machine at a pumped storage power plant. Research using these methods concerned both turbine and pump mode of operation of the tested machine. As part of the research, new original procedures have been used aimed at significant reduction of the measurement uncertainty.

In the case analyzed in the article by appropriate treatment consisting of the use of high-quality transducers, with the use of appropriate measurement techniques and procedures supporting the measurements of the flow rate with the use of both methods, a satisfactorily low measurement uncertainty was achieved.

The use of a high-class transducer measuring the pressure difference between the upper reservoir and the auxiliary tank in the volumetric gauging method, as well as the original method of analysis of the measured pressure difference, allowed to increase the accuracy of measuring the change in water volume over time significantly, and also allowed us to take into account water waving, which, when ignored, can meaningfully distort measurements.

The pressure-time method, which required taking into account the complex geometry of the pipeline connected to the tested hydrounit, was supported by CFD analysis of flow in the area of geometric irregularities (inlet, diameter changes, elbows, changes in cross-sectional shape). The original procedure using the results of this analysis provided the information necessary to introduce appropriate adjustments (correction) to the geometric factor  $F$ , which in turn, contributed to a significant reduction in the flow rate measurement uncertainty.

In contrast to the very good compliance of the results of discharge measurements obtained with the analyzed methods for the turbine operation of the tested machine (differences in the range of  $\pm 0.2\%$ ), in the case of pump operation, larger differences between the results were observed; however, they were still in the uncertainty band for measuring each of these methods independently (differences from  $-0.16\%$  to  $+0.58\%$ ). At this stage, it is difficult to clearly explain these observations. The authors point out the differences in the course of flow phenomena during shut-off in turbine and pumping operation carried out as part of tests executed using the pressure-time method. There is a need for further research to explain the reasons of the obtained differences and their influence on the accuracy of discharge measurement using the pressure-time method in pump operation mode.

It is worth emphasizing the positive effect achieved by using the CFD procedure to support the pressure-time method. A measure of this effect is the reduction of the differences between the measurement results obtained using the volumetric gauging method and the pressure-time method. In the turbine operation mode, the CFD-based correction of the  $F$  factor resulted in a 1.5-fold increase in the convergence of the compared results. In the case of pumping mode of operation, the convergence has improved several times (more than 2- to almost 5-fold, depending on the point of operation). This result proves the correctness of the assumptions made when using the CFD procedure and using its results for the pressure-time method of measuring the flow.

Particularly noteworthy are the results obtained for the pumping mode of operation, for which the use of the pressure-time method is not recommended by the standards. The comparison and consistency of these results with the results obtained with the volumetric gauging method confirmed the correctness of the assumptions underlying the proposed and applied modifications to the calculation procedure of the pressure-time method. This includes also the correct consideration of the temporary change in the flow direction occurring during its cutting off in the pumping mode of operation. Such experience from using this method in practice can help working out the relevant changes in the standards leading to the recommendation of the pressure-time method also for the pumping mode of reversible hydraulic machine operation.

**Author Contributions:** Conceptualization, A.A.; Data curation, W.J. and M.L.; Formal analysis, A.A.; Investigation, W.J. and M.L.; Methodology, W.J.; Software, W.J.; Supervision, A.A.; Validation, W.J. and M.L.; Visualization, M.L.; Writing—original draft, W.J. and M.L.; Writing—review & editing, A.A. All authors have read and agreed to the published version of the manuscript.

**Funding:** This research was financed from the statutory funds of The Szewalski Institute of Fluid Flow Machinery.

**Conflicts of Interest:** The authors declare no conflict of interest.

## Nomenclature

$A$	area; [m <sup>2</sup> ],
$D$	internal diameter of a pipeline; [m],
$e_k$	kinetic energy per unit of mass (specific kinetic energy); [J/kg],
$F$	geometrical factor of a pipeline; [m <sup>-1</sup> ],
$L, l$	pipeline length; [m],

$\dot{m}$	mass flow rate; [kg/s],
$p$	pressure; [Pa],
$Q$	volumetric flow rate; [m <sup>3</sup> /s],
$t$	time; [s],
$u$	absolute standard uncertainty,
$V$	water volume [m <sup>3</sup> ] or water flow velocity; [m/s],
$x$	distance along pipeline axis; [m],
$x, y, z$	coordinates; [m],
$Y$	turbine guide vane opening; [%],
$\Delta f$	relative deviation factor of F factor; [%],
$\rho$	liquid density; [kg/m <sup>3</sup> ],
$\delta$	relative standard uncertainty [%].

**Indexes**

$d$	dynamic pressure value,
$e$	equivalent value,
$f$	final value
$I$	total number of numerical cross-sections in a considered pipeline; [-],
$J$	total number of sub-segments with different dimensions (geometry) in a considered pipeline; [-],
$m$	average (mean) value,
$r$	hydraulic resistance
$0$	initial value.

**Appendix A. Procedure for Calculating Equivalent Geometrical F Factor in The Pressure-Time Method for Pipelines with Irregular Shape Sections of the on the Basis of CFD Analysis**

The determination of the geometrical  $F$ -factor from Equation (3) is fully acceptable for straight measuring sections of pipelines where there are no flow irregularities. This equation does not take into account changes in the flow velocity profiles in irregularly shaped pipeline elements, such as elbows, bifurcations, cones, pipe inlets, etc. Therefore, the authors of this paper recommend a special calculation procedure to consider the effect of these irregular shaped flow elements on the pressure-time measurement results.

The procedure shown below is an extension of the procedure for the curved pipe sections published in [24].

- Step 1:** Determination of the geometry of the considered pipeline flow system, discharge  $Q_j$ , etc., and the computational control flow space—Figure A1.
- Step 2:** Division of the computational control flow space into  $I$  numerical elements using cross-sections normal to the axis of the considered  $i$ -th ( $i = 1, 2, \dots, I$ ) pipe elements.

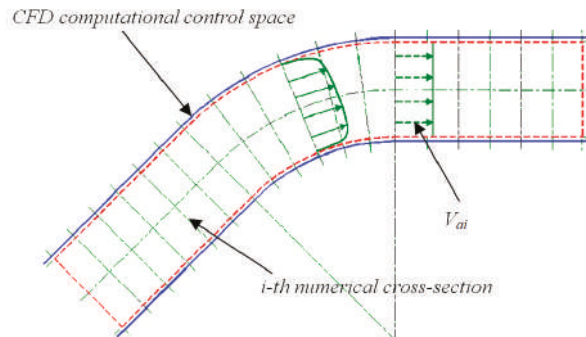


**Figure A1.** A pipe elbow with marked computational space.

**Step 3:** Simulation of velocity field  $V(x,y,z)$  in the flow elements of the considered pipeline within the frame of the computational control space using CFD computer software.

**Step 4:** Computation of mean flow velocity,  $V_{ai}$ , for each  $i$ -th numerical cross-section from the previously derived CFD results (step 3), and assumption of equal kinetic energy resulting from the simulated and the uniform flow velocity distributions:

$$e_{kCFDi} = e_{kai}; \quad \rho = const \tag{A1}$$

$$e_{kCFDi} = \frac{1}{\dot{m}} \iint_{A_i} \frac{1}{2} V_i^2 [\rho V_i dA] = \frac{\rho}{2\dot{m}} \iint_{A_i} V_i^3 dA; \quad \dot{m} = \rho V_{ai} A_i \tag{A2}$$

$$e_{kai} = \frac{1}{2} V_{ai}^2 = \frac{1}{2\dot{m}} \rho A_i V_{ai}^3 \tag{A3}$$

$$V_{ai} = \left[ \frac{\iint_{A_i} (V_i^3 dA)}{A_i} \right]^{1/3} \tag{A4}$$

where  $V_i$  is the flow velocity axial component—the component perpendicular to the  $i$ -th numerical cross-section.

**Step 5:** Computation of the equivalent cross-sectional area,  $A_{ei}$ , for each numerical cross-section ( $i = 1, 2, \dots, I$ ) using the continuity equation  $Q_j = V_{ai} A_{ei} = const$ :

$$A_{ei} = \frac{Q_j}{V_{ai}} \tag{A5}$$

**Step 6** Computation of coordinates of flow velocity centers in each  $i$ -th numerical cross-section,  $i = 1, 2, \dots, I$ :

$$x_{Ci} = \frac{\iint_{A_i} xV(x,y,z)dA}{V_{ai}A_{ei}}; \quad y_{Ci} = \frac{\iint_{A_i} yV(x,y,z)dA}{V_{ai}A_{ei}}; \quad z_{Ci} = \frac{\iint_{A_i} zV(x,y,z)dA}{V_{ai}A_{ei}} \tag{A6}$$

**Step 7:** For the considered flow rate  $Q_j$  through the analyzed pipe element, computing the equivalent factor  $F_{eQ_j}$  from the formula:

$$F_{eQ_j} = \sum_{i=1}^{I-1} \frac{l_{i \rightarrow i+1}}{0.5(A_{ei} + A_{ei+1})} \tag{A7}$$

where  $l_{i \rightarrow i+1}$  denotes the distance between the resultant velocity centers for computational sections  $i$  and  $i + 1$ ,  $A_{ei}$  and  $A_{ei+1}$ —equivalent areas of computational cross-sections  $i$  and  $i + 1$ , respectively.

The above computation should be performed for several discharge values ( $Q_j, j = 1, 2, \dots, m$ ) from the whole scope of its variation ( $Q_{\min} < Q_j \leq Q_{\max}$ ). The average value of equivalent factor,  $F_e$ , can be calculated from the relationship:

$$F_e = \frac{1}{m} \sum_{j=1}^m F_{eQ_j} \tag{A8}$$

In the above procedure, it was assumed that the changes in velocity profiles are the same under steady and transient flow conditions. This assumption is correct for cases where the flow shut devices are not closed very quickly when using the pressure-time method. Practically, such cases occur in all hydraulic machines, due to the need to protect their flow systems against the destructive effects of the water hammer phenomenon.

Taking the equivalent value of  $F_e$  instead of the value  $F$  calculated directly from the geometry of pipeline sections it is possible to increase the pressure-time method accuracy in cases when pipelines have irregular flow elements.

## Appendix B. Analysis of the Uncertainty of Measuring the Flow Rate by the Volumetric Gauging Method

The estimation of uncertainty of measuring the flow rate by the volumetric gauging method takes into account the following factors influencing the measured flow rate, both of a systematic and random nature:

1. Accuracy of geodetic measurements of the geometry of the head water reservoir of the power plant in order to determine the volume of water contained in it as a function of the water level
2. Accuracy class of the differential transducer used
3. The accuracy of the measurement data acquisition system used
4. Sampling frequencies of the differential transducer and accuracy of measuring the time interval in which the measurement took place
5. Selection of the time interval from  $t_0$  to  $t_f$ , used to calculate the change in the volume of water in the reservoir taking into account waves on water surface

The uncertainty of measurement of the water level change resulting from rainfall while it was occurring was disregarded as irrelevant. It was also assumed that uncertainties resulting from water evaporation and leaks through the concrete embankments of the reservoir and steel pipelines connected to it are negligible.

The uncertainty of determining gravitational acceleration and water density in the studied conditions was neglected as practically irrelevant in measuring the change in water level with a differential transducer, and, as follows from further considerations, very small uncertainties of time registration and water level changes related to the resolution of the applied data acquisition system were not taken into account.

The relative accuracy of determining the volume of the reservoir was determined at  $\delta\Delta V = 0.4\%$ , which resulted from the available documentation of the geodetic measurements of the reservoir, made more than 30 years ago after the completion of its construction. According to the principles, the relative standard uncertainty type B associated with it was determined as:

$$\delta_B(\Delta V) = \frac{\delta\Delta V}{\sqrt{3}} = \sim 0.23\% \quad (\text{A9})$$

The pressure difference transducer with the measuring range set at range  $\Delta z_{range} = 5$  m of water column and accuracy class  $K_z = 0.075\%$  was used to measure the water level change in the reservoir  $\Delta z$ . The standard uncertainty of type B concerning measurement of this quantity was calculated from the formula:

$$u_B(\Delta z) = \frac{K_z \cdot \Delta z_{range}}{\sqrt{3}} = \sim 0.0022 \text{ m w.c.} \quad (\text{A10})$$

Due to the fact that flow rate values were measured for the water level in the reservoir changing by at least 1 m, the relative standard uncertainty type B resulting from the measurement of this changes was not worse than:

$$\delta_B(\Delta z) \cong 0.22\% \quad (\text{A11})$$

For registering  $\Delta z$ , a computer data acquisition system with a measurement card of an absolute accuracy of  $\Delta_{DAQ} = 0.55$  mV was used. In order to determine the measurement uncertainty of the water level resulting from using such a measurement card, the scaling of the water level transducer should be taken into account (in the considered case the full measuring range of the transducer corresponded to

the voltage change  $U\Delta z_{range} = 3.5$  V). The standard uncertainty of water level measurement resulting from that can be determined using formula:

$$u_B(\Delta z_{DAQ}) = \frac{1}{\sqrt{3}} \frac{\Delta_{DAQ} \cdot \Delta z_{range}}{U_{\Delta z_{range}}} \cong \frac{1}{\sqrt{3}} \frac{0.00055 \cdot 5}{3.5} \cong 4.5 \cdot 10^{-4} \text{ m} \tag{A12}$$

After referring this uncertainty to the maintained minimum change of the water level in the reservoir (1 m of water), the relative standard uncertainty was not worse than:

$$\delta_B(r_{\Delta z}) \cong 0.05\% \tag{A13}$$

Type B standard uncertainty regarding the measurement of the time range from  $t_0$  to  $t_f$  and resulting from the accuracy and time resolution of a digital recorder (computerized data acquisition system) can be determined from the formula:

$$u_B(\Delta t) = \frac{\Delta_{tDAQ}(t_f - t_0)}{\sqrt{3}} \cong 0.1 \text{ s} \tag{A14}$$

where  $\Delta_{tDAQ} = 50 \times 10^{-6}$  is the time accuracy of the measuring card used in the data acquisition system, including its resolution.

Given the measurement time of each flow rate value that was not less than 1 h, the relative standard uncertainty of type B achieves negligible small value  $\delta_B(\Delta t) \cong 0\%$ .

The last of the above factors had random character and the standard uncertainty of type A that results was determined by statistical means. The recorded measurement signal of the water level change in the reservoir was characterized not only by changes resulting from waves on water surface, but also by random changes. The uncertainty arising from such nature of water changes was taken into account when calculating the  $Q_V$  value as described below. The calculations were started with the selection of the first time limits  $t_0$  and  $t_f$  corresponding to the intersection of the trend line with the recorded signal  $\Delta z(t)$ —Figure 3. Then, the  $t_0$  limit was shifted to the left to the next intersection of the trend line and the next  $Q_{Vi}$  value was calculated while maintaining the  $t_f$  limit. Then, the next  $Q_{Vi}$  calculations were made by shifting the  $t_0$  limit to the right from the original value to the intersection of the trend line with the signal  $\Delta z(t)$ . Similar calculations were carried out for the  $t_{ki}$  time limit shifted in a similar way. The obtained  $Q_{Vi}$  calculation results were then subjected to statistical analysis, i.e., the average  $Q_{Vm}$  value and standard uncertainty type A were calculated from the formula:

$$Q_{Vm} = \frac{1}{n} \sum_{i=1}^n Q_{Vi} \tag{A15}$$

$$u_A(Q_V) = k \sqrt{\frac{1}{n(n-1)} \sum_{i=1}^n (Q_{Vi} - Q_{Vm})^2} \tag{A16}$$

where  $k$  is the extension coefficients calculated for the Student's  $t$ -distribution at a confidence level of 68.2% and the number of degrees of freedom  $(n - 1)$ ,  $n$ —the number of  $Q_{Vi}$  values calculated.

The  $Q_{Vm}$  value was treated as the flow rate value measured by the method discussed. The uncertainty calculated according to the above procedure took different values depending on the measured case, but in none of the examined cases in relation to the measured flow rate was not greater than:

$$\delta_A(Q_V) = 0.2\% \tag{A17}$$

Finally, using the law of uncertainty propagation, the total relative standard uncertainty was determined from the formula:

$$\delta_c(Q_V) = \sqrt{\delta_A^2(Q_V) + \delta_B^2(\Delta V) + \delta_B^2(\Delta z) + \delta_B^2(r_z) + \delta_B^2(\Delta t)} \quad (\text{A18})$$

This value of this uncertainty is as follows:

$$\delta_c(Q_V) = \pm 0.38\% \quad (\text{A19})$$

It should be emphasized that the above-estimated standard uncertainty relates to a confidence level of about 68% and by using a coverage factor of  $k = 2$ , we obtain expanded uncertainty for measuring the flow rate by volumetric gauging method with a confidence level of about 95% of:

$$\delta(Q_V) = k \cdot \delta_c(Q_V) = \pm 0.76\% \quad (\text{A20})$$

A summary of the estimated uncertainty of measuring  $Q$  by the volumetric method is presented in Table A1.

**Table A1.** The results of calculations of uncertainty of the flow rate measurement results obtained using the volumetric gauging method.

Name	Designation	Value	Unit
relative uncertainty in determining the reservoir volume	$\delta(\Delta V)$	0.4000	%
relative standard uncertainty in determining the reservoir volume	$\delta_B(\Delta V)$	0.2309	%
standard uncertainty of water level measurement	$u_B(\Delta z)$	0.0022	m
relative standard uncertainty of measurement of water level related to a change in level of 1 m	$\delta_B(\Delta z)$	0.2165	%
standard uncertainty of water level measurement resulting from the measurement card used	$u_B(\Delta z_{DAQ})$	0.0005	m
relative standard uncertainty of water level measurement resulting from the measurement card used	$\delta_B(\Delta z_{DAQ})$	0.0454	%
standard uncertainty of time interval measurement	$u_B(\Delta t)$	0.1000	s
relative standard uncertainty of a time interval measurement	$\delta_B(\Delta t)$	0.0028	%
relative standard uncertainty due to the nature of the changes in the measured change in water level	$\delta_A(Q_v)$	0.2000	%
total standard uncertainty of flow rate measurement	$\delta_c(Q_v)$	0.3772	%
expanded uncertainty of flow rate measurement ( $k = 2$ )	$\delta(Q_v)_{k=2}$	0.7544	%

### Appendix C. Uncertainty Analysis of Flow Rate Measurements by Means of the Pressure-Time Method

Standards [4,6] specify the requirements that must be met so that the uncertainty of the flow rate measurement obtained using the pressure-time method is in the range of  $\pm 1.5\%$  (2.3%) according to [4] and  $\pm 1.0\%$  according to [6]. However, a way to calculate this uncertainty is not provided. The algorithm for estimating this uncertainty was the subject of only few available papers [36,37] but the presented algorithms do not comply with the applicable principles of expressing measurement uncertainty, presented in [19].

Below is a method for estimating the uncertainty of flow rate measurement under the considered conditions. The method is currently used by the authors of this contribution and complies with the recommendations presented in [19]. To present it, a simplified formulation of Equation (2) is introduced in the following form:

$$Q_0 = \frac{1}{\rho F} (\Delta p_m + \Delta p_{dm} + P_{rm})(t_f - t_0) + Q_f \quad (\text{A21})$$

where  $\Delta p_m$ ,  $\Delta p_{dm}$ , and  $P_{rm}$  are the values of  $\Delta p$ ,  $\Delta p_d$  and  $P_r$ , respectively, after averaging over the time interval from  $t_0$  to  $t_f$ .

Treating all the constituent quantities (components) in the above dependence as uncorrelated with each other, the value of the relative standard total uncertainty  $\delta_c(Q_0)$  can be calculated from the formula resulting from the law of uncertainty propagation:

$$\delta_c(Q_0) = \sqrt{\delta^2(\rho) + \delta^2(F) + \delta^2(\Delta p_m) + \delta^2(\Delta p_{dm}) + \delta^2(P_{rm}) + \delta^2(t_f - t_0) + \delta^2(Q_f)} \tag{A22}$$

The largest uncertainty component is related to the measurement and recording of the pressure difference. In the measurement procedure used by the authors of this work, the initially recorded pressure difference signal  $\Delta p(t_i)$  is numerically corrected taking into account characteristic of signal between limits  $t_f$  and  $t_{ff}$  as well as the flow rate at final conditions ( $Q_f$ ) and the  $C_r$  coefficient of frictional resistance characterizing the pipeline between measuring cross-sections. All measurement results of differential pressure values  $\Delta p(t_i)$  are corrected according to the formula:

$$\Delta p(t_i)_{correction} = \Delta p(t_i) - \left( \frac{1}{N_f} \sum_{t_f}^{t_{ff}} \Delta p(t_i) - C_r Q_f |Q_f| - \Delta p_{df} \right) \tag{A23}$$

where the second component on the right is the average value calculated from the recorded signal  $\Delta p(t_i)$  in the time interval  $(t_f, t_{ff})$ , i.e., in the phase of suppression of free pressure oscillations after the flow is cut off,  $N_f$  is the number of recorded values of  $\Delta p(t_i)$  in the time interval  $(t_f, t_{ff})$ , and  $\Delta p_{df}$  means the difference of dynamic pressures in the final steady state conditions (the method of calculating the difference of dynamic pressures is analogous to the calculation of the average difference of dynamic pressures—see the further part of the Appendix).

The  $C_r$  factor is determined from the formula (A23) on the basis of the measured pressure difference  $\Delta p_{0correction} = P_{r0} + \Delta p_{d0}$  caused by friction losses in the pipeline measuring section and dynamic pressure difference in the initial steady flow conditions, i.e., immediately before the closing of the flow shutoff device. Thus, the value of  $P_{r0}$  is calculated as the average of the measured pressure difference (after correction) in the time interval  $(t_{00}, t_0)$ :

$$P_{r0} = \Delta p_0 - \Delta p_{d0} = \frac{1}{N_0} \sum_{t_{00}}^{t_0} \Delta p(t_i)_{correction} - \Delta p_{d0} \tag{A24}$$

where  $N_0$  is the number of recorded values of  $\Delta p(t_i)$  in the time interval from  $t_i = t_{00}$  to  $t_i = t_0$ , and  $\Delta p_{d0}$  means the difference of dynamic pressures in the initial steady.

The method of correction according to formula (A23) allows us to get rid of the most important part of uncertainty arising from the exact determination of the “zero” pressure differential transducer. The residual uncertainty associated with it is estimated when analyzing the effect of  $t_f$  limit on the uncertainty value. It should be emphasized that the correction applied takes place in the iterative process of calculating the  $Q_0$  value.

Therefore, the mean pressure difference  $\Delta p_m$  is calculated from the measured and corrected values of  $\Delta p(t)_{correction}$  using the formula:

$$\Delta p_m = \frac{1}{N} \sum_{t_0}^{t_f} \Delta p(t_i)_{correction} \tag{A25}$$

where  $N$  is the number of recorded values of  $\Delta p(t_i)$  in the time interval from  $t_i = t_0$  to  $t_i = t_f$ .

The absolute standard uncertainty of type B measurement of pressure difference  $\Delta p$ , resulting from the classes of transducers used, was determined as follows:

$$u_{kB}(\Delta p_m) = \frac{K_{\Delta p} \cdot \Delta p_{range}}{\sqrt{3}} \quad (\text{A26})$$

After considering the pressure difference transducer class  $K_{\Delta p} = 0.075\%$  and its range  $\Delta p_{range} = \pm 500$  kPa (1 MPa), this uncertainty was:  $u_{kB}(\Delta p_m) = 0.43$  kPa.

To record  $\Delta p_m$ , a computer data acquisition system with a measurement card with an absolute accuracy of 0.55 mV was used. In order to determine the measurement uncertainty of the water level resulting from the used measurement card, the scaling of the level transducer should be taken into account (in the case under consideration the full width of the transducer measuring range corresponded to a 3.5 V voltage change). The resulting standard uncertainty of level measurement can be determined by the formula:

$$u_{rB}(\Delta p_m) = \frac{\Delta_{DAQ} \cdot \Delta p_{m-range}}{\sqrt{3} \cdot U_{\Delta p_{m-range}}} \cong \frac{0.00055 \cdot 1000}{\sqrt{3} \cdot 3.5} \cong 0.09 \text{ kPa} \quad (\text{A27})$$

In connection with the above, the total standard uncertainty  $u(\Delta p_m)$ , calculated from the formula:

$$u(\Delta p_m) = \sqrt{u_{kB}^2(\Delta p_m) + u_{rB}^2(\Delta p_m)} \quad (\text{A28})$$

was not worse than:

$$u(\Delta p_m) = 0.44 \text{ kPa}$$

After referring these uncertainty values to the average pressure difference increases caused by the inertia forces after flow cut-off during the measurement, i.e.,

$$\Delta p_{m-inertia} = (\Delta p_m + \Delta p_{dm} + P_{rm}) \quad (\text{A29})$$

the relative standard uncertainty  $\delta(\Delta p_m)$  is determined, which, together with other uncertainty components, has been presented in the uncertainty balance table Table A2. This uncertainty is approximately 0.36% and 0.43% for turbine and pump mode of operation, respectively.

In addition to the  $P_{r0}$  value resulting from the measurement and calculations, the values of friction pressure drop  $P_r$  during flow cut off are calculated according to the relationship (A24) in the time interval  $(t_0, t_f)$ . For this range, the average pressure drop  $P_{rm}$  can be calculated from the formula:

$$P_{rm} = \frac{C_r}{N_0} \sum_{t_0}^{t_f} Q(t_i) |Q(t_i)| - C_r Q_f |Q_f| - \Delta p_{df} \quad (\text{A30})$$

where  $N$  is the number of calculated  $Q(t_i)$  values in the range  $(t_0, t_f)$ . The values of the second and third components to the right of the above dependence are negligibly small, so it can be neglected when estimating their uncertainty.

The standard uncertainty type B resulting from the calculation of the  $P_{rm}$  value was estimated from the formula:

$$u_B(P_{rm}) = u(P_{rm}) = \frac{\delta_{P_{rm}} P_{rm}}{\sqrt{3}} \quad (\text{A31})$$

where  $\delta_{P_{rm}}$  is the average, relative difference in friction losses calculated using the quasi-stationary model (friction coefficient depending on the  $Re$  number) and the stationary model (constant friction coefficient)—the  $\delta_{P_{rm}}$  value was adopted according to approximately parabolic dependence of this difference on the flow rate proposed in monograph [11]:  $\delta_{P_{rm}} = \delta_{P_{rmax}}/3 = \sim 0.025/3 = 0.0083$ . It is worth emphasizing here that for calculating the flow rate,  $\delta_{P_{rm}}$  value was not used to correct friction loss calculations, i.e., the calculations were carried out assuming a constant  $C_r$  factor, not dependent on  $Re$ .

The effect of other factors on uncertainty  $u(P_{rm})$ , e.g., unsteadiness of flow, was omitted as irrelevant from the practical point of view. References [38,39] indicate that dissipation of mechanical energy during flow deceleration (taking place when the pressure-time method is applied) is only

slightly less than that obtained from the quasi-steady hypothesis. It is the opposite to accelerating flow where energy dissipation is much larger than according to the quasi-steady modeling. Some unsteady friction loss models in the closed conduits use these features [40]. These models have been confirmed experimentally—there is a high conformity between experimental and numerical results of the water hammer course [30]. With reference to the pressure-time method, the above assessment is confirmed by [27–29].

Finally, after the referring the  $u(P_{rm})$  to the value of  $\Delta p_{m-inertia}$ , the relative standard uncertainty associated with the calculation of  $P_r$ , for the highest value of flow rate measured is presented in the uncertainty balance table Table A2.

The uncertainty of calculating the dynamic pressure difference between the pipeline measuring cross-sections,  $u(\Delta p_{dm})$  was estimated as follows. The average dynamic pressure difference,  $\Delta p_{dm}$ , in the time interval  $(t_0, t_f)$  was calculated from the formula:

$$\Delta p_{dm} = \frac{1}{2} \left( \frac{\alpha_B \rho}{A_B^2} - \frac{\alpha_A \rho}{A_A^2} \right) \frac{1}{N} \sum_{t_0}^{t_f} [Q(t_i)]^2 \quad (\text{A32})$$

in which  $N$  denotes the number of calculated  $Q(t_i)$  values in the interval  $(t_0, t_f)$ , and  $A_A$  with  $A_B$  are the cross-sectional areas of the upper and lower pipeline measuring cross-sections, and  $\alpha_A$  and  $\alpha_B$ —Coriolis coefficients.

In the considered case, it was assumed that  $A_A = \infty$  and the effect of calculating  $\Delta p_m$  on the uncertainty of flow measurement results from changes in the Coriolis coefficient in the lower measuring cross-section of the pipeline. In calculations  $\alpha_B = 1.05$  was taken as the average value of the Coriolis coefficient for fully developed turbulent flow in the pipeline determined within the limits from 1.04 to 1.06 [23]. On this basis, the standard uncertainty type B resulting from the calculation of the  $\Delta p_{dm}$  value was calculated using the following formula:

$$u_B(\Delta p_{dm}) = \frac{0.01 \Delta p_{dm}}{\sqrt{3}} \quad (\text{A33})$$

For the cases with the highest values of measured flow rates, the values of standard uncertainty  $u(\Delta p_{dm})$  determined in this way was 0.21 kPa and 0.16 kPa for turbine and pump mode of operation, respectively.

Table A2 of the uncertainty balance lists the relative standard uncertainty associated with the calculation of  $\Delta p_{dm}$ , after relating  $u(\Delta p_{dm})$  to the value of  $\Delta p_{m-inertia}$  for the highest values of measured flow rates in the turbine and pump mode of operation of the tested machine.

The time accuracy of the computer acquisition system measuring the pressure difference signal  $p(t_i)$  was omitted as having no impact on the standard uncertainty type B regarding the measurement of the time interval from  $t_0$  to  $t_f$ . It can be calculated using the following formula:

$$u_B(\Delta t) = u_B(t_f - t_0) = \frac{\Delta_{tDAQ}(t_f - t_0)}{\sqrt{3}} \quad (\text{A34})$$

where  $\Delta_{tDAQ} = 50 \times 10^{-6}$  is the time accuracy of measurement card used in the data acquisition system including its resolution.

The value of  $u_B(t)$  is about 0.0007 s and 0.0005 s for turbine and pump mode of operation, respectively.

For the flow rate measurements, the time interval  $(t_0, t_f)$  during turbine mode of operation was not longer than  $T = \sim 25$  s, and during pump mode of operation  $T = \sim 20$  s, using a sampling frequency of 200 Hz. Table A2 of the uncertainty balance lists the relative standard uncertainty associated with the measurement of the time interval  $(t_0, t_f)$ .

The method of determining the  $t_f$  time limit, i.e., the upper limit of integration in the pressure-time method, was presented in [21]—an earlier author’s publication. This method significantly influences the uncertainty of measuring  $Q_0$  in cases where the free pressure oscillations after the closing of the shut-off device have relatively high amplitudes compared to the average  $\Delta p_m$  values. The value of  $t_f$  should be selected at the top of the peak or the bottom of the valley of free oscillations of pressure differences, with its exact determination taking place in the calculation program. It is recommended to choose the limit  $t_f$  from the first clear peak or valley of free oscillations in order to minimize the impact of these oscillations on the measurement result  $Q_0$ . Pulsations superimposed on these oscillations, which are random in nature, have been included in the estimation of uncertainty type A. For this reason, a series of calculations of  $Q_{0i}$  values for several values of time  $t_{fi}$ , selected in close proximity of the original value of  $t_f$  selected in accordance with the above principle, was carried out in the range covering only one valley and one peak visible in the measured quick-change pressure difference signal (pressure difference pulsation). It should be emphasized that it is not advisable to significantly shift the  $t_{fi}$  value from the tops of peaks and bottom of valleys of free differential pressure oscillations. The obtained  $Q_{0i}$  calculation results were subjected to statistical analysis, i.e., the average  $Q_{0m}$  value and standard uncertainty were calculated using the formula:

$$u_{t_{fA}}(Q_0) = k \sqrt{\frac{1}{n(n-1)} \sum_{i=1}^n (Q_{0i} - Q_{0m})^2} \quad (\text{A35})$$

where  $k$  is the extension coefficients calculated from the Student’s  $t$ -distribution for the confidence level  $p = 68.2\%$  and the number of degrees of freedom  $(n - 1)$ ,  $n$ —number of calculated  $Q_{0i}$  values.

After relating the  $u_{t_{fA}}(Q_0)$  values determined in the above described manner to the measured flow rate  $Q_0$ , the relative standard uncertainties  $\delta_{t_{fA}}$  did not exceed  $\delta_{t_{fA}}(Q_0) = 0.08\%$  for turbine mode of operation and  $\delta_{t_{fA}}(Q_0) = 0.1\%$  for pump mode of operation.

The uncertainty  $\delta(\rho)$  results from the variability of water density with pressure change and from the accuracy of its determination for given temperature and average absolute pressure in the pipeline occurring during tests. This uncertainty is very small; therefore, it was omitted in calculating the uncertainty of flow rate measurement.

The standard uncertainty  $\delta(F)$  for determining the geometric factor  $F$  results from the accuracy of measuring the length of individual pipeline segments ( $L_i$ ) and the area of their internal cross-sections ( $A_i$ ) and from the accuracy of the correction of the  $F$  factor using CFD calculations. The uncertainty of determining the  $F$  factor based on the available post-completion documentation of the pipeline, positively verified by direct measurement of  $L_i$  and  $A_i$ , was not worse than:

$$\delta(F_{geom}) = 0.15\% \quad (\text{A36})$$

Due to the fact that the uncertainty of the  $F$  factor correction introduced reaches about 0.75%, the uncertainty of this correction based on CFD calculations is of the same order assuming even 20% accuracy of CFD calculations, and as a result we get standard uncertainty:

$$\delta(F) = \sqrt{\delta^2(F_{geom}) + \delta^2(F_{CFD})} \cong 0.21\% \quad (\text{A37})$$

The flow rate under final conditions, being that the leakage through the closed wicket gates of the pump-turbine,  $Q_f$ , was measured in a separate way. For this purpose, under closed wicket gate conditions, pressure changes in the pipeline were recorded when closing the shut-off valve characterizing with very high tightness. On this basis, also using the pressure-time method,  $Q_f$  values were determined. For turbine mode of operation, it was equal  $Q_f = \sim 0.14 \text{ m}^3/\text{s}$ , while for pump mode of operation  $Q_f = \sim 0.18 \text{ m}^3/\text{s}$ , which is about 0.7% in relation to the minimum flow rate values for turbine

and about 0.65% for pump flow direction. No detailed analysis of the  $Q_f$  uncertainty was carried out, but it was assumed with a large excess that it is not worse than 10%, which gives uncertainty:

- $\delta(Q_f) = \sim 0.07\%$  for turbine mode of operation,
- $\delta(Q_f) = \sim 0.065\%$  for pump mode of operation.

The uncertainty resulting from the iterative algorithm for calculating the flow rate is  $\delta(Q_{0iter}) = 0.1\%$ . This is due to the condition used for ending the calculations, which assumes that the calculations are finished when two subsequent values  $Q_{0iter-1}$  and  $Q_{0iter}$  do not differ by more than 0.1%.

The balance of the estimated uncertainty of  $Q$  measurement using the pressure-time method is presented in Table A2.

**Table A2.** Summary results of calculations of uncertainty of flow rate results measured using the pressure-time method.

Name	Symbol	Value		Unit
		Turbine	Pump	
standard uncertainty of pressure measurement resulting from the applied differential pressure transducer	$u_{kB}(\Delta p_m)$	0.4330		kPa
standard uncertainty of pressure measurement resulting from the measurement card used	$u_{rB}(\Delta p_m)$	0.0907		kPa
total standard uncertainty of pressure measurement	$u(\Delta p_m)$	0.4424		kPa
relative standard uncertainty of pressure measurement related to the average differential pressure increase	$\delta(\Delta p_m)$	0.3600	0.4300	%
standard uncertainty of calculating friction losses	$u_B(P_{rm})$	0.0555	0.1458	kPa
relative standard uncertainty of calculating friction losses	$\delta_B(P_{rm})$	0.0584	0.1487	%
standard uncertainty of calculating the dynamic pressure difference	$u_B(\Delta p_{dm})$	0.2100	0.1600	kPa
relative standard uncertainty of calculating the dynamic pressure difference	$\delta(\Delta p_{dm})$	0.2211	0.1633	%
standard uncertainty of time interval measurement	$u_B(\Delta t)$	0.0007	0.0005	s
relative standard uncertainty of time measurement	$\delta_B(\Delta t)$	0.0029	0.0029	%
standard uncertainty resulting from setting the upper limit of integration	$u_{tFA}(Q_0)$	0.0270	0.0280	m <sup>3</sup> /s
relative uncertainty resulting from setting the upper limit of integration	$\delta_{tFA}(Q_0)$	0.0800	0.1000	%
standard uncertainty of determining the geometrical factor	$\delta(F_{geom})$	0.1500		%
standard uncertainty of CFD calculations	$\delta(F_{CFD})$	0.1500		%
total standard uncertainty of determining the geometric factor	$\delta(F)$	0.2100		%
uncertainty of determining the flow rate at final conditions	$\delta(Q_f)$	0.0700	0.0650	%
uncertainty resulting from iterative calculation of the flow rate	$\delta(Q_{iter})$	0.1000		%
relative total standard uncertainty	$\delta_c(Q_0)$	0.4973	0.5496	%
relative expanded uncertainty ( $k = 2$ )	$\delta(Q_0)_{k=2}$	0.9946	1.0991	%

## References

1. Merzkirch, W. *Fluid Mechanics of Flow Metering*; Merzkirch, W., Ed.; Springer: Berlin/Heidelberg, Germany; New York, NY, USA, 2005; ISBN 3-540-22242-1.
2. Miller, R.W. *Flow Measurement Engineering Handbook*, 3rd ed.; McGraw-Hill Book Company: New York, NY, USA, 1996.

3. Urquiza, G.; Basurto, M.A.; Castro, L.; Adamkowski, A.; Janicki, W. Flow measurement methods applied to hydro power plants, Chapter 7. In *Flow Measurement*; Urquiza, G., Castro, L., Eds.; INTECH Open Access Publisher: Rijeka, Croatia, 2012; pp. 151–168.
4. *Field Acceptance Tests to Determine the Hydraulic Performance of Hydraulic Turbines, Storage Pumps and Pump-Turbines*; IEC 41:1991; European Equivalent: EN 60041:1999; International Electrotechnical Commission: Geneva, Switzerland, 1991.
5. *Hydraulic Machines—Acceptance Tests of Small Hydroelectric Installations*; IEC 62006:2010; European Equivalent: EN 62006:2011; International Electrotechnical Commission: Geneva, Switzerland, 2010.
6. *Hydraulic Turbines and Pump-Turbines. Performance Test Codes*; ASME PTC 18 Standard; The American Society of Mechanical Engineers: New York, NY, USA, 2011.
7. Gibson, N.R. The Gibson method and apparatus for measuring the flow of water in closed conduits. *ASME Power Div.* **1923**, *45*, 343–392.
8. Gibson, N.R. Experience in the use of the Gibson method of water measurement for efficiency tests of hydraulic turbines. *ASME J. Basic Eng.* **1959**, *81*, 455–487. [[CrossRef](#)]
9. Voser, A.; Bruttin, C.; Prénat, J.-E.; Staubli, T. Improving acoustic flow measurement. *Water Power Dam Constr.* **1996**, *48*, 30–34.
10. Lüscher, B.; Staubli, T.; Tresch, T.; Gruber, P. Accuracy analysis of the acoustic discharge measurement using analytical, spatial velocity profiles. In Proceedings of the Hydro 2007, Granada, Spain, 15–17 October 2007. Paper 17.05.
11. Adamkowski, A. Discharge measurement techniques in hydropower systems with emphasis on the pressure-time method. Chapter 5. In *Hydropower—Practice and Application*; Hossein, S.-B., Ed.; INTECH Open Access Publisher: London, UK, 2012; pp. 83–114.
12. Doering, J.C.; Hans, P.D. Turbine discharge measurement by the velocity-area method. *J. Hydraul. Eng.* **2001**, *127*, 747–752. [[CrossRef](#)]
13. Gandhi, B.K.; Verma, H.K. Simultaneous multi-point velocity measurement using propeller current meters for discharge evaluation in small hydropower stations. In Proceedings of the International Conference on Small Hydropower Hydro Sri Lanka, Kandy, Sri Lanka, 22–24 October 2007.
14. Proulx, G.; Cloutier, E.; Bouhadji, L.; Lemon, D. Comparison of discharge measurement by current meter and acoustic scintillation methods at La Grande-1. In Proceedings of the IGHEM, Luzern, Swiss, 14–16 July 2004.
15. Lobet, J.V.; Lemon, D.D.; Buermans, J.; Billenness, D. Union Fenosa Generación’s field experience with Acoustic Scintillation Flow Measurement. In Proceedings of the IGHEM, Milan, Italy, 3–6 September 2008.
16. Adamkowski, A.; Janicki, W.; Krzemianowski, Z.; Lewandowski, M. Volumetric gauging method vs Gibson method—Comparative analysis of the measurement results of discharge through pump-turbine in both operation modes. In Proceedings of the IGHEM 2016, Linz, Austria, 24–26 August 2016; p. 567.
17. Adamkowski, A.; Lewandowski, M. Some experiences with flow measurement in bulb turbines using the differential pressure method. *IOP Conf. Ser. Earth Environ. Sci.* **2012**, *15*, 062045. [[CrossRef](#)]
18. Adamkowski, A.; Lewandowski, M.; Lewandowski, S.; Cicholski, W. Calculation of the cycle efficiency coefficient of pumped-storage power plant units basing on measurements of water level in the head (tail) water reservoir. In Proceedings of the 13th International Seminar on Hydropower Plants, Vienna, Austria, 24–26 November 2004.
19. *Uncertainty of Measurement—Part 3: Guide to the Expression of Uncertainty in Measurement*; (GUM: 1995), ISO/IEC GUIDE 98-3:2008; International Organization for Standardization: Geneva, Switzerland, 2008.
20. Çengel, Y.A.; Cimbala, J.M. *Fluid Mechanics. Fundamentals and Applications*; McGraw-Hill Book Company: New York, NY, USA, 2006.
21. White, F.M. *Fluid Mechanics*; WCB/McGraw-Hill: Boston, MA, USA, 1999.
22. Adamkowski, A.; Janicki, W. Elastic water-hammer theory-based approach to discharge calculation in the pressure-time Method. *J. Hydraul. Eng.* **2017**, *143*, 06017002. [[CrossRef](#)]
23. Adamkowski, A.; Janicki, W.; Krzemianowski, Z.; Lewandowski, M. Flow rate measurements in hydropower plants using the pressure-time method—Experiences and improvements. *Flow Meas. Instrum.* **2019**, *68*, 101584. [[CrossRef](#)]
24. Adamkowski, A.; Krzemianowski, Z.; Janicki, W. Improved Discharge Measurement Using the Pressure-Time Method in a Hydropower Plant Curved Penstock. *ASME J. Eng. Gas Turbines Power* **2009**, *131*, 053003. [[CrossRef](#)]

25. Adamkowski, A.; Janicki, W. Selected problems in calculation procedures for the Gibson discharge measurement method. In Proceedings of the IGHEM, Roorkee, India, 21–23 October 2010; pp. 73–80.
26. Bortoni, E.C. New developments in Gibson’s method for flow measurement in hydro power plants. *Flow Meas. Instrum.* **2008**, *19*, 385–390. [[CrossRef](#)]
27. Jonsson, P.P.; Ramdal, J.; Cervantes, M.J. Development of the Gibson method—Unsteady friction. *Flow Meas. Instrum.* **2012**, *23*, 19–25. [[CrossRef](#)]
28. Dunca, G.; Iovănel, R.G.; Bucur, D.M.; Cervantes, M.J. On the Use of the Water Hammer Equations with Time Dependent Friction during a Valve Closure, for Discharge Estimation. *J. Appl. Fluid Mech.* **2016**, *9*, 2427–2434. [[CrossRef](#)]
29. Sundstrom, L.R.J.; Saemi, S.; Raisee, M.; Cervantes, M.J. Improved frictional modeling for the pressure-time method. *Flow Meas. Instrum.* **2019**, *69*, 101604. [[CrossRef](#)]
30. Adamkowski, A.; Lewandowski, M. Experimental Examination of Unsteady Friction Models for Transient Pipe Flow Simulation. *ASME J. Fluids Eng.* **2006**, *128*, 1351–1363. [[CrossRef](#)]
31. NUMECA International—Computational Fluid Dynamics Software and Consulting Service. Available online: <https://www.numeca.com> (accessed on 15 August 2020).
32. ANSYS Inc. *ANSYS Fluent User’s Guide 18*; Release 18; ANSYS Inc.: Canonsburg, PA, USA, 2017.
33. Menter, F.R. Two-equation eddy-viscosity turbulence models for engineering applications. *AIAA J.* **1994**, *32*, 269–289. [[CrossRef](#)]
34. Wilcox, D.C. *Turbulence Modeling for CFD*; DCW Industries, Inc.: La Canada, CA, USA, 1993.
35. Hellsten, A.; Laine, S. *Extension of the k- $\omega$ -SST Turbulence Models for Flows over Rough Surfaces*; AIAA Paper; AIAA-97-3577; AIAA: Reston, VA, USA, 1997. [[CrossRef](#)]
36. Ramdal, J.; Jonsson, P.P.; Dahlhaug, O.G.; Nielsen, T.K.; Cervantes, M. Uncertainties for pressure-time efficiency measurements. In Proceedings of the IGHEM 2010, Roorkee, India, 21–23 October 2010; pp. 64–72.
37. Hulås, H.; Dahlhaug, O.G. Uncertainty analysis of Pressure-Time measurements. In Proceedings of the IGHEM 2006, Portland, OR, USA, 30 July–1 August 2006; pp. 1–13.
38. Brunone, B.; Golia, U.M.; Greco, M. Some Remarks on the Momentum Equations for Fast Transients. In Proceedings of the 9th Round Table, IAHR, International Meeting on Hydraulic Transients with Column Separation, Valencia, Spain, 4–6 September 1991; pp. 201–209.
39. Bughazem, M.B.; Anderson, A. Problems with Simple Models for Damping in Unsteady Flow. In Proceedings of the International Conference on Pressure Surges and Fluid Transients, BHR Group, Harrogate, UK, 16–18 April 1994; pp. 537–548.
40. Vitkovsky, J.P.; Lambert, M.F.; Simpson, A.R.; Bergant, A. Advances in Unsteady Friction Modeling in Transient Pipe Flow. In Proceedings of the 8th International Conference on Pressure Surges, The Hague, The Netherlands, 12–14 April 2000; pp. 471–482.



© 2020 by the authors. Licensee MDPI, Basel, Switzerland. This article is an open access article distributed under the terms and conditions of the Creative Commons Attribution (CC BY) license (<http://creativecommons.org/licenses/by/4.0/>).

Article

# Differences of Flow Patterns and Pressure Pulsations in Four Prototype Pump-Turbines during Runaway Transient Processes

Zhiyan Yang <sup>1</sup>, Zirui Liu <sup>1</sup>, Yongguang Cheng <sup>1,\*</sup>, Xiaoxi Zhang <sup>2</sup>, Ke Liu <sup>1</sup> and Linsheng Xia <sup>3</sup>

<sup>1</sup> State Key Laboratory of Water Resources and Hydropower Engineering Science, Wuhan University, Wuhan 430072, China; mry@whu.edu.cn (Z.Y.); liuzr97@whu.edu.cn (Z.L.); liukeyf@whu.edu.cn (K.L.)

<sup>2</sup> School of Environmental Science and Engineering, Xiamen University of Technology, Xiamen 361024, China; zhangxiaoxi@xmut.edu.cn

<sup>3</sup> China Ship Development and Design Center, Wuhan 430064, China; xialinsheng@whu.edu.cn

\* Correspondence: ygcheng@whu.edu.cn

Received: 24 August 2020; Accepted: 5 October 2020; Published: 11 October 2020

**Abstract:** Frequent working condition conversions in pumped-storage power stations often induce stability problems, especially when the operating point enters the S-shaped region, during which flow transitions and pressure fluctuations are serious. The pump-turbines with different specific speed values show different characteristics, but their differences in stability features are still not clear. In this study, four different pump-turbines were selected to simulate the runaway processes from turbine modes. The similarities and differences of flow patterns and pressure fluctuations were analyzed. For the similarities, pressure pulsations increase gradually and fluctuate suddenly once the backflows occur at the runner inlets. For the differences, the evolutions of backflows and pressure pulsations are related to specific speeds and runner shapes. Firstly, it is easier for the lower specific speed turbines to enter the reverse pump mode. Secondly, the blade lean angle influences the position where backflows occur, because it determines the pressure gradient at the runner inlets. Thirdly, the runner inlet height influences pressure pulsations in the vaneless space, because the relative range of backflow transitions will be enlarged with the decrease of specific speed. Overall, investigating the mechanisms of flow pattern transitions and pressure variations is important for runner design and transient process control.

**Keywords:** pump-turbine; flow patterns; pressure pulsations; similarities; differences; S-shaped characteristics; runaway transient process

## 1. Introduction

With the substantial increase of electricity consumption and the rapid development of green sustainable energies, pumped-storage power undertakes the functions of peak load regulation, valley filling, frequency modulation, phase modulation, and emergency standby in the power grids [1,2]. Its match-up with nuclear power and complement with wind and solar powers make it an indispensable tool to ensure safety, stability, and efficiency of clean energies [3–5]. To undertake these important functions, the stability and safety of pumped-storage power systems are essential. However, some stability problems in operating pumped-storage power stations, such as violent vibration of pump-turbine units [6], grid connection failure [7,8], runner lifting-up [9], and rotor-stator crashing [10], were frequently reported. These problems were generally attributed to the frequent conversions of operating conditions, especially when the working points pass through the so-called S- and hump-shaped characteristics regions, in which intense flow and pressure fluctuations occur. To know the mechanism, solve the stability problems, and predict working conditions, many studies on the transient processes of pump-turbine generator units were conducted in recent years [11].

Among many transient processes, the runaway process is the most dangerous one. Even if this scenario, it is rarely seen in practical operation, predicting the risk in the design phase is always required. The runaway process happens if the generator is cut from the power grid but the guide-vanes fail to close. Without retarding torque, the runner will be driven only by the unceasing water power, and the unit will be accelerated to the runaway speed. During this process, the working point slides rapidly through the S-shaped characteristic region that is comprised of the high-speed turbine, turbine braking and reverse pump modes, and violent vibrations in the unit happen due to quick flow pattern transitions and strong pressure pulsations [1]. Therefore, it is very important to ensure the safety and stability of the unit by analyzing the laws of flow pattern transitions and pressure pulsation changes, and revealing the interrelations of these key factors.

The existing studies about the runaway instability of pump-turbines mainly focused on unsteady flow patterns and pressure pulsations in the runner and vaneless space [12,13]. Two main situations [11,12], working at a runaway point and running away from a turbine working point, were both investigated. They concluded that strong backflows and vortices in the runner and the vaneless space lead to large pressure pulsations, channel blockage, discharge decrease, and pressure increase [12]. As for the simulations about static working at a runaway point, Gentner et al. [14] found toroid-like vortex structures around the vaneless space, and claimed that the secondary vortex in each runner channel can cause negative head gradient and pressure rise. Wang et al. [15] captured the obviously detached vortices on the pressure sides of blades near the crown and pointed out that they may be the very reason for huge pressure fluctuations. Widmer et al. [16] showed the flow separation, recirculation, and vortex formation in every runner channels of a pump-turbine operating at the speed-no-load condition, and observed the obvious backflows and pressure fluctuations. Hasmatuchi et al. [17] investigated the flow distribution near the runaway point through experiments and found that the low-frequency pressure components can be captured in the spiral-casing and the guide-vanes channel. Jacquet et al. [18] pointed out that the position of backflows at the runner inlet depended on the operating point, and the accompanying pressure fluctuations can reach the maximum at the speed-no-load condition.

As for transient process studies, Trivedi et al. [19–22] concluded that the highest amplitudes of pressure fluctuations in pump-turbine were under the running away condition, according to the measurement of pressure fluctuations in the speed-no-load, running away, total load rejection, start-up, and shut-down conditions. Yin et al. [23] showed that the vortex formation at the runner inlet severely blocks the runner passages periodically, inducing torque and rotational speed fluctuations. Zhang et al. [24] also simulated the runaway process by computational fluid dynamics (CFD) and found that the successive features of transient flow patterns may induce pressure differences between the similar dynamic operating points in different moving directions. Xia et al. [1] conducted simulations of runaway processes of a model pump-turbine with different guide-vane openings (GVOs), and found that the backflows at the runner inlet can lead to quite different pressure fluctuations. Other research investigating the runaway instability by specifying discharge oscillating boundary condition at the turbine inlet or draft-tube outlet were also conducted. For example, Widmer et al. [16] decreased the discharge at the boundary starting from the runaway point, and found that the pressure pulsations can generate abnormal low-frequency signals with the number of stalled channels increased, which was similar to those in the runaway process.

The research discussed above shows that whether at the runaway point or during runaway process, flow blockages and severe pressure fluctuations are strong in the runner and vaneless space, which are the common features in pump-turbines. However, in much reported research, the problems encountered by different pump-turbines are mostly different. For example, a runner lifting-up happened in Tianhuangping power station during a load increase process [9], many grid connecting failures occurred in Baoquan power station under low head conditions [8], and a rotor-stator collision happened in Huizhou power station during a load rejection process [25]. Besides these accidents, there are still many other accidents that need to be paid attention to. Although these accidents are related to many

factors, it is undeniable that the characteristics of the pump-turbine itself have a great influence on them. Most obviously, different pump-turbines have different S-characteristics because of their rated output, head, discharge, rotational speed, along with their runner shapes being different. Therefore, the flow patterns and pressure pulsations may not be similar in local and detailed perspectives, which may be related to the different problems mentioned above. For example, the conclusions in Hasmatuchi [17] and Jacquet [18] are different. In Hasmatuchi's paper, the low-frequency component will further increase in amplitude as the zero-discharge condition is approached, while those in Jacquet's paper reach at the maximum at the no-load conditions. In addition, Zhou et al. [26] optimized the blade inlet and showed the different developing trends of flow patterns and pressure fluctuations of two turbines during the runaway processes, though other geometry features of turbines were kept unchanged.

Therefore, we should not only focus on the common phenomena, but also the differences in different pump-turbines, in order to better understand the mechanism and solve the problems. As a common convention, the characteristics of pump-turbines are always labelled by their specific speeds. However, no research shows whether runaway process characteristics are related to the specific speed. These characteristics include the attenuation of runaway, the transition of flow patterns, the fluctuations of pressure pulsations, and runner forces. In order to answer these questions, we selected four prototype pump-turbines with different water heads, and simulated their runaway transient processes from the turbine mode. The evolutions of pressure pulsations and flow patterns were analyzed, their similarities and differences were discussed, and the mechanism was revealed. The paper will be arranged as follows: the Section 2 describes the basic simulation model and parameters; the Section 3 shows the resulting histories of macro parameters, and the evolutions of flow structures and pressure pulsations, along with their relations with specific speeds; the Section 4 explains the influences of runner shapes for the differences in the evolutions of flow structures and pressure pulsations; and conclusions are drawn in the Section 5.

## 2. Three-Dimensional CFD Setups

**Software for simulation:** Three-dimensional (3D) CFD simulations were carried out by using commercial software ANSYS FLUENT 17.0 (ANSYS, Canonsburg, PA, USA).

**Computational domain:** four pump-turbines with different specific speeds were selected. Because of their main parameters, such as head, discharge, output, and layout out of water conveyance systems are different, it is difficult to ensure that all the settings in the simulations are the same, which is also unrealistic. Therefore, in order to fully reflect the characteristics of the pump-turbines during the transient process, the actual water conveyance systems were removed in the simulations to eliminate the impact of flow inertia in water conveyance systems [1]. This removal will affect the variation period and maximum value of macro parameters due to the flow inertia in pipelines, but we mainly focused on the evolutions of flow patterns and pressure pulsations, which are more affected by the pump-turbine unit. In addition, two extended tubes were added to the inlets of spiral-casings and the outlets of draft-tubes for setting boundary conditions at the locations with smooth flow patterns. Also, a conventional hydraulic turbine was chosen to compare with the above four pump-turbines. The 3D computational domains and monitoring points of the five turbines are shown in Figure 1, and the main parameters are listed in Table 1. The specific speed is defined by  $n_s = n_r \sqrt{N_r} / H_r^{1.25}$ , in which  $n_r$ ,  $N_r$ , and  $H_r$  are the rated rotational speed, output, and head, respectively. The flow patterns have a certain regularity in  $n_{11}$ - $Q_{11}$  plane under large guide vane opening conditions, especially at the runner inlets (in one pump-turbine) [1]. Therefore, the runaway processes of the four pump-turbines are all started near their corresponding rated turbine working conditions, while that of the conventional hydraulic turbine is started from a large guide vane opening condition, in which the runaway characteristics are similar to those in the rated one.

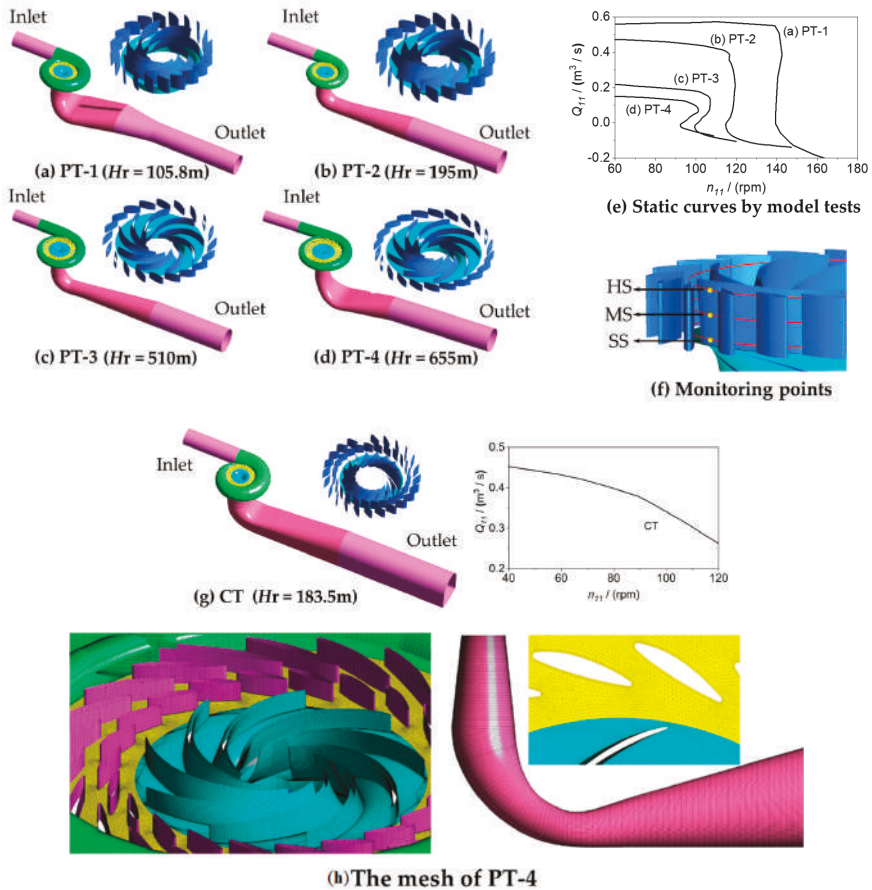


Figure 1. Computational domains of the pump-turbines (PT) and conventional turbine (CT), the schematic of monitoring points, and mesh information.

Table 1. Main parameters of the four pump-turbines and a turbine.

-	Specific-Speed $n_s$ (m·kW)	Rated Head $H_r$ (m)	Rated Output $N_r$ (MW)	Diameter of Runner Inlet $D$ (m)	Height of Runner Inlet $b_0$ (m)	Relative Runner Inlet $b_0/D$ (-)	Number of Runner Blades (-)	Inertia of Rotating Parts $GD^2$ ( $\times 10^7$ kg·m <sup>2</sup> )
PT-1	219.8	105.8	139	5.23	1.12	0.214	7	1.092
PT-2	189.8	195.0	306	5.26	0.79	0.150	9	1.092
PT-3	114.1	510.0	306	3.82	0.34	0.089	9	1.092
PT-4	90.2	655.0	357	4.23	0.30	0.071	9	1.092
CT	148.4	183.5	466	6.0	1.08	0.180	16	1.092

Mesh Generation: The upstream and downstream extended tubes, spiral-casings, runners, and draft-tubes were discretized by hexahedral structure grids, while the vane regions were discretized by wedge grids. Also, the areas near the blades and guide-vanes were locally refined. Grid refinement evaluations were performed for each pump-turbine and we found that when the grid number is more than 5.0 million, the relative differences in resulting macro parameters under steady conditions are negligible. Therefore, the cell numbers of the five turbines are 5.42 million, 5.58 million, 5.76 million, 5.97 million, and 5.54 million, respectively.

**Numerical Scheme:** After many comparisons, considering the calculation time and accuracy at the same time, we selected the timesteps for the five turbines as 0.00125, 0.001, 0.001, 0.001, and 0.00166667 s, corresponding to the times needed for the runner to rotate 1.5, 1.5, 3.0, 3.0, and 1.5 degrees, respectively. The SST-based scale-adaptive simulation model (SAS-SST) turbulence model [1] was adopted, and all the convergence criteria of residuals at each timestep were set to  $1.0 \times 10^{-4}$ , including continuity, x-velocity, y-velocity, z-velocity, k, and omega. For both steady and unsteady simulations, the SIMPLEC algorithm was chosen to achieve the coupling solution of the velocity and pressure equations [1].

**Boundary Conditions:** The total pressure was defined at the inlet of the extended pipe of the spiral-casing, and the static pressure was defined at the outlet of the extended pipe of the draft-tube. The remaining solid walls were imposed with the no-slip wall condition.

### 3. Results of the Runaway Transient Processes

#### 3.1. Macro Parameters Histories

The runaway dynamic characteristics of the four pump-turbines are shown in  $n_{11}$ - $Q_{11}$  plane in Figure 2, in which the unit parameters are defined as  $n_{11} = nD_1 / \sqrt{H}$  and  $Q_{11} = Q / (D_1^2 \sqrt{H})$ , where  $H = E1 - E2$ , with  $E1$  and  $E2$  the total energy values at the spiral-casing inlet and runner outlet, respectively. Comparing the computed results (red lines) of the four pump-turbines, we know that the dynamic trajectories of PT-1 and PT-2 have very high amplitudes in high frequency pulsation signals in the  $n_{11}$ - $Q_{11}$  plane, while those of PT-3 and PT-4 are relatively smaller and become obvious only near the runaway points. In addition, the low-pass filtered curves (green lines) of the original data do not go along the static characteristic curves (black lines) obtained from the model tests, however, they have good agreements before entering the S-shaped region. Once entering the S-shaped region, the dynamic curves deviate from the measured static ones. These deviations have been analyzed in [27], in which the influences of the sections for head definition, the water inertia in pipes and the rotational inertia of unit on the dynamic trajectory were discussed. In this paper, due to neglecting water inertia in pipes and choosing the same rotational inertias, the deviations are different. In fact, the simulating rotational inertia is based on the actual value of PT-1, therefore, the actual rotational inertia of PT-2 is much larger, and those of PT-3 and PT-4 are much smaller. For PT-2, small simulating rotational inertia will lead to large speed increasing rate, then the dynamic trajectory is on the right side of the static curve obviously, which is opposite to the phenomenon in PT-3 and PT-4. To verify the rationality of the above settings and results, we take reference [28] as an example, in which the influence of the inertia of rotating part has been well explained, and it shows that the dynamic trajectories affected by different rotating part inertia in  $n_{11}$ - $Q_{11}$  plane are very similar with those in this paper. In addition, there is no very large deviation in the dynamic trajectories, though the pulsations in the  $n_{11}$ - $Q_{11}$  plane and variation period of rotational speed are different. From the above analysis, we know that the results of transient process are quite different from the static ones and it is necessary to consider the dynamic effect in transient simulations.

The time histories of the main macro parameters during the runaway processes are also shown in Figure 2. Generally speaking, the dynamic histories of PT-1 and PT-2 show damped oscillations, while those of PT-3 and PT-4 demonstrate undamped oscillations. The working points of PT-1 and PT-2 go through the turbine (T) and turbine braking (TB) modes, but do not enter the reverse pump (RP) mode, and the macro parameters fluctuate in the T and TB regions with gradually decreasing amplitudes. On the other hand, the working points of PT-3 and PT-4 not only go across the T and TB modes, but also go down to the RP mode, and fluctuate periodically in these three modes. Overall, the fluctuation periods of the macro variables of the four pump-turbines are about 11.5, 10, 14.4, and 9.6 s, respectively, though the inertia values of rotating parts are the same (Table 1) in the simulations. The periods are also influenced by the rated rotating speed, discharge, and output. In addition, the maximum rotational speeds are heavily affected by the above factors [27,28], and can reach more than 1.4 times that of the initial value in PT-1 but less than 1.2 times in PT-4.

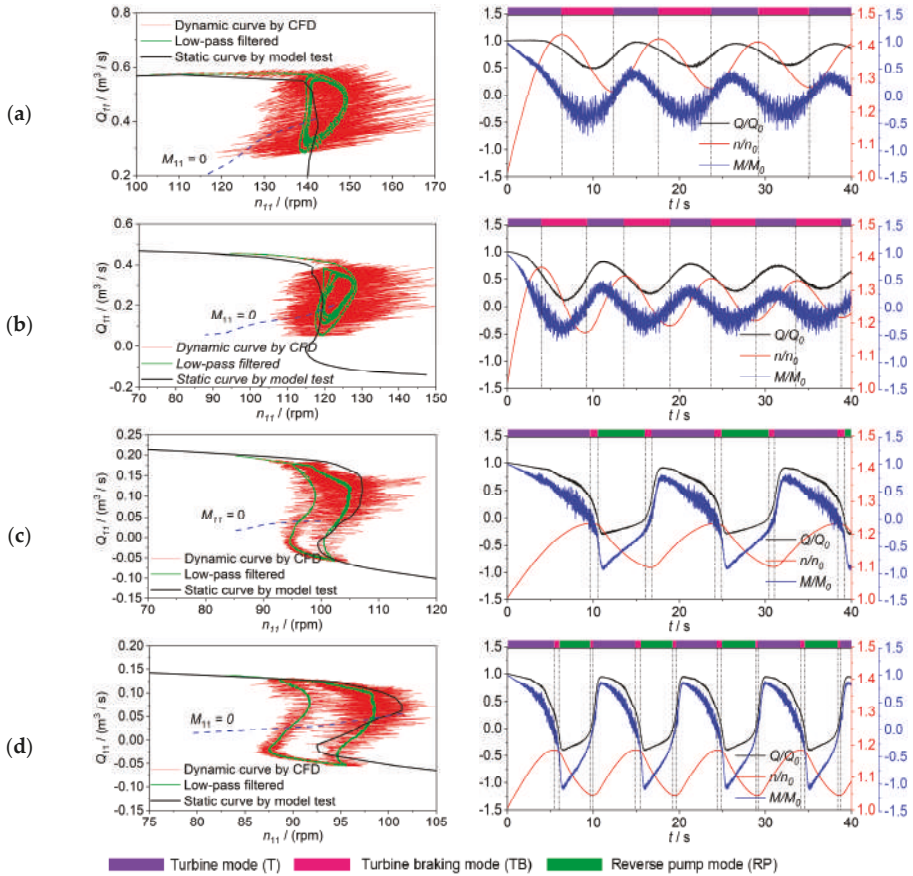


**Figure 2.** Working point trajectories and parameter histories of the four pump-turbines: (a) PT-1, (b) PT-2, (c) PT-3, (d) PT-4.

3.2. Radial Velocity Variations and Backflow Transitions at the Runner Inlets

The aforementioned fluctuations of dynamic trajectories are closely related to the unstable flow patterns near the runner inlets and outlets [29]. The variations of flow velocity at the runner inlet can reasonably demonstrate the characteristics of flow evolutions during the runaway processes. Figure 3 show the variations of normalized radial velocity  $v_r$  at the three monitoring points (HS, MS, and SS shown in Figure 1f, namely hub side, mid span and shroud side, respectively) in the four runners. The normalized velocities were defined by:

$$v_r = \frac{60U_r}{\pi n_1 D_1} \tag{1}$$

where  $U_r$  is the instantaneous radial velocity,  $n_1$  is the initial rotational speed, and  $D_1$  is the runner inlet diameter. Here, positive values of  $v_r$  are defined as the direction of water flowing into the runner passages, while negative values of  $v_r$  mean the backflows from the runner passages to the vaneless space. In addition,  $v_r$  (O) and  $v_r$  (L), in Figure 3, are the original and low-pass filtered data, respectively, and the upper frequency limit of low-pass filtered data is 2 Hz.

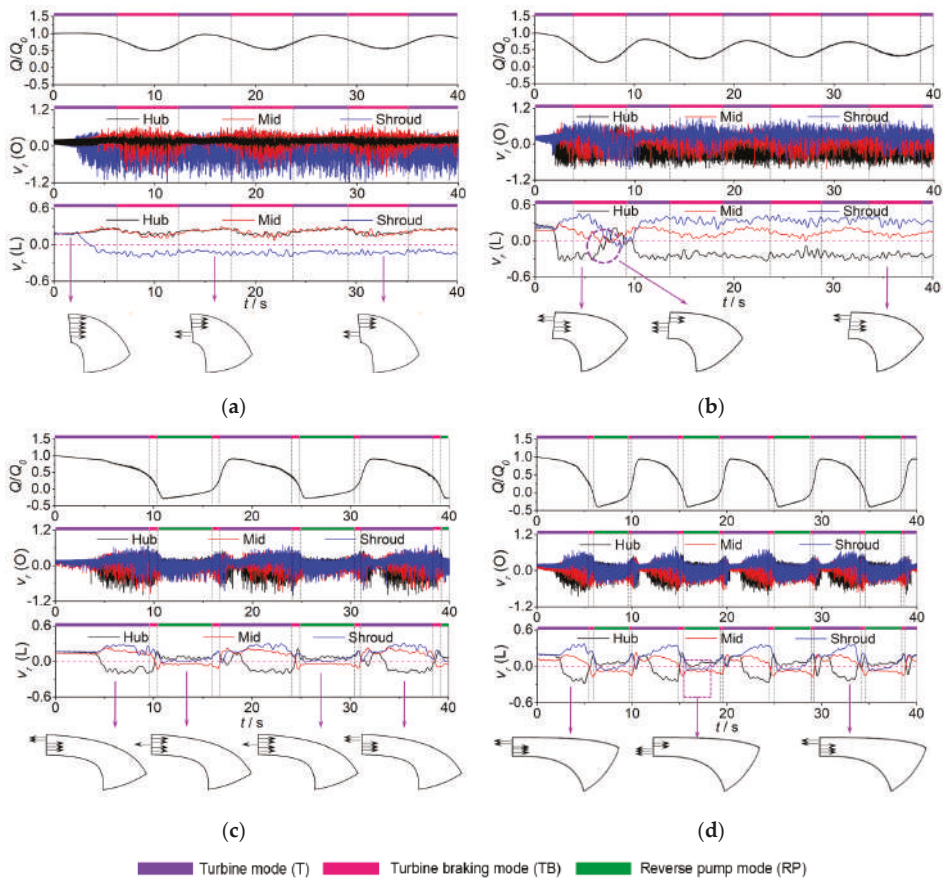


**Figure 3.** Variations of the normalized radial velocity  $v_r$  at the three monitor points: (a) PT-1, (b) PT-2, (c) PT-3, (d) PT-4.

In general, during the beginning period of the runaway process, the rotational speed increases, the inflow attack angle decreases, and the velocity pulsations increase due to the growing impact at the runner inlet. When the backflows occur at the runner inlet (the reverse direction of  $v_r$ ), the velocity pulsations suddenly increase. Also, the velocity pulsations are almost the largest near this critical time. The lower the specific speed, the smaller the differences of velocity pulsations in different monitoring points. Consistent with the features in Figure 2, the velocity pulsations in PT-1 and PT-2 are the largest, and those in PT-4 is the smallest. In addition, though the discharge varies periodically, the variations of radial velocity in PT-1 and PT-2 are not obviously, especially at the location where the backflows occur, which are affected by the absence of flow transitions. But for PT-3 and PT-4, the variation period of radial velocity is corresponding to that of discharge. Overall, with the changes of flow rate, there are significant differences in flow features at the runner inlets.

1. PT-1: The dynamic trajectory of PT-1 only goes through the turbine (T) and turbine braking (TB) modes, and the macro parameters only fluctuate in relatively small amplitudes, therefore, the radial velocity (low-pass filtered data) cannot vary violently. At around  $t = 3.6$  s (in the T mode), the radial velocity direction at the shroud side alters, indicating the appearance of backflows. At the same time, the velocity fluctuations increase significantly, namely the flow instability is intensified. However, the radial velocity directions on the hub side and mid span keep unchanged, and the increased

values (high-frequency data) indicate that the water flow can rush into the blade passages more easily. Although the rotational speed and flow rate fluctuate greatly, the radial velocity direction at the runner inlet remains unchanged after  $t = 3.6$  s (Figure 3a).

2. PT-2: Though the working modes experienced are the same as those of PT-1, the developments of backflows show different characteristics because the backflows start from the hub side ( $t = 2.1$  s) in the turbine mode and have transitions. At the early stage of backflow generations, the radial velocity at the mid span increases briefly and then decreases gradually, while that on the shroud side increases rapidly. At about  $t = 8–10$  s (in the TB mode), there are significant transitions of radial velocity directions, namely the backflows occur suddenly at the mid span and shroud side at the same time, while those at the hub side disappear for a short time. After a short stay, backflows return to the hub side again. Similar to the phenomenon in PT-1, although the speed and discharge still fluctuate afterward, backflows keep staying at one location, and there is no transition (Figure 3b).

3. PT-3 and PT-4: Besides the turbine and turbine modes, the dynamic trajectories of these two pump-turbines also go through the reverse pump mode and the backflow transitions are basically similar. All of them generate from the hub side (in the T mode), then turn to the mid span and shroud side (in the TB mode). However, the only difference is that when the working point enters the reverse pump mode, the backflows in PT-3 mainly alternate between the hub side and mid span, while those in PT-4 also spread to the shroud side (Figure 3c,d).

In order to further explore the flow patterns at the runner inlets, Figures 4–7 show backflows at typical times in a single passage. Generally speaking, when the working points leave from the optimal ones, the water will impact on the blades and form backflows, making some water returning to the vaneless space and some water jumping over and impacting the next blade.

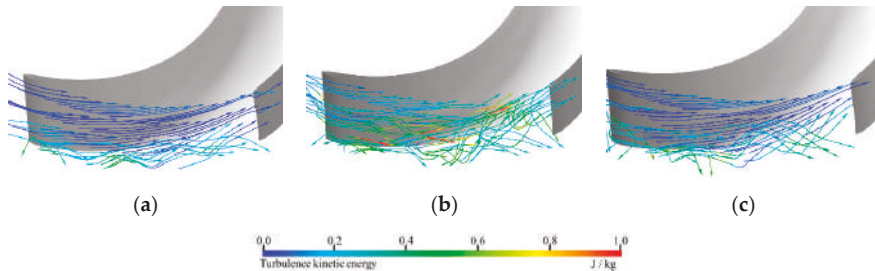


**Figure 4.** Flow patterns at the runner inlet in PT-1: (a)  $t = 3.6$  s (turbine (T)), (b)  $t = 10.0$  s (turbine braking (TB)), and (c)  $t = 15.0$  s (T).

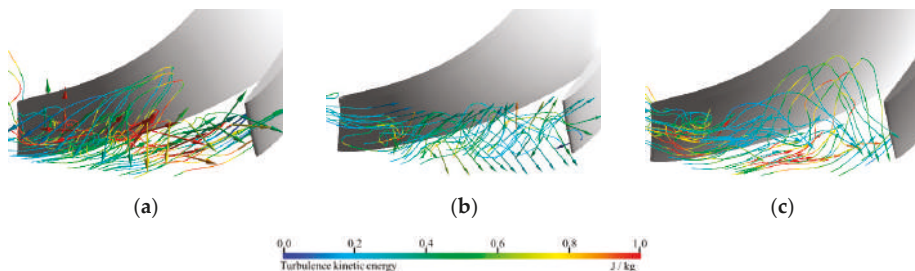


**Figure 5.** Flow patterns at the runner inlet in PT-2: (a)  $t = 5.0$  s (TB), (b)  $t = 8.0$  s (TB), and (c)  $t = 15.0$  s (TB).

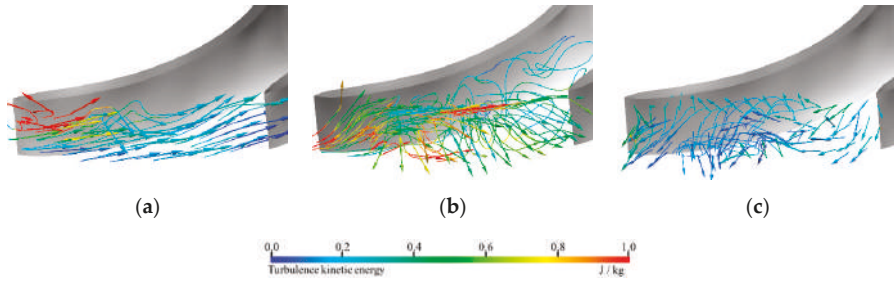


**Figure 6.** Flow patterns at the runner inlet in PT-3: (a)  $t = 8.0$  s (T), (b)  $t = 10.0$  s (TB), (c)  $t = 13.0$  s (reverse pump (RP)).

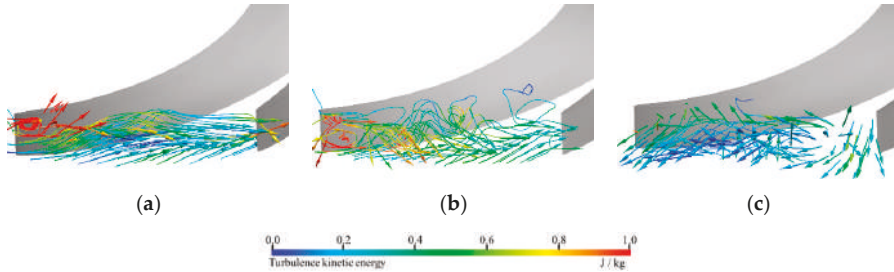


**Figure 7.** Flow patterns at the runner inlet in PT-4: (a)  $t = 4.0$  s (T), (b)  $t = 5.8$  s (TB), (c)  $t = 7.4$  s (RP).

1. PT-1: The backflows generate from the shroud side, while the water flows into the blade passage easily on the hub side. Because the inlet height of PT-1 is relatively large, the backflows are mainly maintained near the shroud over the entire runaway process, and just influence the normal inflow at the mid span (Figure 4a).

2. PT-2: Backflows generate from the hub side and gradually evaluate to other locations. Compared with those in PT-1, the inlet height of PT-2 is smaller, and the backflows are easy to expand to the whole inlet. There is an obvious transition in the flow patterns, and the backflows suddenly occur on the shroud side and at the mid span (Figure 5b,  $t = 8.0$  s), which is consistent with the transition of  $v_r$  in Figure 3b. But with the speed and discharge tending to steady, the backflows keep stay on the hub side.

3. PT-3 and PT-4: The inflow attacks on the blades at the mid span, leading to the upward deviation of the normal inflow on the hub side, then backflows generate and evaluate to other locations. Once entering the reverse pump mode, the backflows at the mid span in PT-3 have less influence to the hub and shroud sides, while those in PT-4 affect the shroud side obviously (Figure 7c).

### 3.3. Pressure Fluctuations in the Time Domain at the Runner Inlets

The dimensionless pressure fluctuations at each monitoring point in the vaneless space are analyzed by comparing with the pressures at the initial time. The normalized pressure was calculated by equation:

$$C_p = \frac{p - p_{\text{initial}}}{0.5\rho u_1^2} \tag{2}$$

where  $p$  is the instantaneous pressure signals,  $p_{\text{initial}}$  is mean initial pressure values at the initial time,  $\rho$  is the water density, and  $u_1$  is the tip velocity of the runner blade leading edge. In addition,  $C_p$  (O) and  $C_p$  (L) in Figure 8 are the original and low-pass filtered data, respectively, and the upper frequency limit of the low-pass filtered data is 2 Hz.

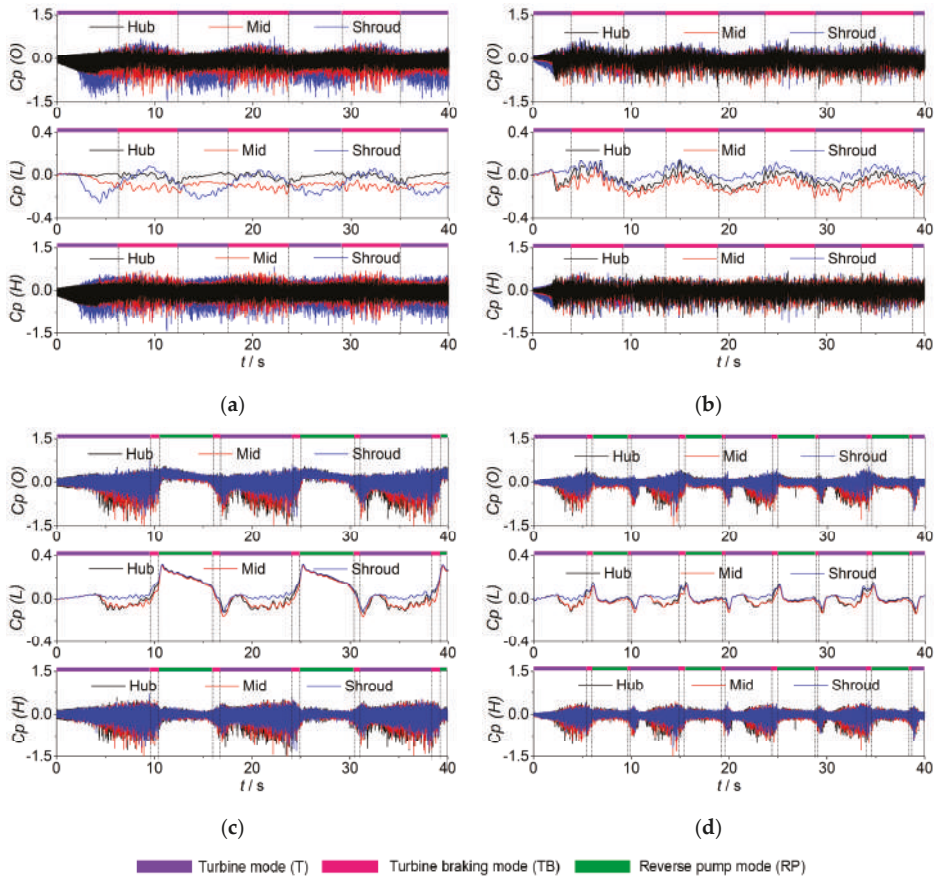


**Figure 8.** Variations of normalized pressure  $C_p$  at the three monitoring points of runner inlet: (a) PT-1, (b) PT-2, (c) PT-3, (d) PT-4.

Previous research has shown that after runaway, backflows will enhance the rotor–stator interactions and greatly increase the amplitudes of pressure pulsations [1]. Figure 8 shows the pressure pulsations in the time domain at the runner inlets of the four pump-turbines. On the whole, under the same total rotational inertia of runner and generator, the amplitudes in PT-1 and PT-3 are relatively large, while those in PT-2 and PT-4 are relatively small. It is found that the longer fluctuation periods of PT-1 and PT-3 mean the longer residence time in the S-shaped region and larger pressure pulsations. In addition, with the variations of rotational speed and discharge, the pressure pulsations present regular changes, with the amplitudes reach the maximum near the runaway point. Due to the different working conditions, there are obvious different characteristics of pressure pulsations.

1. PT-1 and PT-2: The working points only go through the T and TB modes, and the filtered data only slightly vary with the changes of rotational speed and discharge, while the amplitudes of high-frequency signals have no obvious change.

2. PT-3 and PT-4: The trends of pressure pulsations in these two pump-turbines are basically the same, and before the RP mode, they are all similar to those in PT-1 and PT-2 because the low-pass filtered pressure has a shut down when the backflow occurs. However, with the conversion from the TB mode to the RP mode, the low-frequency signals have a significant increase. And when the reverse discharge increases to the maximum value, the low-frequency signals also reach at the maximum.

This is because the rotating energy of the runner and rotor is converted to the water head of the pump-turbine. In addition, the pressure variations in PT-3 and PT-4 in the RP mode are still quite different. In particular, the low-frequency signals decrease slowly in PT-3, while those in PT-4 decrease rapidly. The reason is that the backflows at the runner inlet are quite different during this period. In PT-3, backflows are mainly at the mid span, contributing to poor flow capacity to get water out of the blade passages, forming flow blockage at the inlet and increasing pressure [1]. However, in PT-4, backflows occur at the mid span and on the shroud side at the same time, with strong flow capacity and rapid pressure reduction. For the high-frequency signals, the amplitudes of those in the T mode gradually increase, while those in the TB and RP modes decrease.

Compared with the velocity pulsations in Figure 3, it is found that when the working points of PT-3 and PT-4 enter the RP mode, the velocity pulsation always keeps high amplitude characteristics, while the amplitude of pressure pulsations decreases rapidly, which means the unsteady development of the flow patterns cannot accurately reflect the true values of the pressure pulsations. Figures 4–7 not only show the flow pattern development at the runner inlets, but also show the magnitude of turbulent kinetic energy. It can be seen that the turbulent kinetic energy at the runner inlet is relatively low after entering the RP mode, indicating that pressure pulsations will decrease rapidly when the turbulent kinetic energy becomes small.

### 3.4. Pressure Fluctuations in Time–Frequency Domain at the Runner Inlets

A time–frequency analysis of the transient pressure pulsations at the monitoring points was performed by using the Short Time Fourier Transform (STFT) method [30–32]. From Figures 9–12, at the beginning of the runaway process, the characteristics of pressure pulsations are mainly influenced by the runner. The dominant frequency in the spectrogram is the blade passing frequency (BPF) ( $7f_0$  for PT-1;  $9f_0$  for PT-2, PT-3, and PT-4, where  $f_0$  is the rotating frequency of the runner rotation), and the rest high frequencies are the integer multiples of the BPF.

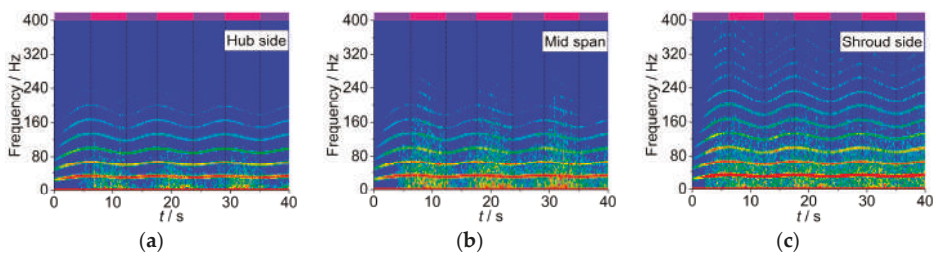


**Figure 9.** Frequency spectrums for pressures at the monitoring points of PT-1: (a) at hub side, (b) at mid span, (c) at shroud side.

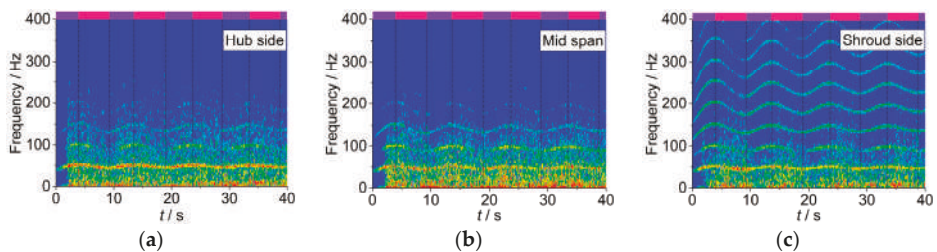


**Figure 10.** Frequency spectrums for pressures at the monitoring points of PT-2: (a) at hub side, (b) at mid span, (c) at shroud side.

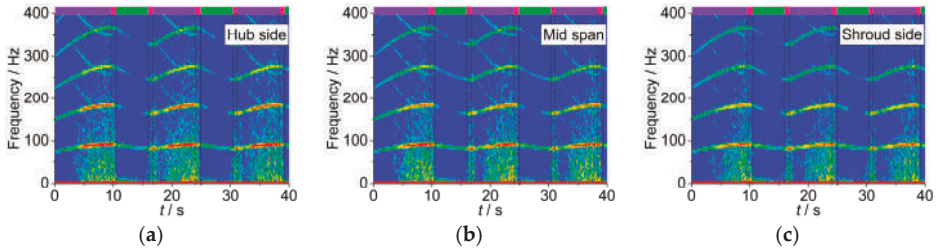


**Figure 11.** Frequency spectrums for pressures at the monitoring points of PT-3: (a) at hub side, (b) at mid span, (c) at shroud side.

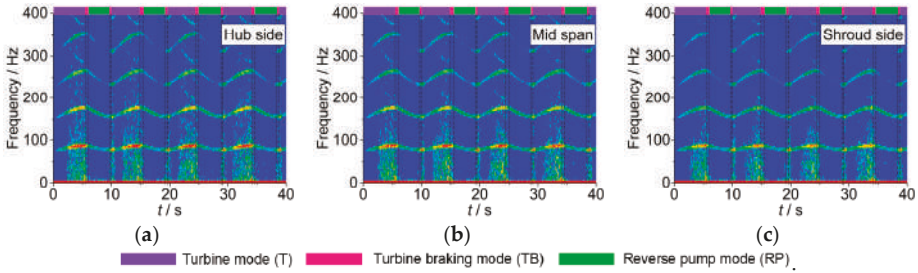


**Figure 12.** Frequency spectrums for pressures at the monitoring points of PT-4: (a) at hub side, (b) at mid span, (c) at shroud side.

In the runaway process, each outstanding frequency varies with the change of rotational speed. As a whole, the amplitude of each frequency increases obviously once the working point enters the S-shaped region, which is due to the enhancement of impact at the runner inlet and rotor-stator interaction. In addition, the high-amplitude low-frequency signals occur obviously, and their occurrence time is consistent with the reduction of inlet radial velocity. Once the backflows generate, the amplitude increases rapidly and reaches at the maximum near the runaway point. Previous studies shown that the high-amplitude low-frequency signals are mainly caused by rotating stalls [1].

In contrast, in PT-1 and PT-2, the durations of the maximum amplitude are mainly after the runaway point, while those in PT-3 and PT-4 are before the runaway point, indicating that the evolutions of unstable flow patterns are affected quite differently by the S-shaped characteristics. Because the working points of PT-3 and PT-4 have gone through the RP mode, the amplitudes suddenly decrease obviously at  $t = 10$  s (PT-3) and  $t = 5$  s (PT-4), and increase at  $t = 16$  s (PT-3) and  $t = 10$  s (PT-4), respectively. All of these phenomena are caused by the backflow transitions, consistent with the changes of pressure fluctuations in the time domain spectrum in Figure 8.

For each runner, the amplitudes of pressure pulsations in different locations at the runner inlet are also different. In PT-1 and PT-2, the differences of pressure pulsation characteristics at the three monitoring points Figure 8 are quite large, while those in PT-3 and PT-4 are smaller. Taking PT-1 as an example, with the runaway beginning, the radial velocity at the inlet decreases obviously, and the low-frequency signals gradually generate at each monitoring point. Once the backflows occur on the shroud side, the amplitudes increase rapidly. Compared with pressure fluctuations at the three locations, the duration of the low-frequency signals is the longest on the shroud side, and they exist in the whole S-shaped region, because the backflows keep staying at this location all of the time. However, the highest amplitudes of low-frequency signals are at the mid span, while the lowest ones are on the hub side, and there are only low-frequency signals at the runaway point. In PT-2, the same phenomenon as in PT-1 is that the location with the highest amplitudes is also at the mid span, though the backflows occur on the hub side. In PT-3 and PT-4, there are no significant differences in the frequency of pulsations in different locations.

From the analysis mentioned above, we know that the high-amplitude low-frequency signals will generate at the location where backflows occur, which is the most obvious in PT-1 because its inlet height is the largest. These phenomena also have the same laws in PT-3 and PT-4, but the difference is not obvious because their inlet heights are smaller. However, the pressure characteristics in PT-2 is an exception Figure 10, which will be discussed in the later chapter.

### 3.5. Flow Patterns in Blade Passage and Draft Tube

Even if the radial velocity at the runner outlet cannot be exactly monitored like that at the inlet, the outlet backflows can be observed clearly from the flow patterns in the draft-tube and near the blade suction side as seen in Figures 13–16. After the working point enters the S-shaped region, the streamlines in the blade channels are no longer as smooth as before. The main flow will enter the draft-tube along the side wall, or return to the runner from the draft-tube center, due to the changes in rotational speed and discharge [31]. As mentioned before, whether or not the working point enters the RP mode can lead to large differences in flow patterns, which has no exception at the runner outlet. For PT-1 and PT-2 (Figures 13 and 14), although the total flow rate is mainly in the turbine direction, the main stream water flow attacks the blade suction side from the draft-tube center, because of the increase of the pumping effect. Some water jumps into the nearby runner channel, and some go back to the draft-tube. Also, this phenomenon will be very obvious when the minimum discharge condition is approached. But in PT-3 and PT-4 Figures 15 and 16, the working points also enter the RP mode, and the flowing directions reverse to the pump direction. At this time, a part of water flow enters the upstream along the suction surface, and a part escapes to the next blade channel, and a little water returns to the draft-tube.

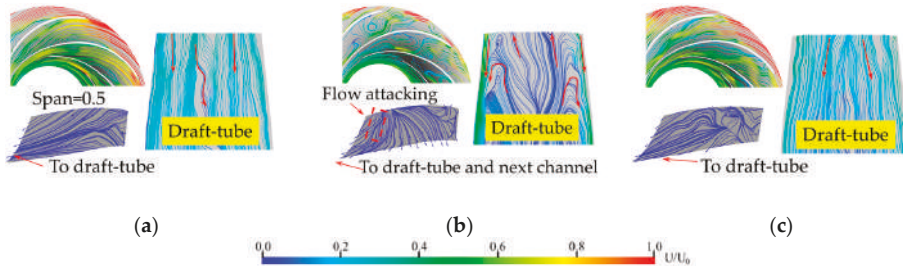


Figure 13. Flow patterns in PT-1. (a)  $t = 3.6$  s, (b)  $t = 10.0$  s, and (c)  $t = 15.0$  s.

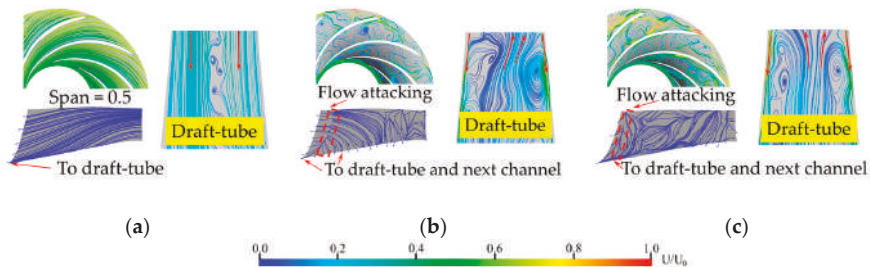


Figure 14. Flow patterns in PT-2. (a)  $t = 0.1$  s, (b)  $t = 7.0$  s, and (c)  $t = 15.0$  s.

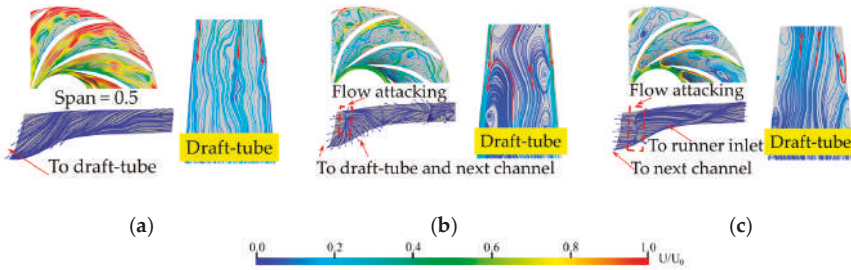


Figure 15. Flow patterns in PT-3. (a)  $t = 5.0$  s, (b)  $t = 10.0$  s, and (c)  $t = 13.0$  s.

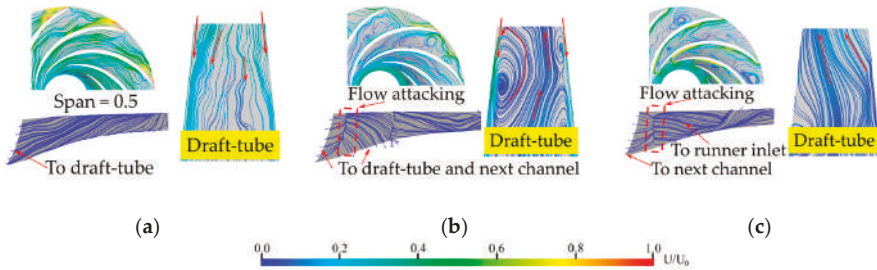


Figure 16. Flow patterns in PT-4. (a)  $t = 4.0$  s, (b)  $t = 5.8$  s, and (c)  $t = 7.4$  s.

#### 4. Discussions of Influences of Runner Shapes

It can be seen from the above analysis that the starting and staying locations of backflows at the runner inlets are different during the runaway processes in the pump-turbines with different specific speeds. Xia [33] pointed out that the backflow structures are mainly affected by the shape of the blade inlet and centrifugal force, which can change the pressure gradient. Similarly, the initial position of backflows is related to this factor. Figure 17 shows the different blade lean angles of the four pump-turbines, which mean the inclination angles of blade leading edges at the runner inlets. The blade lean angle of PT-1 is negative, and its backflows generate from the shroud side. The blade lean angle PT-2 is positive, and its backflows generate from the hub side. Interestingly, the inlets of PT-3 and PT-4 have no blade lean, but the backflows also generate from the hub side.

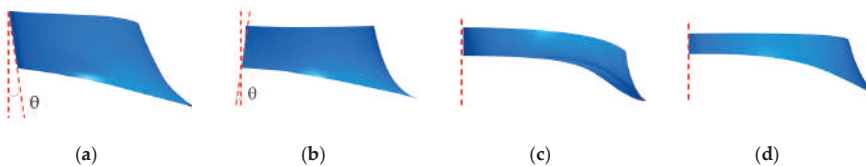
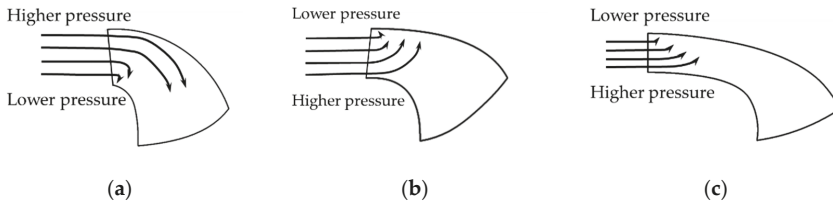


Figure 17. Lean angles of the blade leading edges of the four pump-turbines: (a) PT-1, negative lean angle, (b) PT-2, positive lean angle, (c) PT-3, no blade lean, (d) PT-4, No blade lean.

As shown in Figure 8, it can be seen from the filtered-data that in the early stage of runaway, the pressures at the monitoring points are approximately the same and there is no backflow. With the increase in rotating speed, the centrifugal force increases but the discharge decreases, then the pressure gradient between the hub and shroud sides becomes larger, resulting in water flows from the higher-pressure side to the lower one. Here, the blade lean angle affects the distribution of pressure gradient and leads to the different initial position of backflows. The negative lean angle of PT-1 forces the pressure to increase on the hub side, which makes the water turn from the hub side to middle and shroud ones, leading to backflows on the shroud side Figure 18a. On the contrary, the backflows in

PT-2 generate from the hub side due to the existence of a positive lean angle Figure 18b. Although there is no lean angle in PT-3 and PT-4, the pressure gradient distribution in them is consistent with that in PT-2, therefore the backflows all generate from the hub side Figure 18c.



**Figure 18.** Diagram explaining the reason of backflows at runner inlet in four pump-turbines: (a) PT-1, (b) PT-2, (c) PT-3 and PT-4.

Secondly, the different heights of runner inlets affect the development of backflows. The smaller the height of runner inlet, the easier the backflows change location. The inlet height of PT-1 is the largest, therefore the backflows can only exist on the shroud side all the time, and the influence range of backflows is relatively small. Therefore, due to the lowest height of PT-4, in the RP mode, the relative backflow region can be larger than that in PT-3 Figure 3. Because of these differences in backflow transitions, pressure pulsation evolutions get large differences. With the decrease of the inlet height, the differences of the pressure fluctuations between three locations decrease. Hence, the difference of the pressure fluctuations at each location in PT-1 is the largest, while that in PT-4 is the smallest. In the above four runners, except for PT-2, the location where the backflows occur, the pressure amplitudes are the largest. As a special case, the blade inlet design of PT-2 is the main reason that the blade leading edge diameters at the three locations are quite different Figure 19b. Due to the difference of blade leading edge diameters at the three locations, the pressure characteristics in PT-2 is an exception. Therefore, besides the backflows, the size of the vaneless space and distance to the blade should be considered.

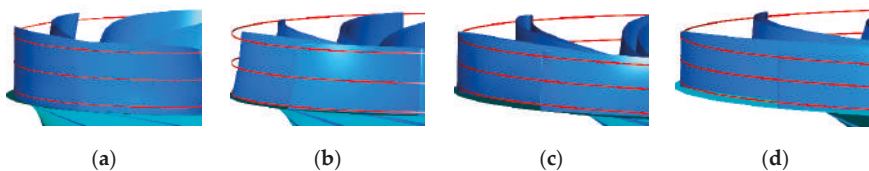


**Figure 19.** Differences of blade leading edge diameters of the four pump-turbines: (a) PT-1, (b) PT-2, (c) PT-3, (d) PT-4.

In order to further verify the analysis mentioned above, the runaway process of a conventional turbine was also simulated, and the detailed information including the lean angle of blade leading edge and inlet diameter was shown in Figure 20. Though the starting working condition of runaway is not the rated one, it is a large guide-vane opening case, which is near the rated working point and can reflect the main characteristics of backflows and pressure pulsations.

The results show that the macro parameters nearly maintain constant values after  $t = 4$  s due to the absence of the S-shaped characteristics, and the period during this time is defined as the no-load mode (Figure 21). The radial velocity and flow patterns are selected (Figures 22 and 23), and it can be seen that the backflows only generate on the hub side, which is similar to those in PT-2 because these two turbines have the same blade lean angle (Figures 17b and 20a) and the same pressure gradient (Figure 18b). Also, the backflows keep staying on the hub side because the runner inlet height is relatively large, which is similar to those in PT-1.

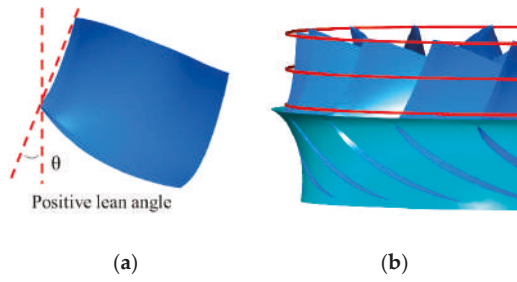


Figure 20. Lean angle of blade leading edge and inlet diameter of CT. (a) Inlet lean angle and (b) inlet diameter.

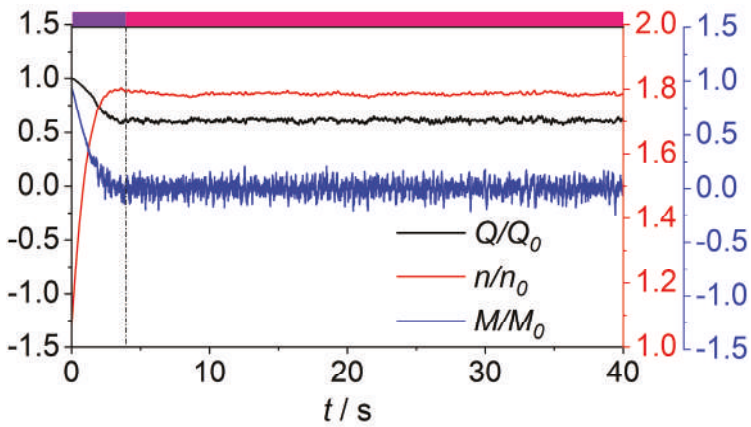


Figure 21. Histories of the macro parameters of CT during runaway processes.

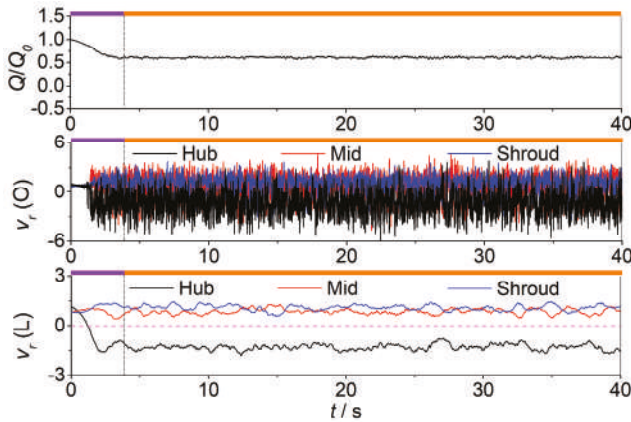


Figure 22. The variations of normalized radial velocity  $v_r$  of three monitor points in CT.

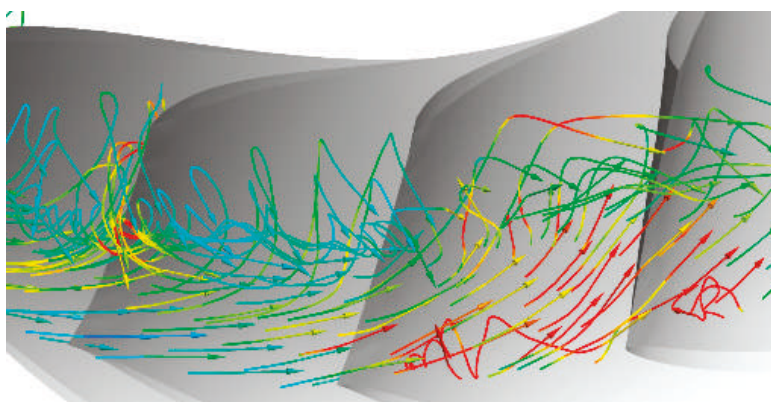


Figure 23. Flow patterns at the runner inlet of CT.

## 5. Conclusions

The transient processes of the four pump-turbines with different specific speeds from turbine mode were simulated, and the macro parameter variations, flow pattern evolutions, as well as pressure fluctuations were analyzed. The working conditions, the transitions of backflows at the runner inlet and outlet, and the pressure pulsations at different locations were compared, and the following conclusions were drawn.

1. The lower specific speed of the pump-turbine, the easier the chance for pump-turbines to enter into the reverse pump mode, generating undamped runaway oscillations. During these runaway processes, backflows and violent pressure pulsations occur in all turbines, and similarities and differences are obvious.

2. The position where the backflows generate at the runner inlet is related to the blade lean angle, which can affect the distribution of pressure gradient. As a result, the water turns from the higher-pressure side to the lower one, then the backflows generate at the lower pressure side. In addition, because lower specific speed turbine has smaller inlet height, the backflows occupy relatively larger range at the runner inlet and are easier to have transitions.

3. The pressure pulsations at different locations are influenced by the relative runner inlet height, distance to runner blades and flow pattern transitions. The smaller the runner inlet height, the smaller the differences in the pressure signals at three locations. The smaller the distance to the runner blades, the larger the pressure pulsations. Furthermore, flow pattern transitions and the turbulent kinetic energy distribution are important and should be considered.

4. S-characteristics in different pump-turbines are quite different, therefore, besides the four pump-turbines in this paper, more pump-turbines should be chosen to investigate the evolutions of pressure pulsation and flow patterns during the runaway process. Also, more factors including water conveyance systems, inertia of rotating parts, and guide vane openings should be considered to study the flow patterns and pressure pulsations in practical power stations. In addition, control methods should be investigated in the design stage by 3D simulations of transient processes.

**Author Contributions:** Data curation, Z.L. and Z.Y.; formal analysis, Z.Y. and Z.L.; investigation, Z.Y. and L.X.; validation, X.Z.; writing—original draft, Z.Y. and Y.C.; writing—review & editing, K.L. and X.Z. All authors have read and agreed to the published version of the manuscript.

**Funding:** This work was supported by the National Natural Science Foundation of China (NSFC) (Grant Nos. 51839008 and 51579187), the Natural Science Foundation of Hubei Province (Grant No. 2018CFA010), the National Natural Science Foundation of China (Grant No. 51909226), and the Natural Science Foundation of Fujian Province, China (Grant No. 2018J01525).

**Acknowledgments:** The numerical simulations were conducted on the supercomputing system in the Supercomputing Center of Wuhan University.

**Conflicts of Interest:** The authors declare no conflict of interest.

## Nomenclature

$b_0$	height of runner inlet (m)
$C_p$	normalized pressure at the runner inlets (-)
$C_p (O)$	original data of normalized pressure at the runner inlets (-)
$C_p (L)$	low-pass filtered data of normalized pressure at the runner inlets (-)
$C_p (H)$	$C_p (O) - C_p (L)$ , high frequency data of normalized pressure at the runner inlets (-)
$D$	diameter of the runner inlet (m)
$E_1$	total energy values at the spiral-casing inlet (m)
$E_2$	total energy values at the runner outlet (m)
$GD^2$	Inertia of rotating parts ( $10^7 \text{ kg} \cdot \text{m}^2$ )
$H_r$	rated head (m)
$H$	head during the runaway process (m)
$M$	moment during the runaway process (N·m)
$M_0$	moment at the initial time (N·m)
$M_{11}$	unit torque (N·m)
$n$	rotational speed during the runaway process (rpm)
$n_0$	rotational speed at the initial time (rpm)
$n_1$	rotational speed at the initial time (rad/s)
$n_{11}$	unit speed (rpm)
$n_s$	specific speed (m · kW)
$n_r$	rated rotational speed (rpm)
$N_r$	rated output (MW)
$p$	instantaneous pressure (Pa)
$p_{\text{initial}}$	mean initial pressure values at the initial time (Pa)
$Q$	discharge during the runaway process ( $\text{m}^3/\text{s}$ )
$Q_0$	discharge at the initial time ( $\text{m}^3/\text{s}$ )
$Q_{11}$	unit discharge ( $\text{m}^3/\text{s}$ )
$t$	times (s)
$u_1$	tip velocity of runner blade leading edge (m/s)
$U_r$	the instantaneous radial velocity (m/s)
$v_r$	normalized radial velocity at the runner inlets (-)
$v_r (O)$	original data of normalized radial velocity at the runner inlets (-)
$v_r (L)$	low-pass filtered data of normalized radial velocity at the runner inlets (-)
$\rho$	water density ( $\text{kg}/\text{m}^3$ )

## References

- Xia, L.; Cheng, Y.; Yang, Z.; You, J.; Yang, J.; Qian, Z. Evolutions of Pressure Fluctuations and Runner Loads during Runaway Processes of a Pump-Turbine. *J. Fluids Eng. Trans. ASME* **2017**, *139*, 091101. [[CrossRef](#)]
- Fu, X.; Li, D.; Wang, H.; Zhang, G.; Li, Z.; Wei, X. Numerical simulation of the transient flow in a pump-turbine during load rejection process with special emphasis on hydraulic acoustic effect. *Renew. Energy* **2020**, *155*, 1127–1138. [[CrossRef](#)]
- Li, D.; Wang, H.; Xiang, G.; Gong, R.; Wei, X.; Liu, Z. Unsteady simulation and analysis for hump characteristics of a pump turbine model. *Renew. Energy* **2015**, *77*, 32–42.
- Barbour, E.; Wilson, I.; Radcliffe, J.; Ding, Y.; Li, Y. A review of pumped hydro energy storage development in significant international electricity markets. *Renew. Sustain. Energy Rev.* **2016**, *61*, 421–432. [[CrossRef](#)]
- Durga Hari Kiran, B.; Sailaja Kumari, M. Demand response and pumped hydro storage scheduling for balancing wind power uncertainties: A probabilistic unit commitment approach. *Int. J. Electr. Power Energy Syst.* **2016**, *81*, 114–122. [[CrossRef](#)]

6. Cai, J.; Zhou, X.; Deng, L. The research of the abnormal water hammer phenomenon based on the unit 3 over speed test of Jiangsu. *Water Power* **2009**, *35*, 87–90. (In Chinese)
7. Li, Q.; Li, J.; Hu, Q.; Yu, J. Site test on S-shape characteristics of large-sized mixed flow reversible turbine-generator unit. *Northwest Hydropower* **2012**, *51*, 81–85. (In Chinese)
8. Ma, M. Analysis and solution of grid connection failure under low head condition. *Mech. Electr. Tech. Hydropower Stn.* **2002**, *2*, 37–39. (In Chinese)
9. Le, Z.; Kong, L. Cause analysis on rotating part lifting of unit 2 in Tianhuangping pumped storage plant. *Mech. Electr. Tech. Hydropower Stn.* **2005**, *28*, 11–13. (In Chinese)
10. Yang, Z.; Cheng, Y.; Xia, L.; Meng, W.; Gao, L.; Dai, X. Evolutions of guide vane moment of a pump-turbine during runaway transient process after pump trip. *IOP Conf. Ser. Earth Environ. Sci.* **2019**, *240*, 072033. [[CrossRef](#)]
11. Li, D.; Fu, X.; Zuo, Z.; Wang, H.; Li, Z.; Liu, S.; Wei, X. Investigation methods for analysis of transient phenomena concerning design and operation of hydraulic-machine systems—A review. *Renew. Sustain. Energy Rev.* **2019**, *101*, 26–46. [[CrossRef](#)]
12. Zhang, Y.; Wu, Y. A review of rotating stall in reversible pump turbine. *Proc. Inst. Mech. Eng. Part C J. Mech. Eng. Sci.* **2017**, *231*, 1181–1204. [[CrossRef](#)]
13. Zuo, Z.; Liu, S.; Sun, Y.; Wu, Y. Pressure fluctuations in the vaneless space of High-head pump-turbines—A review. *Renew. Sustain. Energy Rev.* **2015**, *41*, 965–974. [[CrossRef](#)]
14. Gentner, C.; Sallaberger, M.; Widmer, C.; Braun, O.; Staubli, T. Numerical and experimental analysis of instability phenomena in pump turbines. *IOP Conf. Ser. Earth Environ. Sci.* **2012**, *15*, 032042. [[CrossRef](#)]
15. Wang, L.; Yin, J.; Jiao, L.; Wu, D.; Qin, D. Numerical investigation on the “S” characteristics of a reduced pump turbine model. *Sci. China Technol. Sci.* **2011**, *54*, 1259–1266. [[CrossRef](#)]
16. Widmer, C.; Staubli, T.; Ledergerber, N. Unstable characteristics and rotating stall in turbine brake operation of pump-turbines. *J. Fluids Eng. Trans. ASME* **2011**, *133*, 1–9. [[CrossRef](#)]
17. Hasmatuchi, V.; Farhat, M.; Roth, S.; Botero, F.; Avellan, F. Experimental evidence of rotating stall in a pump-turbine at off-design conditions in generating mode. *J. Fluids Eng. Trans. ASME* **2011**, *133*, 1–8. [[CrossRef](#)]
18. Jacquet, C.; Fortes-Patella, R.; Balarac, L.; Houdeline, J.B. CFD investigation of complex phenomena in S-shape region of reversible pump-turbine. *IOP Conf. Ser. Earth Environ. Sci.* **2016**, *49*, 042010. [[CrossRef](#)]
19. Trivedi, C.; Cervantes, M.; Gandhi, B. Investigation of a high head Francis turbine at runaway operating conditions. *Energies* **2016**, *9*, 149. [[CrossRef](#)]
20. Trivedi, C.; Gandhi, B.; Cervantes, M.; Dahlhaug, O. Experimental investigations of a model Francis turbine during shutdown at synchronous speed. *Renew. Energy* **2015**, *83*, 828–836. [[CrossRef](#)]
21. Trivedi, C.; Cervantes, M.; Gandhi, B.; Dahlhaug, O. Transient pressure measurements on a high head model Francis turbine during emergency shutdown, total load rejection, and runaway. *J. Fluids Eng. Trans. ASME* **2014**, *136*, 121107. [[CrossRef](#)]
22. Trivedi, C.; Cervantes, M.; Dahlhaug, O.; Gandhi, B. Experimental investigation of a high head Francis turbine during spin-no-load operation. *J. Fluids Eng. Trans. ASME* **2015**, *137*, 061106. [[CrossRef](#)]
23. Yin, J.; Wang, D.; Walters, D.; Wei, X. Investigation of the unstable flow phenomenon in a pump turbine. *Sci. China Phys. Mech. Astron.* **2014**, *57*, 1119–1127. [[CrossRef](#)]
24. Zhang, X.; Cheng, Y.; Xia, L.; Yang, J.; Qian, Z. Looping dynamic characteristics of a pump-turbine in the s-shaped region during runaway. *J. Fluids Eng. Trans. ASME* **2016**, *138*, 1–10. [[CrossRef](#)]
25. Wei, B.; Ji, C. Study on rotor operation stability of high-speed large-capacity generator-motor: The Accident of Rotor Pole in Huizhou Pumped-Storage Power Station. *Water Power* **2010**, *36*, 57–60. (In Chinese)
26. Zhou, Q.; Xia, L.; Zhang, C. Internal mechanism and improvement criteria for the runaway oscillation stability of a pump-turbine. *Appl. Sci.* **2018**, *8*, 2193. [[CrossRef](#)]
27. Zhang, X. Three-Dimensional Transient Flow in Pumped-Storage Plant: Simulation and Analysis by Coupling One-Dimensional Water Conveyance System with Three-Dimensional Pump-Turbine. Ph.D. Thesis, Wuhan University, Wuhan, China, 2015.
28. Zhang, X.; Cheng, Y.; Yang, Z.; Chen, Q.; Liu, D. Influence of rotational inertia on the runner radial forces of a model pump-turbine running away through the S-shaped characteristic region. *IET Renew. Power Gener.* **2020**, *14*, 1883–1893. [[CrossRef](#)]

29. Xia, L.; Cheng, Y.; Yang, Z.; Yuan, Y.; Zhu, Z. Numerical investigations into the transient behaviour of a model pump-turbine during load rejection process. *IOP Conf. Ser. Earth Environ. Sci.* **2019**, *240*, 072040. [[CrossRef](#)]
30. Liu, Q.; Su, W.; Li, X.; Zhang, Y. Dynamic characteristics of load rejection process in a reversible pump-turbine. *Renew. Energy* **2020**, *146*, 1922–1931. [[CrossRef](#)]
31. Yang, Z.; Cheng, Y.; Xia, L.; Meng, W.; Liu, K.; Zhang, X. Evolutions of flow patterns and pressure fluctuations in a prototype pump-turbine during the runaway transient process after pump-trip. *Renew. Energy* **2020**, *152*, 1149–1159. [[CrossRef](#)]
32. Fu, X.; Li, D.; Wang, H.; Zhang, G.; Li, Z.; Wei, X. Dynamic instability of a pump-turbine in load rejection transient process. *Sci. China Technol. Sci.* **2018**, *61*, 1765–1775. [[CrossRef](#)]
33. Xia, L. Mechanism of the S-Shaped Characteristics and the Flow-Induced Dynamic Instability of Pump-Turbines. Ph.D. Thesis, Wuhan University, Wuhan, China, 2017.



© 2020 by the authors. Licensee MDPI, Basel, Switzerland. This article is an open access article distributed under the terms and conditions of the Creative Commons Attribution (CC BY) license (<http://creativecommons.org/licenses/by/4.0/>).